HIGH-PERFORMANCE ROOM-TEMPERATURE AMMONIA GAS SENSOR BASED ON MOLYBDENUM TRIOXIDE NANOSTRUCTURE

CHUA WEN HONG

INSTITUTE FOR ADVANCED STUDIES
UNIVERSITI MALAYA
KUALA LUMPUR

2021

HIGH-PERFORMANCE ROOM-TEMPERATURE AMMONIA GAS SENSOR BASED ON MOLYBDENUM TRIOXIDE NANOSTRUCTURE

CHUA WEN HONG

DISSERTATION SUBMITTED IN FULFILMENT OF THE REQUIREMENTS FOR THE DEGREE OF MASTER OF PHILOSOPHY

INSTITUTE FOR ADVANCED STUDIES
UNIVERSITI MALAYA
KUALA LUMPUR

2021

UNIVERSITI MALAYA
ORIGINAL LITERARY WORK DECLARATION

Name of Candidate: **Chua Wen Hong**

Registration/Matric No: **17217736/1**

Name of Degree: **Master of Philosophy**

Title of project Paper/Research Report/Dissertation/Thesis:

High-Performance Room-Temperature Ammonia Gas Sensor based on Molybdenum Trioxide Nanostructure

Field of study: **Techniques of Material Characterization (Materials Engineering)**

I do solemnly and sincerely declare that:

(1) I am the sole author/ writer of this work;
(2) This work is original;
(3) Any use of any work in which copyright exists was done by way of fair dealing and for permitted purposes and any excerpt or extract from, or reference or to reproduction of any copyright work has been disclosed expressly and sufficiently and the title of the Work and its authorship have been acknowledged in the Work;
(4) I do not have any actual knowledge nor do I ought reasonably to know that the making if the work constitutes an infringement of any copyright work;
(5) I hereby assign all and every rights in the copyright to this Work to the University of Malaya ("UM"), who henceforth shall be owner of the copyright in this Work and that any reproduction and use in any form or by any means whatsoever is prohibited without the written consent of UM having been the first hand and obtained;
(6) I am fully aware that if in the course of making this Work I have infringed any copyright whether intentionally or otherwise, I may be subject to legal action or any other action as may be determined by UM.

Candidate's Signature Date:

Subscribed and solemnly declared before,

Witness's signature Date:

Name:
Designation:

HIGH-PERFORMANCE ROOM-TEMPERATURE AMMONIA GAS SENSOR BASED ON MOLYBDENUM TRIOXIDE NANOSTRUCTURE

ABSTRACT

In this research, *h*-MoO_3 nanostructure were grown on tapered region of optical fiber glass via simple chemical bath deposition (CBD) to form a unique sensing element to detect ammonia (NH_3) gas in room temperature. As NH_3 gas sensor have been highly demanded due to its commonly utilization of NH_3 gas in various industrial sectors and a highly toxic and corrosive agent that can cause threat human health and environment. Experiment parameter such as type of precursor used, precursor concentration, deposition time and annealing treatment was performed to fine-tuned the growth of *h*-MoO_3 nanostructure and optimised the NH_3 gas sensing performance. The structural, thermal and optical properties of the sample were studied by using field emission scanning electron microscope (FESEM), energy dispersive X-ray (EDS), selected area electron diffraction (SAED), X-ray photoelectron spectroscopy (XPS), X-ray diffraction (XRD), thermogravimetric analysis (TGA), Fourier-transform infrared spectroscopy (FTIR) and UV-Vis spectroscopy. The morphology of the deposited *h*-MoO_3 is highly affected by the types of precursors used. As different precursor concentration and deposition time also affect the overall sensing performance. Overall, the annealing treatment improves the sensitivity, respond time and recovery time of the sensor towards NH_3 gas. However, overheating the sample cause disruption towards gas adsorption due to its metastable characteristic. Among them, the sodium-based *h*-MoO_3 nanorod sample annealed at 150^{o}C shows a stable room-temperature respond of 0.05, 0.18, 0.22, 0.28 and 0.35 au, a fast respond time of 210 s towards 500 ppm of NH_3 and good stability and repeatability. The optical NH_3 gas sensing behaviour have a significant relationship with the interaction between the *h*-MoO_3 nanostructure and the evanescent wave. The chemisorbed oxygen species and physisorbed NH_3 alter the refractive index and its absorption coefficient on the MoO_3 nanostructure which provide manipulation of optical signal as sensing mechanism. This work proved that a chemical bath deposition grown *h*-MoO_3 nanostructure exhibits a promising optical sensing characteristic which shed a light for new emerging gas sensing technology.

Keywords: Chemical bath deposition, *h*-MoO_3, free carriers' absorption, Optical gas sensor.

PENDERIA GAS AMMONIA SUHU BILIK YANG BERPRESTASI TINGGI DENGAN MENGGUNAKAN MOLIBDENUM TRIOKSIDA YANG BERSTRUKTUR NANO

ABSTRAK

Dalam penyelidikan ini, *h*-MoO_3 yang berstruktur nano ditumbuh di kawasan tirus kaca gentian optik melalui kubang kimia (CBD) untuk membentuk elemen penginderaan gas ammonia (NH_3) yang unik yang berfungsi dalam suhu bilik. Penderia gas NH_3 amat diperlukan kerana penggunaan gas NH_3 yang tinggi di berbagai sektor industri dan ia juga sangat beracun dan boleh menjadi ancaman terhadap kesihatan manusia dan persekitaran. Parameter eksperiment seperti jenis prapenanda, kepekatan prapenanda, masa pemendapan dan process penyepuhlindapan telah dijalankan supaya dapat mengoptimumkan penumbuhan *h*-MoO_3 dan tindak balas penderia gas . Sifat struktul, terma dan optik *h*-MoO3 telah dicirikan dengan teknik seperti FESEM, EDS, SAED, XPS, XRD, TGA, FTIR dan UV-Vis. Morfologi *h*-MoO_3 yang ditubuh banyak dipengaruhi oleh jenis prekrusor yang digunakan. Kepekatan prapenanda dan masa pemendapan juga akan mempengaruhi respons penderian gas. Secara keseluruhan, rawatan penyepuhlindapan meningkatkan kepekaan, masa tindak balas dan masa pemulihan sensor terhadap NH_3. Walau bagaimanapun, suhu yang tinggi akan menyebabkan gangguan terhadap penjerapan gas disebabkan ciri metastabilnya. Antaranya, sampel *nanorod h*-MoO_3 yang berdarsar natrium yang dianil pada suhu 150^oC menunjukkan tindak balas suhu bilik yang stabil 0.05, 0.18, 0.22, 0.28 dan 0.35 au, masa tindak balas yang cepat 210 s dalam 500 ppm NH_3 dan kestabilan dan kebolehulangan yang baik. Prestasi penginderaan gas NH_3 optik mempunyai hubungan yang rapat dengan interaksi antara nanostruktur *h*-MoO_3 dengan gelombang evanesen. Spesies oksigen dan NH_3 yang diserap secara kimia dan fizikal turut mengubah indeks biasan dan pekali penyerapannya pada nanostruktur *h*-MoO_3 yang memberikan pertukaran isyarat optik sebagai mekanisme penginderaan. Penyelidikan ini mengesahkan bahawa nanostruktur *h*-MoO_3 yang dihasikan melalui kubang kimia menunjukkan ciri penginderaan optik yang menjanjikan dan memberi harapan kepada teknologi penderiaan gas yang baharu.

Kata kunci: Pemendapan mandi kimia, *h*-MoO_3, penyerapan pembawa bebas, penderia optik gas.

ACKNOWLEDGEMENTS

First and foremost, I would like to convey my sincere appreciation to my supervisor, Associate Prof. Dr. Ong Boon Hoong, Associate Prof. Dr. Tan Chou Yong and Dr. Mohd Hanif Yaacob, for their valuable guidance, constant motivation and enormous support mentally and physically throughout this journey. Being their student under their supervision is truly life changing and profound for me toward the journey in to research.

I would also like to extend my gratitude to my lab mate and best friends for their constant support and cooperation, Mohd Rashid and also Muhammad Nur Iman. They've taught me more than just an experiment in the lab but the whole experience in research and finding new things. I really enjoy the time spent with them, and I've a lot more to learn from them.

I would also like to thank all the technician member and also admin staff including Muhammad Al Amin (NANOCAT procurement Admin) for always helping for the documentation matter and chemical purchases which is quite a hectic without any guidance. Without them this project would not been a success.

Last but not least, I would like to sincere gratitude to my parents for their unconditional love, support and sacrifices. Their support and motivation drive and fuels me through this journey of exploring the unknown in the field of science and always remind me to give back the society when it's time. Without them none of this would be possible and therefore, I would like to dedicate my work to my parents.

TABLE OF CONTENT

LIST OF FIGURES

LIST OF TABLES

LIST OF SYMBOLS AND ABBREVIATIONS

Ar	:	Argon
AHM	:	Ammonium Heptamolybdate $(NH_4)_6$ $Mo_7O_{24}.4H_2O$)
α-MoO_3	:	Alpha molybdenum trioxide
NH_3	:	Ammonia
β-MoO_3	:	Beta molybdenum trioxide
CBD	:	Chemical bath deposition
CLCFC-SPF	:	Cholesteric liquid crystal film coated on side polished fiber
CO	:	Carbon monoxide
CO_2	:	Carbon dioxide
EMI	:	Electromagnetic interferences
EDS	:	Energy Dispersive Spectroscopy
FESEM	:	Field Emission Scanning Electron Microscope
FTIR	:	Fourier-transform infrared spectroscopy
FC	:	Fiber channel
H_2	:	Hydrogen
h-MoO_3	:	Hexagonal molybdenum trioxide
LPG	:	Liquefied petroleum gas
LED	:	Light-emitting diode
MMF	:	Multimode fiber
CH_4	:	Methane
MB Dye	:	Methylene blue
HNO_3	:	Nitric acid
N_2	:	Nitrogen
O_2	:	Oxygen
O_3	:	Ozone

SMO	:	Semiconductor metal oxide
SILAR	:	Successive ion layer adsorption and reaction
SM	:	Sodium molybdate (Na_2MoO_4)
SMF	:	Single mode fiber
SPR	:	Surface plasmon resonance
SO_2	:	Sulfur dioxide
SiO_2	:	Silica
SMA	:	Subminiature assembly
TGA	:	Thermogravimetric Analysis
TIR	:	Total internal reflection
UV-Vis	:	UV-Visible Spectroscopy
VOC	:	Volatile organic compound
Vis-NIR	:	Visible Near-Infrared
XRD	:	X-Ray diffraction

CHAPTER 1: INTRODUCTION

1.1 Background

Ammonia (NH_3), a kind of colourless gas, that has been commonly produced and widely used in various sector in our life. Ammonia is mainly used as a fertilizer, refrigerant gas, water purifier, manufacturing of plastics, explosives, textiles, pesticides, dyes and other chemicals (Kwak et al., 2019; Tanguy, Thompson, & Yan, 2018). It also acts as a fuel for hydrogen gas production which is a promising source of energy in the near future(Abashar, 2018; Miyaoka, Miyaoka, Ichikawa, Ichikawa, & Kojima, 2018). However, this colourless gas which applied by us all the time is not only harmful to the living, but also has negative impact on the surrounding environment. Inhaling 500 ppm of NH_3 causes acute nasal discomfort, whereas inhaling more than 1000 ppm of NH_3 causes pulmonary edema, or the collection of fluid in the lungs, and even mortality if exposed to greater NH_3 concentrations(Girei et al., 2021; Singer, 2007). Hence, developing a high-performance gas sensor for NH_3 detection and monitoring purposes has attracted increasing attention in recent years not only for household safety but also including NH_3 production plants and also food and beverages factories industry.

In the recent decades, semiconductor metal oxide (SMO) has received tremendous amount of attention due to its simplicity, low cost and the ability to be mass produced(Ananya Dey, 2018). The most well-known method to sense gas is using chemiresistor method due to its benefits such as, lower fabrication cost and highly sensitive towards gases. However, chemiresistor sensor require a high operating temperature and vulnerable towards electromagnetic interference which will result in signal compromise. On the other hand, optical sensors have several advantages over chemiresistor sensors, such as a resistance towards electromagnetic interference, compact

size, lightweight, stable in low-signal conditions and resilient in high-temperature environments(Tabassum & Kant, 2020; Y. nan Zhang et al., 2017).

The use of 1D semiconductor metal oxide has also received much attention due to its large surface area for gas absorption. Many of the metal oxide has already well researched such as ZnO, TiO, MnO and even graphene base material (Bigiani et al., 2019; Malallah Rzaij & Mohsen Abass, 2020; Tian, Liu, & Yu, 2018; Tu et al., 2020). Among the metal oxides, MoO_3 has many unique properties, such as a high electrochemical performance, wide bandgap (>2.7 eV)(de Castro et al., 2017) and excellent photo-chromic and electro-chromic performances(K. K. Singh et al., 2017). In general, MoO_3 exists in the following three different polymorphs: the *α*-orthorhombic, *β*-monoclinic and *h*-hexagonal phases. To begin, the *α*-MoO_3 crystal structure is orthorhombic, consisting of stacked, double-layered MoO_6 octahedra building blocks held together by van der Waal's forces. Second, the *β*-MoO_3's structure is similar to the cubic rhenium trioxide (ReO_3), in which the MoO_6 octahedra shares corners and establishes a monoclinic structure. Finally, the hexagonal *h*-MoO_3 is formed by joining the MoO_6 octahedra's zigzag chains in the cis-position along the c-axis (Chithambararaj et al., 2016; Z. Li, Ma, Zhang, Song, & Wang, 2017). Many works have been put on to explore the sensing properties of thermally stable α-MoO_3 but not much attention on the metastable phase *h*-MoO_3. Up till now, there has been no research using MoO_3 in an optical gas sensing system.

For the material deposition part, there are various technique to synthesize MoO_3 ranging from physical method and also chemical method such as sputtering, thermal evaporation, hydrothermal, chemical bath deposition and the sol–gel method (de Castro et al., 2017; Inpan et al., 2018; H. Ren et al., 2018). Among all these deposition techniques, chemical bath deposition is by far consider the only method to fully coat the surrounding of the optical fibre. Hence, chemical bath deposition has been chosen for the choice for deposition.

In this work, a room temperature optical fiber sensor with functionalized *h*-MoO_3 nanorod were fabricated using chemical bath deposition technique. It was confirmed that the material demonstrates a short respond time as well as sensitive & selective respond towards NH_3 gas which shed a light in the gas sensing technology.

1.2 Problem Statement

Despite the benefits of ammonia gas mentioned above, it also come with a cost to our health if exposed to a certain concentration. The pungent smell of ammonia gas can be distinguished by bare nose at around 5 ppm in ambient air. Hence, exposing high concentration of ammonia gas will be easily detectable by any individuals(Dongwook Kwak et al., 2019). Most often it is best to avoid exposure to any high concentration of ammonia gas as exposing to 500 ppm of NH_3 can cause an immediate irritation to the nasal system, while exposing more than 1000 ppm of NH_3 can cause coughing, laryngospasm and pulmonary edema, which is an accumulation of fluid in the lungs. Exposing to higher concentrations of 2500 to 4500 ppm can lead to fatality in approximately 30 minutes(Singer, 2007). As a result, a high-performance and fast-responding gas sensor for NH_3 detection and monitoring is critical not only for household safety but also for NH_3 manufacturing facilities, fertiliser factories, and the food processing sector to minimise any health risks.

Current NH_3 sensors that widely used are chemiresistive based sensor. These chemiresistive based sensors have quite a lot of drawbacks which are high operating temperature and vulnerable towards EMI. Such EMI will interfere the signal obtained during the sensing process which might compromises the system and a heater filament is required to generate extra heat for the sensing(Sabri et al., 2015). In the other hand, optical fiber gas sensor provides benefits of immune under EMI and also able to operate in room temperature environment which is suitable in household set up and also factory

production integration(Y. nan Zhang et al., 2017). Hence, an optical fiber gas sensor can be fabricated by incorporating with a light-reactive metal oxide nanostructure.

The method of material deposition is also a problem to address. The common nanomaterial deposition method ranges from chemical to physical deposition for instance such as spray pyrolysis, sputtering, hydrothermal, sol-gel, dip-coating and drop casting method. Most of these methods are not suitable in this work as it only allows a single side of deposition. Single side deposition will greatly reduce the total surface area induced for gas sensing reaction. In the other hand, chemical bath deposition (CBD) method is able to solve such problem as it required the whole substrate to be immersed into the precursor solution for the growing of nanomaterial(B. A. Ezekoye et al., 2012). This technique provides a much homogeneous and uniform coating on the cylindrical area of optical fiber. Chemical bath deposition also provides an overall cheaper and easier set up. Hence, the optimization of the parameter such as precursor concentration and the deposition time has to be fine-tuned in order to obtain a well-coated metal oxide nanostructure on the optical fiber.

1.3 Research Objectives

This thesis focuses on the development of tapered optical fiber sensor coated with hexagonal molybdenum oxide nanostructures via chemical bath deposition. The objectives of this research are as follows:

1. To synthesize hexagonal molybdenum oxide nanostructures via chemical bath deposition.
2. To fabricate a short respond time, highly sensitive, good repeatability and selective room temperature optical sensor for Ammonia gas.

1.4 Outline of the dissertation

There are five chapters in this dissertation. The following is a summary of each chapter's content:

Chapter 1: This chapter concisely describe the basic information related to the benefits and also the danger of ammonia gas, current gas sensing method for ammonia gas comparing to optical fiber gas sensing, the significance of using molybdenum oxide as gas sensing material. It also focuses on the problem statement, and also introduce the objectives for this research.

Chapter 2: A comprehensive review on the current gas sensing method while comparing to the optical fibre gas sensing, the choice of gas sensing material chosen which is molybdenum oxide, the mechanism behind the metal oxide gas sensing and also the methodology used in this research which is the chemical bath deposition.

Chapter 3: In this chapter, the choice of material used, the methodology performed to modify the optical fiber and to obtained the nanostructure material via chemical bath deposition were clarified. The characterization technique conducted were presented and explained.

Chapter 4: The two kinds of MoO_3 produced from two distinct precursors, Ammonium Heptamolybdate $(NH_4)_6 Mo_7O_{24}\cdot 4H_2O$) and Sodium molybdate ($Na_2MoO_4$), were described in this chapter. For each precursor utilised, it is split into two primary sub parts. Which is section 4.1. *h*-MoO_3 using Ammonium Heptamolybdate as precursor and section 4.2. *h*-MoO_3 using Sodium molybdate (Na_2MoO_4) as precursor. Each section discussed on the characterized data regarding the morphology, chemical component, structural properties, thermal properties and also the optical properties of each sample while adjusting the synthesis parameter of the material. Further, the two different sample was tested under exposure of different NH_3 concentration to identify the dynamic, repeatability and also the selectivity performance of the sensor and the result are discussed in each section. Lastly, the mechanism of the optical NH_3 gas sensing is also discussed in this chapter.

Chapter 5: In the final chapter, we summarize the dissertation with some concluding remarks and some future research suggestions.

CHAPTER 2: LITERATURE REVIEW

2.1 Overview of gas sensor

In the past decades, NH_3 gas detection has been a rise as mentioned earlier in Chapter 1. This is due to the importance of NH_3 used in many major fields of chemical manufacturing and applied in vast area around the globe. However, the toxicity of NH_3 gas can't be ignore and neglected as it also brought many harms to us, human and also other living beings.

Currently, there are many ways to detect this harmful colourless gas. Based on Xiao Liu et al. the gas sensing method has been classified in to two main categories which are: method based on electrical variation with different material. Secondly, different method based on other kind of variation such as optical method, Acoustic method, gas chromatograph and calorimetric methods as shown in Figure 2.1 below(Xiao Liu et al., 2012).

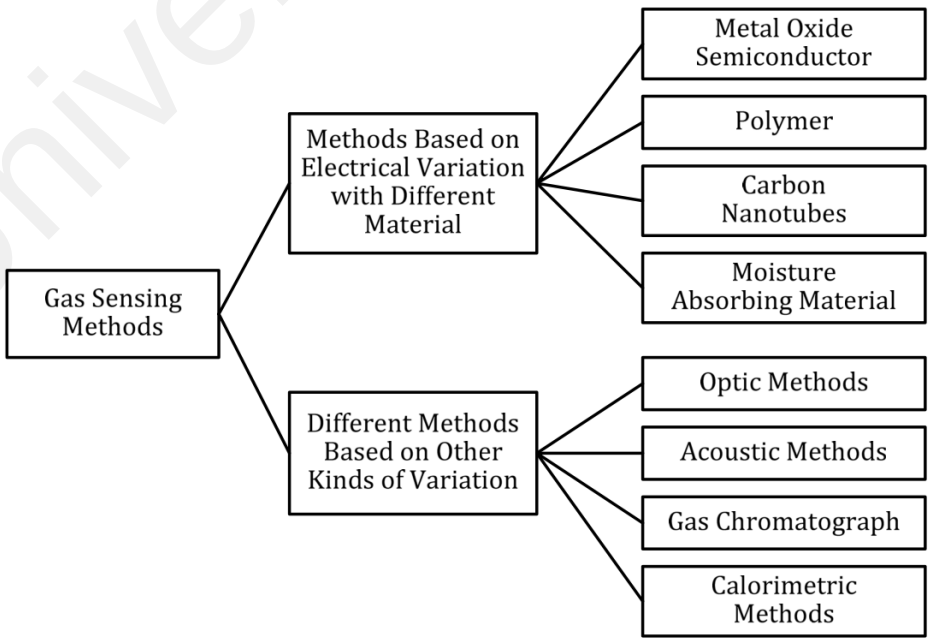

Figure 2.1 Classification of gas sensing method(Xiao Liu et al., 2012)

Every type of sensor plays a very important yet different roles in gas sensing under different situation, they also have different sensing mechanism which allow them to shines in certain application. Firstly, chemiresistive gas sensor is based on the alteration of electrical resistance when the sensing element is exposed under different type of gases environment. This phenomenon is highly depending on the type of materials used as sensing layer and the nature of the target gas. As the change of electrical conductivity during interaction with target gas acts as the sensing mechanism of chemiresistive gas sensor(Majhi, Mirzaei, Kim, Kim, & Kim, 2021). On the other hand, optical fiber-based sensors track changes in optical properties including refractive index (RI), absorbance, reflectance, and transmittance. These changes act as the fundamental sensing mechanism for optical fiber based sensor. All of this is dependent on the physicochemical characteristics of the gases in the studied environment, as well as the sensor's functional material. (Korposh, James, Lee, & Tatam, 2019). Next, acoustic based sensor monitor waves parameters utilizing on ultrasonic methods. These mainly consists of three main categories, the speed of sound, attenuation, and acoustic impedance. Acoustic based sensor can hardly find in the commercial market due to the inclination of attenuation affected by many factors(Jakubik, 2011). Next, gas chromatograph (GC) which usually used in laboratory analytical technique due to its highly sensitive and selective gas sensing ability. Hence, the cost of GC is relatively high, and reducing the GC instrument scale is still impossible with the current technology(Haghighi, Talebpour, & Sanati-Nezhad, 2015). Finally, the calorimetric gas sensor works on the basis of chemical reaction or physisorption, in which heat is absorbed or released and then converted into sensor signals. Calorimetric sensors are commonly employed in severe and industrial environments to detect CH_4 and other flammable gases(Aldhafeeri, Tran, Vrolyk, Pope, & Fowler, 2020). Below is a table tabulated on the advantages and the disadvantages of all the different types of sensors mentioned above.

Table 2.1: Advantages and disadvantages of different types of gas sensing methods(Kwak et al., 2019; Xiao Liu et al., 2012).

Types of gas sensing method	Advantages	Disadvantages	Ref
Chemiresistive gas sensor	a) Relatively Low cost b) Short respond/recovery time c) Long lifetime	a) High operating temperature (250-550°C) b) Risk of ignition and explosion in the sensing environment c) Low sensitivity and selectivity	(Majhi et al., 2021; Srinivasan, Ezhilan, Kulandaisamy, Babu, & Rayappan, 2019)
Optical based sensor	a) High sensitivity, selectivity and stability b) Able to work in wide range of temperature (room temperature to 1500C)	a) Restricted due to miniaturization and relatively high cost	(Korposh et al., 2019; Xiao Liu et al., 2012; Tabassum & Kant, 2020)

	c) Insensitive to environment change d) Long lifetime		
Acoustic based sensor	a) Long lifetime b) Avoiding secondary pollution	a) Low sensitivity b) Sensitive to environment change	(Jakubik, 2011; Kwak et al., 2019; Xiao Liu et al., 2012)
Gas chromatograph gas sensor	a) Excellence separation performance b) High sensitivity and selectivity	a) Higher in cost b) Bulky in size	(Haghighi et al., 2015; Xiao Liu et al., 2012)
Calorimetric gas sensor	a) Low cost b) Moderate sensitivity c) Stable in room temperature	a) Risk of catalyst poisoning and explosion b) Poor in selectivity	(Aldhafeeri et al., 2020; Park, Akamatsu, Itoh, Izu, & Shin, 2014)

In this work, the author is keen to further explore the interesting characteristic of optical based gas sensing using optical fiber platform as its advantages outweigh its limitation of the sensor. In addition, optical based sensor is able to work well in room

temperature which aligned with the author's objective. More details explanation on optical fiber gas sensing will be discussed in Chapter 2.4 to 2.6.

2.2 Material used for gas sensor

Functionalized material is very crucial in all gas sensing devices. This is because the roles of functionalized material are to convert the physical and chemical changes of its property into measurable signal such as electrical signal or optical signal for gas sensing. There are many choices of material to be use as the sensing material with different types of attributes and characteristic ranging from the widely used metal oxide material, carbon nanotube material and polymer-based material.

2.2.1 Polymer based material

Conducting polymer materials are highly used in detecting inorganic gases like CH_4 and H_2O and also VOC compounds. Other than that, it also provides a vast advantage such as, simple in fabrication and modification, sensing stability flexible design and able to tune with other types of material(Xiao Liu et al., 2012). The basic working mechanism of polymer-based material is when the polymer material layers are in contacted with the target gas, gas absorption will occur and lead to a change in the physical properties such as the polymer mass or its dielectric properties. Hence, these changes of properties will be changed in to signal for gas sensing measurement. To be exact, when the interaction of target gas with the polymer layer undergoes a physisorption mechanism which including four different interactions: induced dipole/induced dipole interactions, dipole/induced dipole interactions, dipole/dipole interactions and hydrogen bonds. Overall, the polymer-based material used for gas sensing application are categorized into

two main group which is the conducting polymer and the non-conducting polymer(Wong, Ang, Haseeb, Baharuddin, & Wong, 2020).

First, the conducting polymers, such as polyaniline (Pani), polypyrrole (PPy) and polythiophene (PTh) are well-established material that utilised the alteration of electrical conductivity when exposed to diverse of organic and inorganic gases(H. Bai & Shi, 2007). Such interesting characteristic attracted high effort of exploration towards the potential of conducting polymer-based material in gas sensing application(Albaris & Karuppasamy, 2020; Gaikwad, Patil, Patil, & Naik, 2017; Mane, Navale, & Patil, 2015). Non-conducting polymer, on the other hand, is widely used as a coating on many types of sensor devices. Polymers with various characteristics or physisorption processes can be coated onto transducers to serve as gas sensors. Quartz Crystal Microbalance (QCM), Surface Acoustic Wave (SAW), and Surface Transverse Wave (STW) are some examples of polymer layers sensitive to resonance frequency, dielectric constant, and enthalpy during analytes gas absorption/desorption.(Matsuguchi, Harada, & Omori, 2014; Yantchev, Strashilov, Rapp, Stahl, & Avramov, 2002).

However, polymer-based gas sensors consist some disadvantages which will hinder the overall gas sensing performance. These including long-time instability, poor reversible reaction and poor selectivity. It also has low mechanical stability as many of the polymer will need to be doped with different type of material to enhance its mechanical stability (Xiao Liu et al., 2012).

2.2.2 Carbon nanotubes (CNT)

Carbon nanotubes are cylinder's structure formed by curling a graphene sheet along the axial direction. Fullerene like hemispherical molecules is used to cover the ends of CNTs. CNT has also found itself a favourable choice of material used for gas sensing application. Because of its great sensitivity to target gases as a result of high nanotube electrical transport and thermopower, CNT is widely used in gas sensing applications(Mittal & Kumar, 2014).

CNT also offers a number of additional benefits, such as requiring fewer elements for a response owing to their high surface to volume ratio, which is characterised by a conductance that is easily perturbed by gas molecules. Gas molecules adsorbed on the surface of carbon nanotubes alter electrical characteristics such as resistance and capacitance. CNT based sensor are widely used for detecting gases in physiological parameters, environmental and industrial applications. CNTs are also useful as additives in polymers and catalysts, electrochemical sensors, energy conversion, lithium batteries, nanoprobes, and supercapacitors, among other applications. As a result, they hold a lot of promise for the creation of chemical and biological sensors.(L. C. Wang et al., 2011).

CNT has electrical characteristics that allow sensitive detection of tiny volumes of gases such as alcohol, NH_3, CO_2, and NO_x when used in gas sensing. Generally in gas sensing application, CNTs could be classified into single-walled carbon nanotubes (SWCNTs) and multiwall carbon nanotubes (MWCNTs)(Espinosa et al., 2007; K. Lee, Lee, Dong, & Ju, 2008).

Despite the benefits of CNT material used as a gas sensing material, it also facing some fundamental disadvantages which will hinder the fabrication of gas sensor. Firstly, the downside of CNTs is the higher cost of material production, the fabrication process also much more complicated and relatively challenging compare with other conductive

material. Producing defect-free carbon nanotubes with length up to few micrometres is challenging task either. CNT-based sensors are usually operate in a higher operating temperature, which limit its experimental application in laboratory equipped conditions (Cantalini et al., 2004; Han, Nag, Chandra Mukhopadhyay, & Xu, 2019)**.**

2.2.3 Semiconductor metal oxide (SMO)

Among many gas sensing material such as, 2D carbon base material and polymer based material, SMO possess superior sensing ability due to its unique properties, such as high electrochemical performance, wide bandgap(de Castro et al., 2017) and excellent photo-chromic and electro-chromic performances(K. K. Singh et al., 2017). When comparing with nanostructure SMO, it also possessed improved chemical, physical and mechanical properties. This is due to the rise of quantum confinement phenomena and their significant features such as high surface-to-volume ratio which result in higher overall surface area when comparing to the bulk structure counterpart. (Ji, Zeng, & Li, 2019; Sun et al., 2012).

Nanostructure SMO can occur in several structure based on the type of synthesis method, ranging from 0D (zero dimension). In 0D all three spatial dimension are in nanoscale such as quantum dot and nanoparticles. Secondly, the 1D (one dimension) such as nanorods, nanowhiskers, and nanowires where two spatial dimensions of the structure are in nanoscale range. Thirdly, the 2D (two dimension) as only one spatial dimension is in nanometre range. These structures include nanoflakes, nanospheres, and thin film. Lastly, 3D (three dimension) are the material with any spatial dimension placed close together in contact and forming an interface(E. Lee, Yoon, & Kim, 2018; Nunes et al., 2019). Nanostructure SMO are researched extensively due to the benefits mentioned previously, in addition they are also widely abundant, low cost in fabrication, chemically

stable, and wide engineered potential in term of optical and electrical characteristic. The significance properties of these metal oxide materials apart from any structure of it built up are its wide band gap energy, high carrier mobilities, high dielectric constant, high optical transparency, and superconductivity. These are the properties that make nanostructure SMO shines among the other in electrical and optical based application(Chavali & Nikolova, 2019; Khan, Bhatti, Qindeel, Althobaiti, & Alonizan, 2017).

There are many influencing factor that affect the sensing ability of nanostructure SMO as annealing is one of the methods often use to improve its sensing performance. Annealing is a process where extreme heat is applied onto the material for a certain time. Annealing can be done is ambient air or even other types of gas for different final properties. It has found that by annealing SMO sample will bring some morphology changes, better crystallinity, oxidation state changes and also optical properties changes toward the material. It was found that by undergoing annealing process for SMO sample will bring some significant improvement on the properties especially the electrical and the optical properties(Y. Ren, Yuan, Fan, Huang, & Shuai, 2018; L. L. Yang, Zhao, Willander, Yang, & Ivanov, 2009; S. Yang et al., 2019a). This is due to many reasons such as the change of the non-stoichiometric species in the material which improve chemisorb oxygen species and the alteration of the band gap in the material. Shulin yang and team reported an improved gas sensing performance α-MoO_3 by annealing in reducing gas(S. Yang et al., 2019a). this proved a simple heating process to improve the gas sensing ability of an intrinsic SMO without much complicated process.

These interesting features of SMO nanostructure has found itself exhibiting a beneficial condition for material-gas interaction. In addition, nanostructure SMO has all the advantages which aligned with the objectives of this work. Hence, SMO nanostructure is chosen to be the sensing material for this work

2.3 Semiconductor metal oxide (SMO) for optical sensing

SMO are generally ionic compounds which consists by one positively charged metallic and negatively charged oxygen ions. It can behave in the form of a metallic material, semiconductor or insulator characteristic depending on the external condition of the material. In most metal oxide species, the electrons are fully filled in the s-shells of positive metallic ions. However, their incompletely filled d-shells are the reasons of the multiple characteristics in electronic and optical properties. This interesting property is what allows this material to conduct electricity in specific situation. SMO are classified into two different types, which is *n*-type, in which the majority charge carriers are electrons, and *p*-type, in which the majority charge carriers are holes. Almost all properties of metal oxide such as electronic and optical properties are able to be engineered and tuned by changing their structure, size, chemical compound, and stoichiometry of the element using different synthesis and treatment method.

Furthermore, the electronic structure metal oxide is categorised into two major categories, which are the transition metal oxide and non-transition metal oxides. Firstly, transition metal oxides (Fe_2O_3, NiO, Cr_2O_3, etc.), they exhibit relatively small energy differences between a cation configuration. This small energy differences allow quick transformation of oxides between the different states, which have a downside of unstable properties. However, the non-transition metal oxides consist of both the pre-transition and post-transition metal oxides. Pre-transition metal oxide behave quite stable because they have large and wider band gaps. This wider band gap prevents the instant formation of holes and electrons. They are rarely chosen as gas sensor materials due to their poor electroconductivity behaviour. In the other hand, the more stable metal oxides are the one with d^0 and d^{10} electronic configurations. Transition-metal oxides such as, TiO_2, V_2O_5 and WO_3 are found to have the d^0 configuration, where post-transition-metal oxides, such as ZnO or SnO_2 have d^{10} configuration. Hence, more d^0 and d^{10} configuration of metal

oxide are often used in gas sensing application(Ananya Dey, 2018; C. Wang, Yin, Zhang, Xiang, & Gao, 2010a).

In this work, the author will be focusing on the optical properties of the nanostructure SMO as the sensor chosen in this work is an optical fiber based gas sensor, The optical properties of a metal oxide are closely related to its electrical properties because the electric field component of light can interact with the electrons of the metal oxide according to the Drude free electron model(X. Zhang, Wu, Amrehn, & Wagner, 2019). Usually, the SMO optical properties can be explained based on the band gap of the material. There are two types of band gap in SMO which is the direct and the indirect band gap. The direct band gap require photon to excite an electron from the valance band to the conduction band. Meanwhile the indirect band gap needs a phonon plus photon to excites an electron from the valence band to the conduction band. When the electron is falling from the conduction band, the photon is emoted in a formed of light. Depending on the band-gap value, there is a minimum energy of photon require for the transition to occur. This can be expressed in the equation below,

$$E_g = \frac{hc}{\lambda} \quad \textbf{(Eq 2.1)}$$

Where E_g is the band gap value, h is the plank constant, c is the speed of light and λ is the minimum wavelength. Each of the types of SMOs has its own absorption wavelength which can be identified by the UV-Vis measurement. P.Bharathi et al has reported doped Gd-ZnO nanorod and nanoflowers which resulted in decreasing in band gap. These findings shows that Gd-doped ZnO exhibits a good xylene sensing performance at room temperature(Bharathi et al., 2020). Hence, extensive has been dedicated to explore the potential of band gap modification and alteration for specific light source in specific optical application.

Currently, nanostructures SMO are widely incorporated in sensors regardless chemiresistive or optical gas sensor. This is mainly is due to their high surface-to-volume ratios with different types of nanostructure formation, high surface reaction performance, high catalytic efficiency, and strong adsorption ability. Hence, nanostructure SMO has always been a preferred choice of material in almost all types of gas sensor technology (Nunes et al., 2019).

2.3.1 Review of nanostructure SMO in optical sensor for Ammonia gas sensing application

Based on previous works, there are various works reported on room temperature optical ammonia gas sensing. However, without elevated sensing temperature, SMO still suffers from rapid sensing and low sensitivity. Table 2.2 review the recently reported room temperature ammonia optical gas sensor.

Table 2.2. Table shows the list of recent reported metal oxide nanostructure used for ammonia optical gas sensing (Subramanian et al., 2018; Q. Wang et al., 2020)

Sensing material	Detection limit	Respond time	Recovery time	Operation temp	Ref.
$Zn_3(VO_4)_2$	500ppm	46 mins	59 mins	RT	(Subramanian et al., 2018)
Fe_2O_3 nanotube	3492ppm	>10mins	<4mins	RT	(Fu et al., 2020)
ZnO nanocrystalline	100ppm	11 mins	8 mins	RT	(Devendiran & Sastikumar, 2017)
WO_3 nanorods	3492ppm	14mins	>4mins	RT	(Q. Wang et al., 2020)
GO-ZnO nanocomposites	24ppm	6.9 mins	less than 90 s	RT	(Fu et al., 2018)

2.3.2 Zinc Oxide (ZnO)

Zinc Oxide is the most researched metal oxide material in gas sensing application. It is a n-type semiconductor with high electron mobility, wide band gap (3.37 eV) which explains its good photoelectric behaviour, large exciton binding energy (60 meV), excellent chemical and thermal stability(Marlinda et al., 2012). All these properties are relatively crucial for a gas sensitive material. ZnO exhibits in three different forms of crystal structure arrangement which is wurtzite, cubic zincblende, and the cubic rocksalt which is relatively rare to obtained shown in Figure 2.2. Among all three different crystal structure, the thermodynamically stable wurtzite structure is the most common phase obtained with a space group of P63mc or C6v under ambient condition. Moreover, ZnO is being known with its benefits such as low-cost, environmentally friendly, simple fabrication process and ready for mass batched production(L. Zhu & Zeng, 2017).

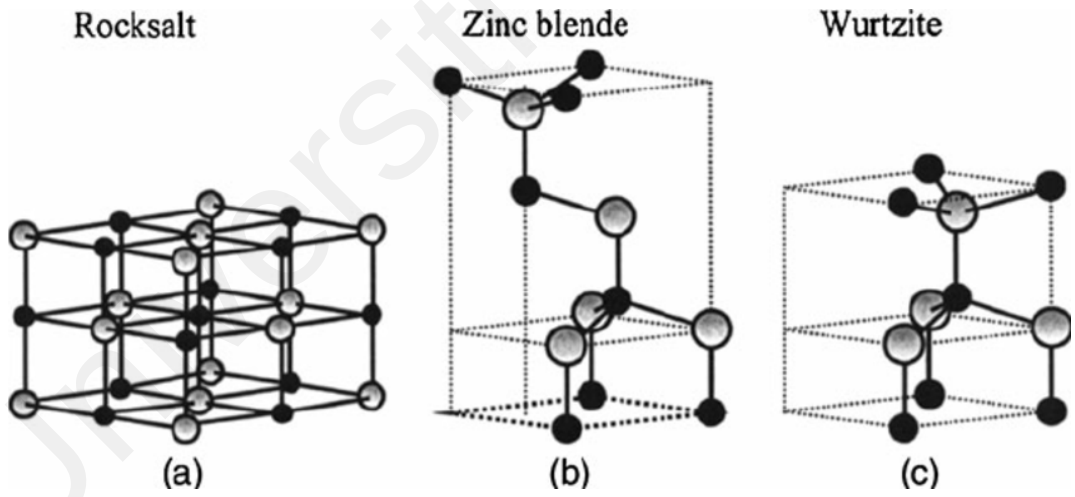

Figure 2.2: Crystal structure of Zinc oxide a) rocksalt, b) Zinc blende and c) Wurtzilite(Espitia et al., 2012).

ZnO is a usually utilized as a sensing material in chemoresistive type gas sensor. The gas sensing mechanism is similar as mentioned previously, which the manipulation of the sensor's resistance when gas molecules interact with the material's surface acts as the measurable signals.(Spencer, 2012).

There are many reported works on Zinc oxide in gas sensing application. For instance, Q.A. Drmosh et al.(Drmosh, Yamani, & Hossain, 2017) reported a high sensitive and short respond time ZnO thin films hydrogen sensor. This is due to the formation of higher oxygen vacancies and more active sites that are responsible for gas sensing performance when the ZnO film was prepared by oxidization of sputtered Zn in low oxygen partial pressure. In addition, Mausumi Das(Das & Sarkar, 2017) reported an ammonia (NH_3) gas sensor in room temperature by fabricating nanocomposite of zinc oxide (ZnO) and polyaniline (PANI). It shows the synthesized ZnO-PANI nanocomposite exhibit fast response time and better stability with highly selective towards NH_3. A B Khatibani(Khatibani, 2021) investigated the relationship of annealing temperature with the ZnO gas sensing ability. the result concluded that the sample annealed at 450°C has the outstanding performance as a sensor.

2.3.3 Manganese oxide (MnO_x)

One of the metal oxides that attracted researchers due to its low cost and abundance is manganese oxide (Mn_xO_y). Among all different oxidation states, Manganese dioxide (MnO_2) is one of the widely used materials in wide range of application due to its varieties and uniqueness in structure. The related field implemented using MnO_2 are supercapacitors, rechargeable batteries, catalysts, and magneto electronic devices. In addition, it is also highly research in the application of gas sensing to further understand the interaction of gases with different oxidation states of MnO_2. it mainly focuses on the electrical based sensor similar as the ZnO.

Currently, nanostructure such as nanoparticles, nanorods, nanosheets, nanowires, nanotubes, and nanofibers has been successfully constructed via various chemical methods utilizing the MnO_2. Generally, MnO_2 has a great structural flexibility, and it may

be found in four crystallographic forms i.e., α, β, γ, and δ-MnO_2 shown in Figure 2.3. The fundamental structural unit which is the MnO_6 octahedron is the building blocks by linking and connecting in different ways. MnO_2 may be classified into three varieties based on the distinct MnO_6 links: the chain-like tunnel structure such as α-, β-, and γ-types, the sheet or layered structure such as δ-MnO_2, and the 3D structure such as λ-type(Xiaodi Liu, Chen, Zhao, & Jia, 2013).

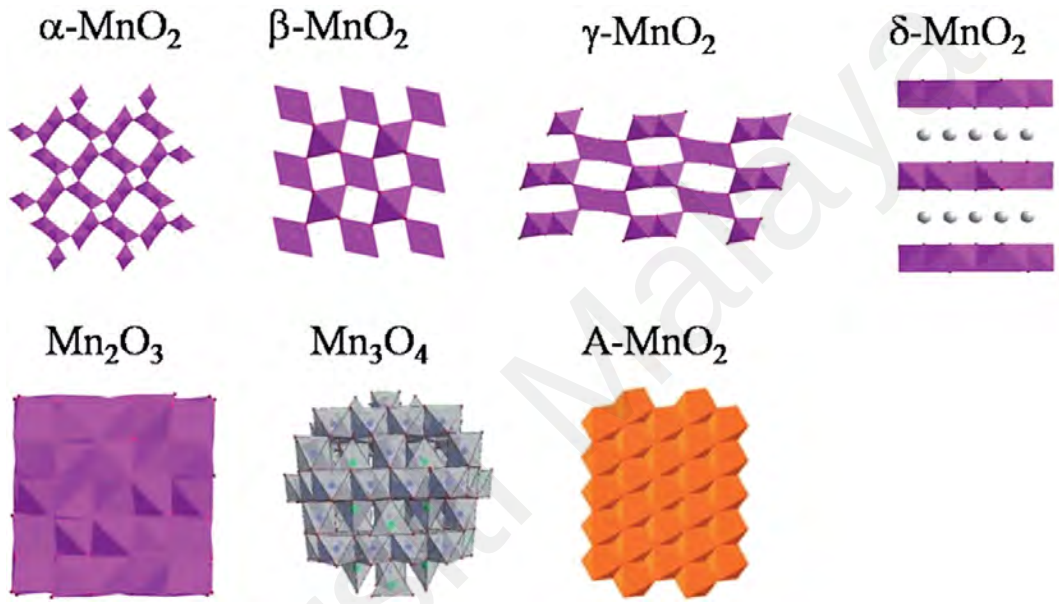

Figure 2.3: Structural representation of manganese oxides used in this study: α-MnO_2, β-MnO_2, γ-MnO_2, δ-MnO_2, Mn_2O_3, Mn_3O_4 and A-MnO_2(Y. Liu et al., 2015)

There are several work reporting MnO_2 as gas sensing material. for instance, Chenshitao Liu et al(C. Liu et al., 2017) reported an ethanol gas sensor utilizing α-MnO_2 nanorods synthesized via simple and cost-effective hydrothermal method. The gas sensor shows superior reproducibility and stability when exposure to ethanol interaction at a higher working temperature. It assured the potential of α-MnO_2 NRs as a promising sensing material in ethanol-based gas sensors. Moreover, an NH3 sensor using cryptomelane type octahedral molecular sieve of manganese oxide (K-OMS-2) has been reported by Robin Kumar et al(R. Kumar, Kumar, Kushwaha, & Mittal, 2016). The

presented sensor has relatively short response and recovery times (approximately 70 s and 85 s). In addition, it is able to detect up to 5 ppm NH_3 at room temperature and response is reversible with no hysteresis for NH_3.

2.3.4 Molybdenum oxide (MoO_3)

Among all SMO, MoO_3 can be consider the most adaptable and functional optical and electronic oxides as it has much unique properties such as wide stoichiometric, high electrochemical activity, wide range of oxygen state, a wide bandgap energy of approximately 3 eV , and low thermal dynamic stability. (de Castro et al., 2017)These properties have provided a superior platform for MoO_3 to be beneficial in advance optical application. MoO_3 can exist in 3 different phase, α-orthorhombic phase, β-monoclinic phase and *h*-MoO_3 (hexagonal structure) shows in Figure 2.4. (a), (b) and (c) respectively. α-MoO_3 has an orthorhombic crystal structure. It consists of stacked, double-layered MoO_6 octahedra building blocks formed by edge-sharing zigzag rows and corner sharing rows held by van der Waal's forces along the [001] and [100] direction, respectively. In the other hand, the β-MoO_3's structure is the same to the cubic rhenium trioxide (ReO_3), as the MoO_6 octahedra shares corners and build up a monoclinic structure. Lastly, the hexagonal *h*-MoO_3 is constructed by the joining the zigzag chains of the MoO_6 octahedra through the *cis*-position running along the c-axis. This hexagonal structure showcase a large one dimensional tunnels along the c direction with a diameter of approximately 3.0 Å, which sufficient to accommodate cations and water molecules (Chithambararaj et al., 2016; Z. Li et al., 2017).

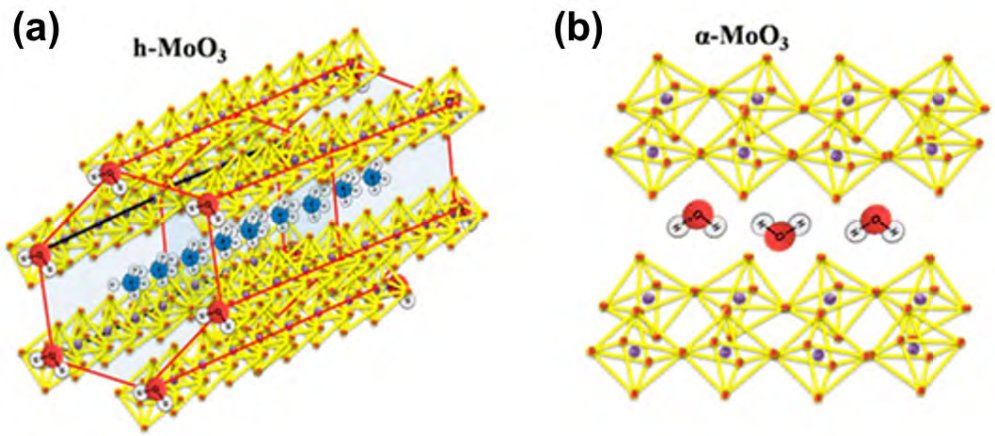

Figure 2.4: Crystal structure of MoO_3 a) *h*-MoO_3, b) α-MoO_3(Chithambararaj et al., 2016)

5 years ago, Shulin Yang et al. has develop a highly responsive H_2 gas sensor using α-MoO3, which shows response time of 14.1 s toward 1000 ppm of H_2 in room temperature with no catalyst added(S. Yang et al., 2015). Dongwook Kwak and team has also showed the potential of α-MoO_3 to detect NH_3 at concentration at low as 50 ppb with operating temperature at 450^{o}C (Dongwook Kwak et al., 2019). Last year, Surendra Kumar and team has try to challenge the working temperature of the ammonia sensor at 200^{o}C using *h*-MoO_3 which shows responds from 5 ppm-100 ppm (S. Kumar et al., 2020).

Many works have been put on to explore the sensing properties of ZnO and also MnO_2 but not much attention on the metastable phase *h*-MoO_3 which have really interesting hollow rod like structure and a unique optical property which is highly advantages in this work. in addition, there has been no research using MoO_3 in an optical gas sensing system so far. Hence, the author proceeds with MoO_3 as the metal oxide of choice to be the gas sensing material in this work.

2.4 Method to obtain Semiconductor Metal Oxide Nanostructure

There are various techniques to synthesize SMO nanostructure ranging from physical method and also chemical method such as vapour deposition, pulse laser deposition, spray pyrolysis, sputtering, and also reaction including: hydrothermal, chemical bath deposition and sol–gel(de Castro et al., 2017; Inpan et al., 2018; H. Ren et al., 2018). In this work, the author is focusing more in solution-phase chemical synthesis method due to is simplicity on instrument usage and lower cost of fabrication. The benefits of using the chemical methods are that particles with a defined size, dimension, composition and structure are able to be produced and fabricated. Such characteristic of nanostructure is highly useful in various applications such as catalysis, electronic devices and in most importantly in sensing fields.

2.4.1 Hydrothermal

The hydrothermal technique is one of the most widely utilised, offering a solution-based chemical approach for the production of various types nanostructured materials. The technique offers several advantages, including the ability to modify the crystal structure, morphology, and size by adjusting the reaction conditions, such as reactant precursor, reaction temperature, reaction duration, types of solvent medium, and additives. Furthermore, the synthesis is low-cost and ecologically benign, resulting in a high degree of chemical uniformity on a molecular scale. (Chithambararaj et al., 2016)

Crystal synthesis or crystal growth at high temperature and high-pressure water conditions substances which are insoluble in ordinary temperature and pressure (< 100°C, < 1atm) is known as hydrothermal synthesis. Hydrothermal synthesis is generally carried out below 300°C because ionic product (K_w) has a maximum value of approximately

250–300°C. As 374 °C and 22.1 MPa are the critical temperatures and pressures for water, respectively. (Adschiri, Hakuta, Sue, & Arai, 2001). An autoclave (thick-walled steel cylinders) holding solvent (water) and dissolved/suspended precursors is used in the hydrothermal method. Microwave-hydrothermal therapy using integrated equipment has been widely utilised in laboratories for the past 20 years. (Nikam, Prasad, & Kulkarni, 2018).

The major benefit of the hydrothermal technique is the potential of crystalline phases forming, which are unstable at the target compound's melting point. However, the primary downside is the requirement for costly equipment. Changes in pressure, temperature, solvent, reaction duration, or precursor ratio can be used to alter morphology and crystallinity of produced materials. Hydrothermal reactions in water are more appropriate for green chemistry applications since they are ecologically benign, and they are widely used to produce a range of materials. This technique also provides for little reactant loss and often greater product yields, making it particularly helpful for obtaining classic and less-common nanostructures with desired form and size control: powders, films and especially one- to three-dimensional nanocrystals(Kharissova, Kharisov, González, Méndez, & López, 2019)

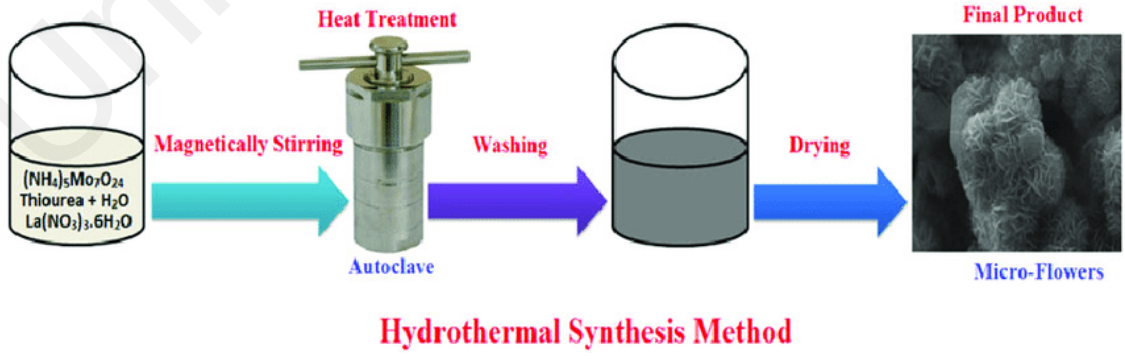

Figure 2.5: Hydrothermal synthesis process for 3D flower-like MoS_2 nanostructure(Nadeem Riaz et al., 2019)

As shown in Figure 2.5, Khalid Nadeem Riaz et al. reported a simple and cost-effective hydrothermal technique to fabricate three-dimensional (3D) flowerlike MoS_2 nanostructures by changing the hydrothermal temperature (180°C, 200°C, and 220°C) and reaction time (6, 12, 24, and 36 hours). The sample produced at 200°C for 24 hours had a 3D flowerlike MoS_2 nanostructure with hexagonal phase structure, according to the findings in SEM & XRD (Nadeem Riaz et al., 2019). For highly sensitive and selective ethanol gas detection, indium oxide nanocubes (NCs) were produced using a simple, template-free hydrothermal technique at low temperature by Thuy T.D. Nguyen et al(Nguyen et al., 2020). The superior sensing performance of the synthesised In_2O_3 NCs is due to its unique properties, which include a large BET surface area and BJH adsorption average pore diameter, as well as an abundance of sharp edges and tips, resulting in high surface to volume ratios for gas adsorption and diffusion processes. Cheng Li et al on the other hand, reported a unique construction of porous butterfly-like hierarchical SnO_2 3D structure assembled by 2D SnO_2 nanosheets. It was formed by annealing SnO nanostructures that had been produced through a simple hydrothermal method. The as-synthesized butterfly-like SnO_2 structure has an extremely high gas sensing sensitivity and a strong selectivity for acetaldehyde at the optimal operating temperature of 243 °C. It also has a ppb detection limit of 78.7 for acetaldehyde at 500 ppb(C. Li et al., 2020).

2.4.2 Sol gel

The sol–gel technique is a well-known synthetic methodology for producing high-quality SMO nanostructures and mixed oxide composites. The texture and surface characteristics of the materials may be controlled very well with this approach. Hydrolysis, polycondensation, ageing, drying, and thermal breakdown are the five main stages in the sol–gel technique. as described in Figure 2.6.(Parashar et al., 2020)

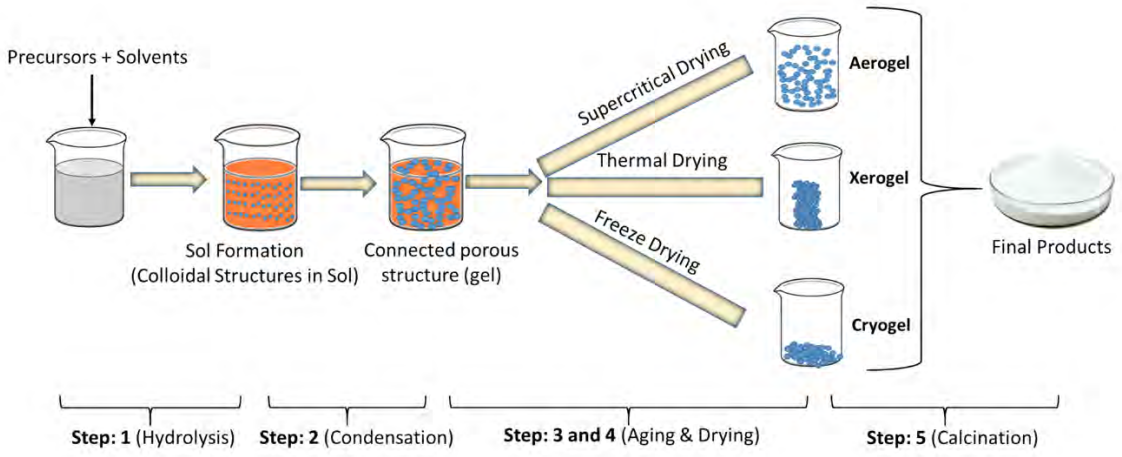

Figure 2.6: Steps involved in sol–gel process to synthesize SMO nanoparticles (Parashar et al., 2020)

To allow condensation to occur, zero-charge precursor molecules with a particular water / hydroxyl content must be generated before nucleation can begin. The accumulation of precursor molecules causes supersaturation, which allows nucleation to occur once the precursor concentration exceeds the nucleation threshold. It is possible to develop from a supersaturated solution until the solid reaches' saturation concentration. Aging can affect the average particle size and size distribution after nucleation and growth. Aggregation and coarsening are the two most important processes, both of which are highly dependent on the experimental conditions. The ultimate particle size and size distribution are determined by the intricate interaction between the rates of precursor production, nucleation, growth, and ageing (Niederberger, 2007; Oskam, 2006).

There are a few recent works reporting the fabrication of metal oxide gas sensor using so-gel method. for instance, B. C. Yadav et al(2016) reported synthesizing nanostructured ferric oxide humidity sensor using sol–gel method. The spin coating method was used to create thin ferric oxide coatings. The sensor's reaction and recovery times were determined to be 12 and 9 minutes, respectively. In addition, Anup Dey et al(2018). have reported the development of ZnO nanostructure on p-silicon (100) substrates using a sol–

gel technique followed by a dip-coating approach for use as a hydrogen gas sensor. The results demonstrate that as the annealing temperature rises, the sensitivity improves substantially, with maximum sensitivity at 550°C annealing temperature and 150°C operating temperature. Amol R. Nimbalkar and team(2017) previously reported the development of a zinc oxide (ZnO) nanostructure H_2S sensor using a facile sol-gel spin coating method. At 300°C working temperature and 100 ppm gas concentration, the maximal gas response is reached towards H_2S gas.

Similar with hydrothermal method, sol-gel method doesn't provide a direct growth of SMO nanostructure on the desire substrate. An additional deposition steps such as spin coating and drop casting will need to be performed in order to coat the nanostructure on the substrate. Even by using spin coating and drop casting, we are unable to obtain an overall coating of nanostructure on the optical fiber substrate used in this work. Hence, a method that enable full coat of SMO nanostructure is more suitable to carry on.

2.4.3 Chemical bath deposition (CBD)

Among all these deposition technique, chemical bath deposition (CBD) is by far consider the lowest cost and hassle-free method to fully coat the surrounding of the optical fibre. By fully coating the surrounding of the exposed core region from the tapering process, higher interaction of light and sensing material are allowed and hence resulting from a higher absorbance response. Other method such as dip coating or even sputtering process only allow for single sided surface coating as the substrate will only exposed one side during deposition. Unlike CBD, the whole substrate is immersed into the chemical precursor for deposition. CBD technique is considered an inexpensive and a simple deposition method, as it also able to produce relatively high crystalline phases nanostructure shown in Figure 2.7.

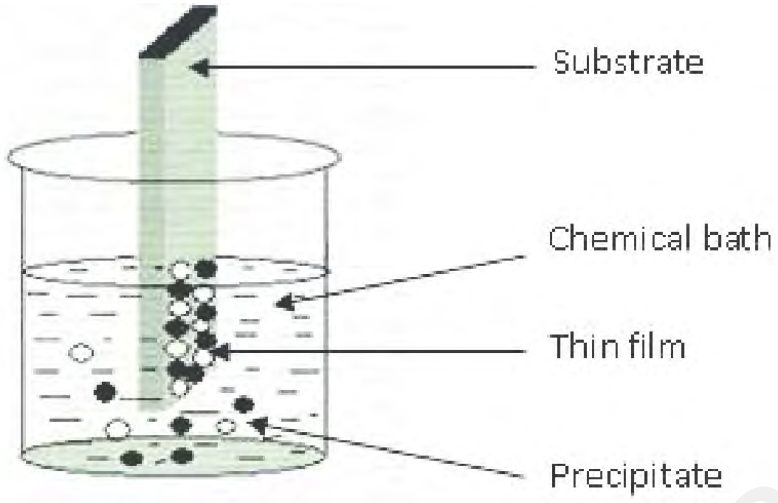

Figure 2.7: Schematic of Chemical Bath Deposition (More et al., 2016)

The overall phenomena of a CBD occur using a liquid starting precursor which will undergoes a chemical reaction at a substrate surface, usually in a solid material. Finally, after the reaction leaving a solid layer of thin film with various form of nanostructure. The substrates were usually cleaned with very high detailed via sonication and dried before the deposition to ensure a clean substrate surface for better coating condition. In the chemical aspect of the formation of the nanostructure in chemical bath deposition, it mostly involves hydrolysis of metal cations which compromised three main steps: First, the creation of atomic/molecular/ionic species from colloidal and nucleation process. Follow by the transport of these species through a medium (in this case is water), and lastly the condensation steps of the species which terminates the growth of the nanostructure. The aim of CBD method is to controlled the precipitation of the desired nanostructure compound from a solution of its starting precursor(B. A. Ezekoye et al., 2012).

For the deposition of nanostructure SMO via CBD, there are two main deposition mechanism that govern the growth of nanostructure: the ion-by-ion mechanism and the cluster mechanism. In the ion-by-ion mechanism, the nanoparticles' nucleation rate is

usually slower and its growth usually happens at the surface of the substrate. However, in the cluster mechanism, the size of the colloids depends largely on temperature. And the deposited colloids' size will greatly affect the product of the crystal. Nucleation therefore is confined to two dimensions for ion-by-ion reaction, unlike for the cluster mechanism which is in three dimensions. Termination of the crystal growth in the CBD reaction occurs when adjacent crystals touch each other or by some other termination mechanism (Hodes, 2007).

Chemical bath deposition method was selected due to many advantages mentioned earlier such as simplicity of instrument set up, lower in cost production, large area of deposition and provide an overall coating of the nanomaterial(B. A. Ezekoye et al., 2012). A beaker to contain the precursor solution and the cleaned substrate which deposition is to be carried out is the only requirements needed for this synthesis technique. Furthermore, stirring action can be added using a magnetic hotplate or a thermostat bath in order to maintain a specific and constant temperature are options that are useful to improve the overall material deposition(Mugle & Jadhav, 2016). There are a few important parameters that can be adjust, for instance the deposition time, reaction temperature, concentration of the precursor, types and concentration of the complexing agent and reducing agent which can ultimately affect the characteristic and the growth of the nanomaterial including particle size, morphology grow and dimension of the nanostructure.

2.4.4 Successive ion layer adsorption and reaction (SILAR)

There is another related technique which is quite similar with CBD which is called the Successive ion layer adsorption and reaction (SILAR) shown in Figure 2.8. In the SILAR method, the selected substrate is first dipped with the first precursor solution for a period of time. Later on, the substrate is removed and rinsed, then dipped again in the second precursor solution(Pathan & Lokhande, 2004). Purpose of this method is to form a monolayer nanostructure during each deposition in different precursor solutions. But comparing with CBD, SILAR have more parameter to fine tune and optimized as there are more procedure in the whole synthesis process which include the rinsing process and also the type of different precursor solution used.

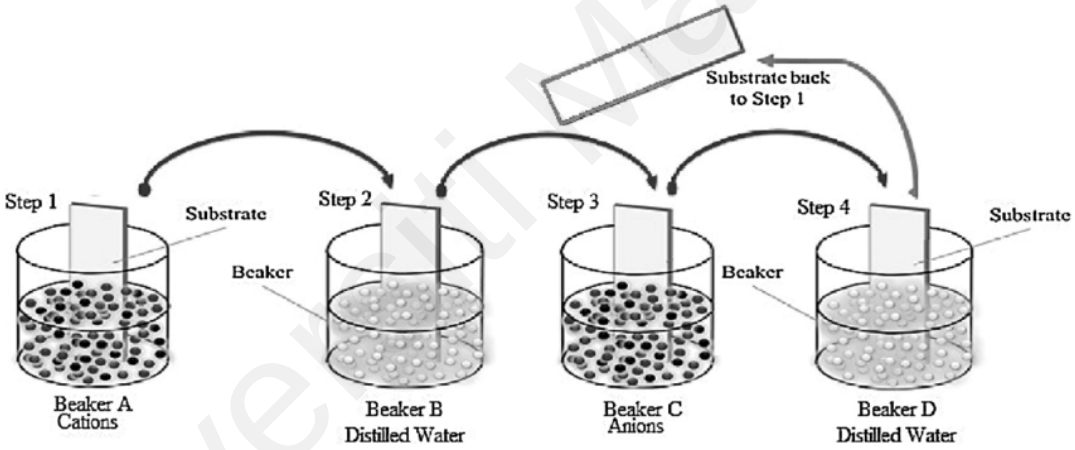

Figure 2.8: The Schematic diagram of Successive Ionic Layer Adsorption and Reaction (SILAR) technique.(Ighodalo et al., 2017)

Many of the author uses CBD to deposit nanostructure SMO for multiple applications. For example, Zhi-yong Xue et al has successfully prepare a MoO_3 film via CBD method(Xue, Xu, Gu, & Ren, 2017). The MoO_3 nanostructure formed were characterized by using a VERTEX70 infrared spectrometer, XRD, SEM and also a UT6 UV/VIS spectrophotometer. The morphology of the MoO_3 nanostructure formed shows large particle form in the beginning of the CBD. After the first 4 hours, smooth MoO_3 nanostructure forms in the solution. Later, there are many large particles formed at the 8^{th}

hours of CBD which might cause by the particle's aggregation. After reacting for 12 hours, more cracks and holes formed. In the light absorption performance of MoO_3, it was reported that the longer the solution reacts, the optical absorbance is higher. The results indicates that the synthesised MoO_3 using CBD method has a good light absorption performance from the findings with an absorbance voltage oof estimated 300-400V.

Arpan Dhara et al. has synthesis a *h*-MoO_3 by using two stage CBD with well aligned nanorod(Dhara, Hodes, & Sarkar, 2014). In his work, Arpan Dhara modified the conventional CBD to a 2-stage deposition which is quite similar to a SILAR method. He also fine-tunes and adjust on the important parameter such as, precursor concentration, effect of different concentration of acid used, different type of substrate gas, deposition time of the first stage and the second stage and how does this change in parameter affect the final morphology of the MoO_3 nanorod formed. In conclusion, it was found that the growth and morphology of the films are able to be controlled using this two-steps process, where the sample were rinsed between each deposition. Nanostructure growth was found occurring at the second stage. The rinsing step in the first stage is responsible for the nanostructure growth initiated by a chemical change of the nucleation centres. Lastly, for the photocatalytic degradation of methylene blue dye was found to be fairly good under irradiation of visible light.

Surendra also uses CBD to synthesis the MoO_3 gas sensor(S. Kumar et al., 2020). In her work, they managed to formed a hexagonal nanorod MoO_3 for low concentration NH_3 resistive gas sensor. The gas sensing performance towards different concentration of NH_3 was tested in an operating temperature of 200^{o}C. They reported the *h*-MoO_3 nanorods formed from CBD method demonstrated a high sensitivity and selectivity performance to low concentration of NH_3 (5ppm).

2.4.5 Review of Semiconducting Metal oxide via Chemical bath deposition

CBD of nanostructure SMO is well established across a wide scale of application shown in Table 2.3. These recent reported works proved nanostructure SMO fabricated using CBD method is suitable for gas sensing applications and especially MoO_3 based devices as NH_3 sensor. For this study, modified CBD inspired by the SILAR method has been chosen to synthesis and coat the MoO_3 nanostructure metal oxide on the tapered optical fiber for NH_3 gas sensor. This method will be explained more in detail in methodology part.

Table 2.3. Table shows the list of reported metal oxide nanostructure synthesised by chemical bath deposition (Anil Kumar et al., 2019; S. Kumar et al., 2020)

Material	CBD process	Morphology	Application	Ref.
CuO	Seed Layer-Assisted CBD	Thin film	-	(C. Zhu & Panzer, 2014)
CdS	Single stage CBD	Nanoparticles	Solar cell	(Kozhevnikova, Vorokh, & Uritskaya, 2015)
Al_2O_3	Single stage CBD	Nanoparticles	Buffer for CNT deposition	(H. Wang & Na, 2015)
ZnO	Microwave-assisted CBD	Nanorod	Photosensitive UV detectors	(Husham et al., 2017)
ZnO	Single stage CBD	Nanorod	-	(Terasako et al., 2019)
MoO_3	Single stage CBD	Nanoparticles	-	(Xue et al., 2017)
MoO_3	Two-stage CBD process	Hexagonal Nanorod	Photocatalytic degradation of MB dye	(Dhara et al., 2014)
h-MoO_3	Single stage CBD	Hexagonal Nanorod	NH_3 gas sensor	(S. Kumar et al., 2020)
$MoNiO_4$	Single stage CBD	flower-like nanostructure	Super capacitor	(Anil Kumar et al., 2019)

2.5 Optical fiber

2.5.1 Structure of an optical fiber

There are basically two types of silica glass optical fiber that are used as gas sensor, which is Single mode fiber (SMF) and Multimode fiber (MMF). The different of these two fiber is SMF has smaller core diameter (around 9 micron) that only support one mode of light to propagate meanwhile, MMF with a larger diameter core of 62.5 micron allows multiple modes of light to propagate inside the fiber. In addition, MMF are also feasible for sensing application used in visible-near infrared range of wavelength which is the set up for this project. MMF provides low attenuation loss and resilient in high temperature which make its characteristic suitable to be used in ammonia gas sensing. Figure 2.9 shows a cross sectional diagram of a fiber optic component which comprises of glass core and cladding, primary and secondary buffering(Sabri, Aljunid, Salim, Ahmad, & Kamaruddin, 2013).

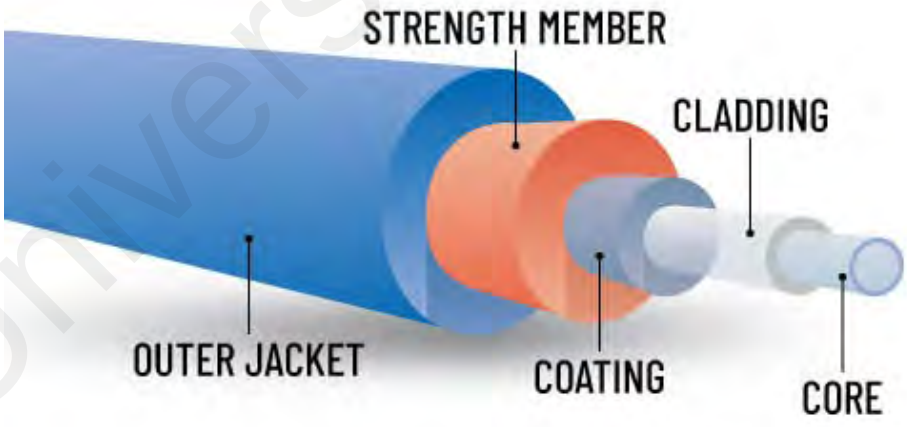

Figure 2.9: Fiber optic components (Hodgkinson & Tatam, 2013)

Core is the centre of the fiber which made out of silica glass, it is where the light travels and cladding is the outer part that surrounds the core so that the propagated light will not escape from the fiber. The buffer coating is to provide a further protection for the finer

from moisture and damage. When light travels inside the optical fiber, it allows total internal reflection (TIR) as shown in the Figure 2.10.

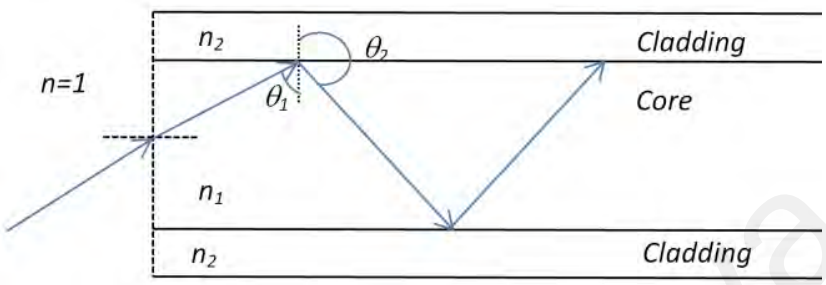

Figure 2.10: Total internal reflection (TIR) in optical fiber (Y. nan Zhang et al., 2017)

Total internal reflection only happens when the incident ray / light exceeds the critical angle. This can be explained in the mathematical equation below.

$n_1 \sin_1 \boldsymbol{\theta} = n_2 \sin 90^o$ (Snell's law)

Since $\lambda_1 = \theta_c$

Then $\theta_c = \sin^{-1} (\frac{n_2}{n_1})$ .....**(Eq. 2.2)**

Where θ_1 = incident angle, θ_c = critical angle, n_1= refractive index of core and n_2= refractive index of cladding.

2.5.2 Evanescent wave

The idea of evanescent wave is important in optical fiber sensing as the working mechanism is highly related to it. The change of evanescent wave alters the transmitted

light escape from the fiber, which eventually acts as a signal output for the sensor. Hence, it is critical to understand the concept of an evanescent wave before looking into the sensing mechanism of an optical fiber sensor. In optical science, when light from a certain light source shines at an interface between an two medium with different value of refractive index, the angle of incidence from the side of higher refractive index will be greater than the critical angle corresponding to the interface(Sharma, Gupta, & Sharma, 2019). This resulting the total internal reflection where a complete reflection of a ray of light back into the denser medium (optical fiber core), creating a mirror like phenomena.

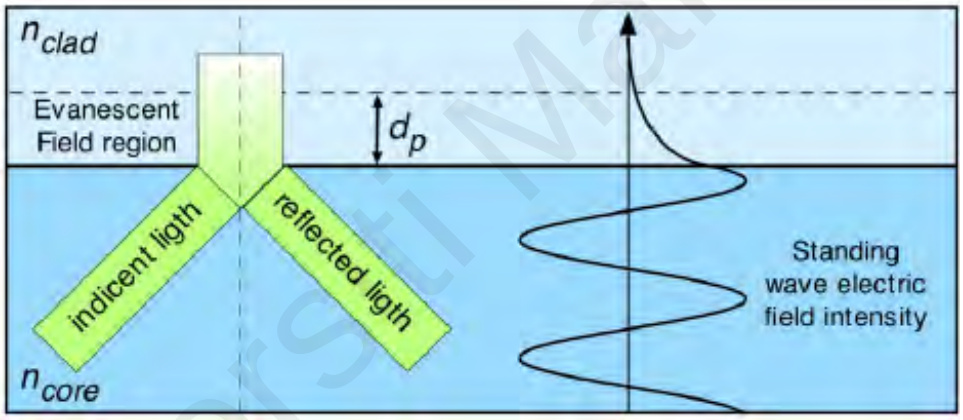

Figure 2.11: Evanescent field in the core/cladding interface of an optical fiber(J. Gouveia et al., 2013).

Taking a closer look at the light interaction interfaces, the ray of light does not actually reflect immediately when reaching the interface between two mediums. However, superposition occurs on the reflected light with the incident light resulting the creation of a standing electromagnetic wave with a certain intensity, this standing electromagnetic wavefront is perpendicular to the interface shown in Figure 2.11. This phenomenon is called the evanescent wave(J. Gouveia et al., 2013).

Evanescent wave plays an important role in optical fiber gas sensing technology as it propagates externally from the fiber core and react with the surrounding material. When the light propagates in the optical fiber and meet the requirement of a total internal refraction, evanescent field is generated at the interface between the core and the cladding which penetrates only a short distance but transfer energy to the cladding. The intensity of evanescent fields decays exponentially away from the interface. (Ke, Tang, Lai, Dai, & Zhang, 2018; Samavati, Samavati, Ismail, Othman, & Rahman, 2019; Tabassum & Kant, 2020). The penetration depth, d_p of evanescent filed in the cladding can be expressed in equation 2.3.,

$$d_p = \frac{\lambda}{2\pi\sqrt{n_1^2 sin^2\theta - n_2^2}} \quad \textbf{(Eq.2.3)}$$

In which θ is the angle of incidence, n_1 and n_2 are the refractive index of the core and cladding respectively, and λ is the wavelength of the light source. This evanescent field can be utilized for sensing application by removing the cladding so that a direct contact of light matter interaction can be formed.

Sensing design for optical fiber gas sensor can be categorized into two main types which is the intrinsic and extrinsic sensors. The intrinsic sensors refer to the interaction between gas molecules and he element in the optical fiber itself. The interaction alters the light transmission properties. Meanwhile. Intrinsic sensors use immobilised indicator (sensing layer) coated on optical fiber. Physical/chemical properties of sensing layer change when reacted with gas molecule hence. Influence the light transmission. In this work, the extrinsic sensor type has been chosen due to its simplicity in development and higher sensitivity towards target gas(Sabri et al., 2013).

2.6 Optical fiber gas sensor

In the current optical fiber gas sensing technology, evanescent field ammonia sensing method the most commonly used so far. In order to maximised the exposure of evanescent wave to allow a better sensitive signal obtain, many modifications have been done towards the fiber with only one goal in mind: to expose the core region.

2.6.1 Modification of optical fiber for gas sensing

Generally, the types of the modifications of optical fiber categorised as etched optical fiber, tapered optical fiber, or side-polished optical fiber which shown in Figure 2.12. All these modifications of the fiber will follow by a coating of a gas sensitive material on this core-exposed optical fiber for a better gas-material interaction. For now, we will only discuss the types of modification of the fiber. First, the modification by etching method is achieved by removing the polymer cladding of the optical fiber using high concentration hydrofluoric acid (HF) or by pulling the fiber in an IR laser-beam(Rickelt, Ottosen, & Kühl, 2015). In the other hand, to modify a side-polished optical fiber, standard fiber is embedded in a rig with grooves and by polishing them mechanically. This method uses a customised rid that have precisely calculated grooves and only allow the cladding being exposed for polishing process(Tseng & Chen, 1992). Lastly, for the modification of a tapered fiber can be produced by gently stretching an optical fiber while it is heated with a fusion machine which also require a relatively high temperature(Abduldaem Mohammed & Hanif Yaacob, 2020; Y. nan Zhang et al., 2017).

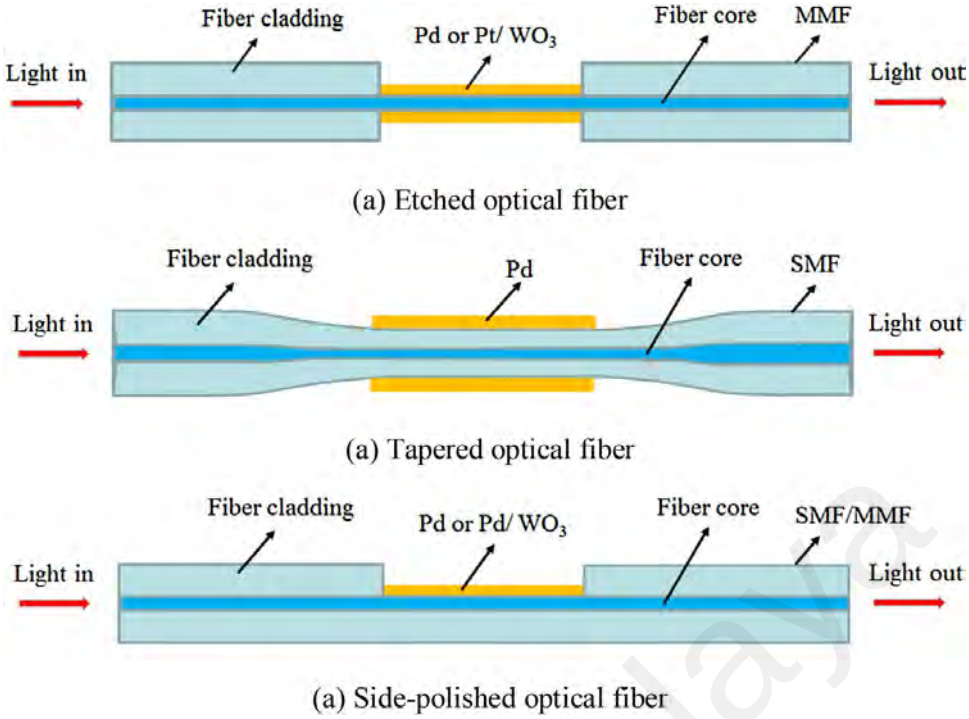

Figure 2.12: Schematic probe structures of different optical fiber sensors based on evanescent field sensor(Y. nan Zhang et al., 2017).

Erfan Owji and team (Owji, Mokhtari, Ostovari, Darazereshki, & Shakiba, 2021) reported a humidity sensor by fabricating using an etched-fibers coated with 2D layers Molybdenum disulfide (MoS_2), Molybdenum diselenide ($MoSe_2$) and composition of graphene and graphene oxide (G/GO). They reported that the etched fiber coated with G/GO has relatively high response (>30%).

Side-polished fiber are often fabricated by polishing a curved SMF embedded in. The cladding region on one side of the fiber can then be removed by mechanically polishing. The downside of this method are its time-consuming fabrication process and difficulty to fabricate long length or fibres in small diameter as optical fiber are relatively fragile without the cladding (Jin, Ho, Cao, Ju, & Qi, 2013a). Tang jie Yuan et al had demonstrated a volatile organic compound (VOC) gas sensor using cholesteric liquid crystal film coated on side polished fiber (CLCFC-SPF). It is found that the pitch of the

CLCF increases with VOC gas concentration, which reduces the refractive index (RI) of CLCF and results in a blue shift of the resonant dips (Tang et al., 2018). This prove that a simple polished optical fiber provides a linear measurement for VOC gas.

R. Kanmani et al (2019) has also reported an investigations of a side polished optical fiber silver (Ag) surface plasmon resonance (SPR) sensors integrated with titanium oxide (TiO_2). Their work focusing more towards the SPR phenomena of the Ag layer for refractive index sensing using side-polished optical fiber with the integration of TiO_2. They reported an improve of sensor performance in term of sensitivity when 30 nm thickness of Ag layer combined with a dielectric TiO_2. It shows a relatively good sensitivity with reading of 268 nm/RIU and a detection limit of 0.012. This work demonstrated the developed sensor is sensitive towards alcohol sensing.

Both etched and side polished have a certain limitation on fiber fabrication consistency and low repeatability in producing the same dimension profile. Hence a tapered optical fiber is a way to look into.

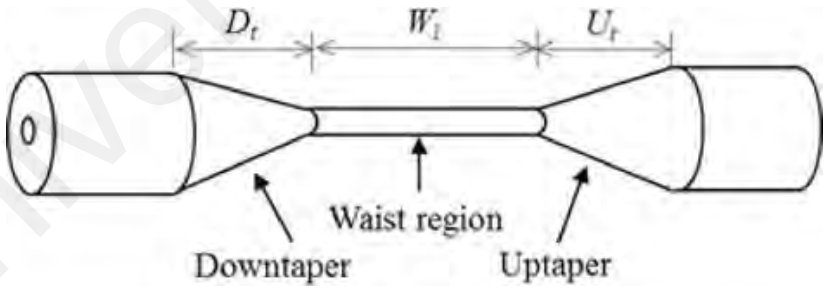

Figure 2.13. Tapered optical fiber labelled with down tapered, waist region and up tapered(Korposh et al., 2019).

Among all modification, the simplest methods for exposing more core region and without hindering the overall mechanical strength is to taper a relatively short portion of the optical fibre as shown in Figure 2.13. This modification allows the formation of evanescent wave all over the tapered parameter, improving the light-material interaction

with the surrounding material and allowing the measurement of changes of optical transmission. The structure of a tapered optical fibre consists of a waist section, where it is the section with reduced total diameter with a greater reduction on cladding compare with the core; up/down taper region, which is the two conical sections where the joint region of tapered section with the untapered surrounding fiber. There are three main factors which will affect the optical properties in term of optical fiber modifications. Which is the length of the up/down tapered sections, the overall diameter of the taper waist and the refractive index of the surrounding material used. These changes of the parameter will generally affect to the intensity of the evanescent wave generated. Tapered optical fibres provides a wide range of interesting characteristics for sensor fabrication which includes larger generation of evanescent fields, high adaptability and compact in size. It was reported that the size and diameter of the waist and tapered will effect on the sensitivity of the sensor (Yahya et al., 2020). This is caused by the depth of the penetration of the evanescent wave field towards the sensing layer. By inducing a functional material onto the tapered region of the optical fiber, the properties of the waveguide can be improved and increased when the material interact with specific gases. Previously, tapered optical fibres were used for the manufacturing of directional couplers. However in these recent years, tapered optical fibres have also found applications in sensor development, polarizers, submicron wire, light amplifiers and near and far field microscopy (Korposh et al., 2019).

A very recent development of tapered optical fiber coated with carbon nanotubes (CNT) for flammable liquids such as ethanol in remote sensing applications (Khalaf, Hasan, Abdulbari, Kadhim, & Yaacob, 2021).The proposed sensor are able to transfer signals using optical fiber with a distance of about 3 kilometres from the sensor location. They have reported that the remote sensor exhibits fast response (8.7 s) with very short recovery time (18 s). The relative absorbance of stable 26% when exposure to ethanol

(100%) and a relatively good repeatability test. The sensing mechanism of this work is believed to base on the interaction between ethanol molecules and the proposed CNT sensing layer. The tapered optical fiber allows a better interaction between the evanescent field and the light sensing material with the chemical analytes.

All of these methods in producing evanescent wave have its own advantages and disadvantages. The tapered method has been selected for this work due to its reproducible and the dimension of taper can be controlled via advance equipment available in the lab. The process is also simple and relatively fast. The tapered optical fiber can utilized by coating it with metal oxide nanostructure that is sensitive to NH_3. Chemical interaction of between the sensing layer and target gas will change the optical properties of the material. The analyte concentration also can be quantified from the light absorbance measurement.

2.6.2 Optical measurement techniques in gas sensing

By modifying the optical fiber allow a better exposure of evanescent wave from the core region, but only tapering the optical fiber is insufficient to obtain high response. The sensitivity of the sensor is still considered low if only bare optical fiber is use, this is due to the weaker light-gas interaction. Hence different functional nanomaterial has been used to integrate with the optical fiber to enhance the overall sensitivity as light-matter-gas interaction is much more superior compare to only light to gas(Yao et al., 2019). In this work, indirect optical spectroscopy approached has been used by applying NH_3 sensitive semiconductor metal oxide (SMO) layer. SMO stands out due to its advantages such as, simple to fabricate, low cost and sensitive with suitable catalyst. SMO are also used for detecting various gases such as CO, CO_2, O_2, SO_2, O_3, H_2, Ar, N_2, NH_3, VOCs, LPG, etc because of their distinctive characteristics that able to form a wide range of nanostructure

from 0D to 3D nano/microstructure. These nanostructures are suitable for gas sensing application. Detailed review on the SMO will be discussed in the following part.

Deposition of the nanostructure SMO on the tapered optical fiber is also convenient and the measurement can be done in the visible-NIR wavelength range using inexpensive setup such as optical fiber, silicon photodiode as well as LED. Absorbance, transmittance, reflectance, surface plasmon resonance (SPR), chemiluminescent are typical optical spectroscopy methods used for gas sensing application. In this work, the absorbance technique was selected for this work due to its less complicated setup and ease to perform.

Absorbance is optical signal happens when a light strikes a surface. The light's energy is transferred to the surface of the material thus attenuates the transmission of light passes through the material. The intensity of the absorbance can be quantified as a function of wavelength or frequency. The common range can be used optical sensor are ultra-violet (UV), Visible (Vis) and Infrared (IR) as shown in the Figure 2.14. These ranges are important in chemical sensor due to its radiation energy that is able to change the material atom configuration and electronic states(Hodgkinson & Tatam, 2013). Hence, in this work, visible to near infrared range was chosen to observe on the optical response.

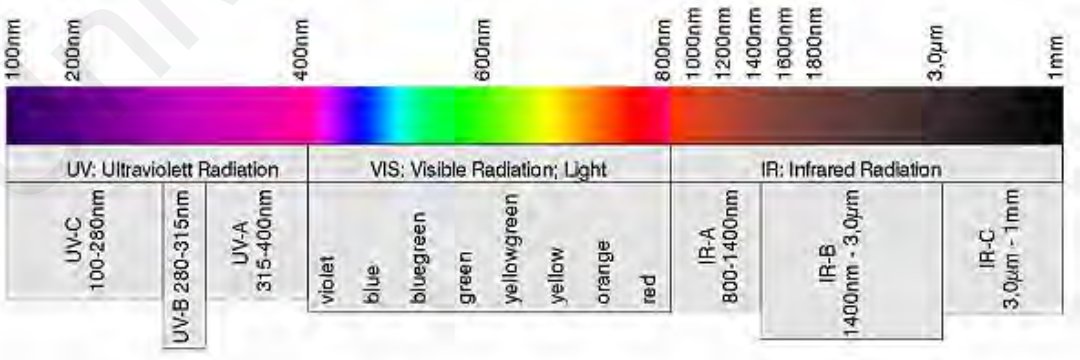

Figure 2.14: Spectra region that can be utilized for optical sensors (Hodgkinson & Tatam, 2013).

To measure the absorbance spectra, the setup only requires a light source, emitting the light signal through sample and a detection system. The light intensity output can be monitored via absorbance measurement. This measurement is based on Beer-Lambert Law which is related to the output intensity with the analyte concentration. Referring to Figure 2.15, for the incident light intensity, I_o pass through cell containing a chemical species with length, I , the output light is given by(Jin, Ho, Cao, Ju, & Qi, 2013b):

$$I = I_o e^{(-alC)} \quad \textbf{(Eq. 2.4)}$$

Where:

a= Absorption coefficient for gas

C= Concentration of the analyte

Equation 2.4 is suitable to be applied for the direct light interaction with the analyte.

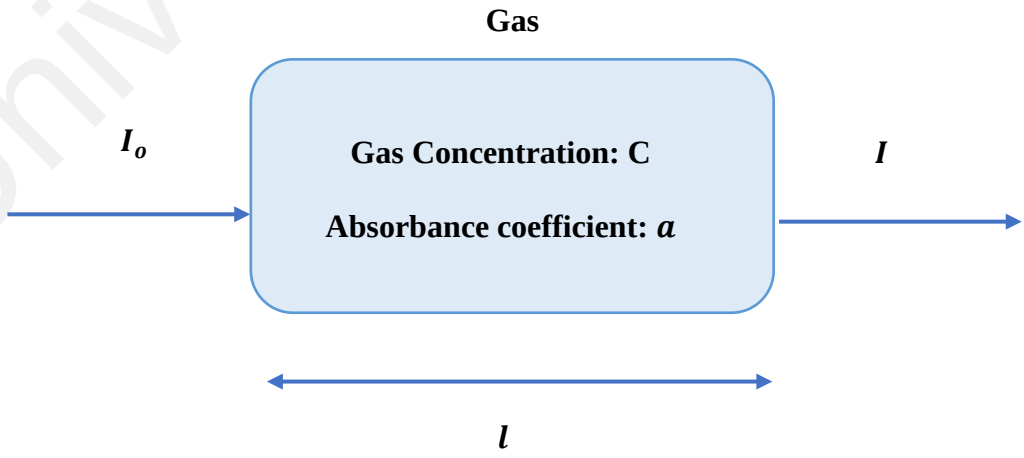

Figure 2.15: Illustration of absorption spectroscopy (Jin et al., 2013a):

The absorbance of the gas sample is defined as(Lehmann, 2016):

$$A = \log_{10} \frac{I_o}{I} = A = 0.434\ (alC) \quad \textbf{(Eq 2.5)}$$

From the Eq. 2.5 expression, absorbance is linearly proportional to a, l, and C. Change of light intensity is directly from the interaction with the gas concentration. When light is guided in the optical fiber, the interaction is now indirectly based on the evanescent fiend instead of light intensity. For the evanescent field interaction, the formula form E.q 2.4 can be rewrite as(Jin et al., 2013b):

$$I = I_o e^{(-raIC)} \quad \textbf{(Eq 2.6)}$$

Which refractive index, r is

$$r = \frac{n_r}{n_e} f \quad \textbf{(Eq 2.7)}$$

Where n_r refers to refractive index of the gas for direct sensing or sensing layer for indirect sensing. n_e however, is the effective index of the guided mode and f is the fraction of the total evanescent field power that interacts with the gas or the sensing layer. The absorbance response if the sensing layer is caused by the change of the material electronic states while interacting with the gas.

Another sensing measurement linked to absorbance is transmittance which can be written as:

$$T = \frac{I}{I_o} \quad \text{and} \quad \textbf{(Eq 2.8)}$$

$$A = -log_{10} T \quad \textbf{(Eq 2.9)}$$

Other than those two techniques, reflectance measurement can be used in spectroscopy. Reflection is defined by the change of optical signal direction at an interface between two mediums with different refractive index so the signal will revert into its original propagating medium.

2.7 Optical fiber gas sensing mechanism based on semiconductor metal oxide nanostructure

In all fiber optic sensor, a region of the exposed fiber core is responsible for fabricating a highly sensitive optical gas sensor, without a portion of the core region exposed, there would be no interaction of light and the gases. However, direct interaction of light and gases possess low and unstable result. Hence, a light and gas sensitive nanostructure SMO were used to incorporate with the fiber. The gas-matter surface reaction of the nanosized SMO play an important role affecting the response obtained from these sensors. As mentioned previously, in order to fabricate an optical fiber gas sensor, a small region of the fiber cladding is removed and replaced by the gas sensitive functionalized SMO(Samavati et al., 2019).

For nanostructure SMO as the gas sensitive material, alteration of the optical or structural properties of the nanomaterial happens when target gas molecules interact with the surface adsorbed oxygen species (originally from ambient air). These tiny alterations are responsible for the generation of signal output for the sensor. Modification of the refractive index of the nanomaterial on the optical fiber occur when gas molecules interact with the oxygen species, which resulting an alteration of its overall optical transmission and absorbance characteristic accordingly(Sangeetha & Madhan, 2020; Thangaraj et al. 2020). Evanescent wave plays an important role in the SMO gas sensing mechanism. As mentioned previously, a tiny fragment of light energy that escapes and leaves from the fiber core during a total internal reflection is called the evanescent wave. In other words, evanescent wave can be describe as a exponentially decaying electromagnetic (EM) fields in the optical fiber clad which correspond to radiative losses of the transmitting light through the optical fiber(Sharma et al., 2019). Influencing factor such as surface morphology and grain size of the nanostructure SMO surrounding the optical fiber core will affect the adsorption of the evanescent wave. Even the nature and the concentration

of the target gas will cause change to the properties of the nanostructure SMO and resulting a change of the adsorption of evanescent wave.

These changes of the properties of the nanostructure SMO may cause its refractive index to change as well. When the nanostructure SMO is exposed to target gas (reducing or oxidising gas), the refractive index of the metal oxide film will change, leading the alteration of the evanescent field absorption and the intensity of transmitted optical signal.(Huang et al., 2021; Y. nan Zhang et al., 2017). Hence, the modification of the refractive index resulting an alteration of evanescent wave absorption which eventually leads to the change of the final light output. For example, if the refractive index of the nanostructure SMO becomes greater than the core after interaction with target gas, portion of the optical light is refracted into the cladding, while another part is reflected back into the core. On the other hand, if the refractive index of the nanostructure SMO becomes lower than the core when it reacts with a target gas, then it fulfilled the total internal reflection requirement. The evanescent wave absorption at the interface will lead to the change of the final light output in the fiber core(Subramanian, Violet Dhayabaran, & Shanmugavadivel, 2020). Hence, the overall optical power changes due to the light absorbed is correspond by the nanostructure SMO coated on the tapered region.

In this chapter, the various types of gas sensor used currently and material used as the sensing element for ammonia sensing application has been explained and reviewed. An extensive review on the state of art SMO with the fabrication method as a gas sensor is presented. The optical measurement technique was also discussed including the mechanism for gas sensing. with all of the information acquired, the rationales to commence on the development of NH_3 optical fiber sensor are explained. The next chapter will discuss on the fabrication of sensing element and the set-up of the optical fiber gas sensor.

CHAPTER 3: RESEARCH DESIGN AND METHOD

This chapter consists of two main sections. First is the modification process on the optical fiber. Secondly, the process of synthesization of MoO_3 onto the tapered optical fiber. Both segments will be described in detail including preparation procedure involving fabrication of optical fiber based sensor coated with MoO_3 nanostructures.

3.1 Research Flowchart

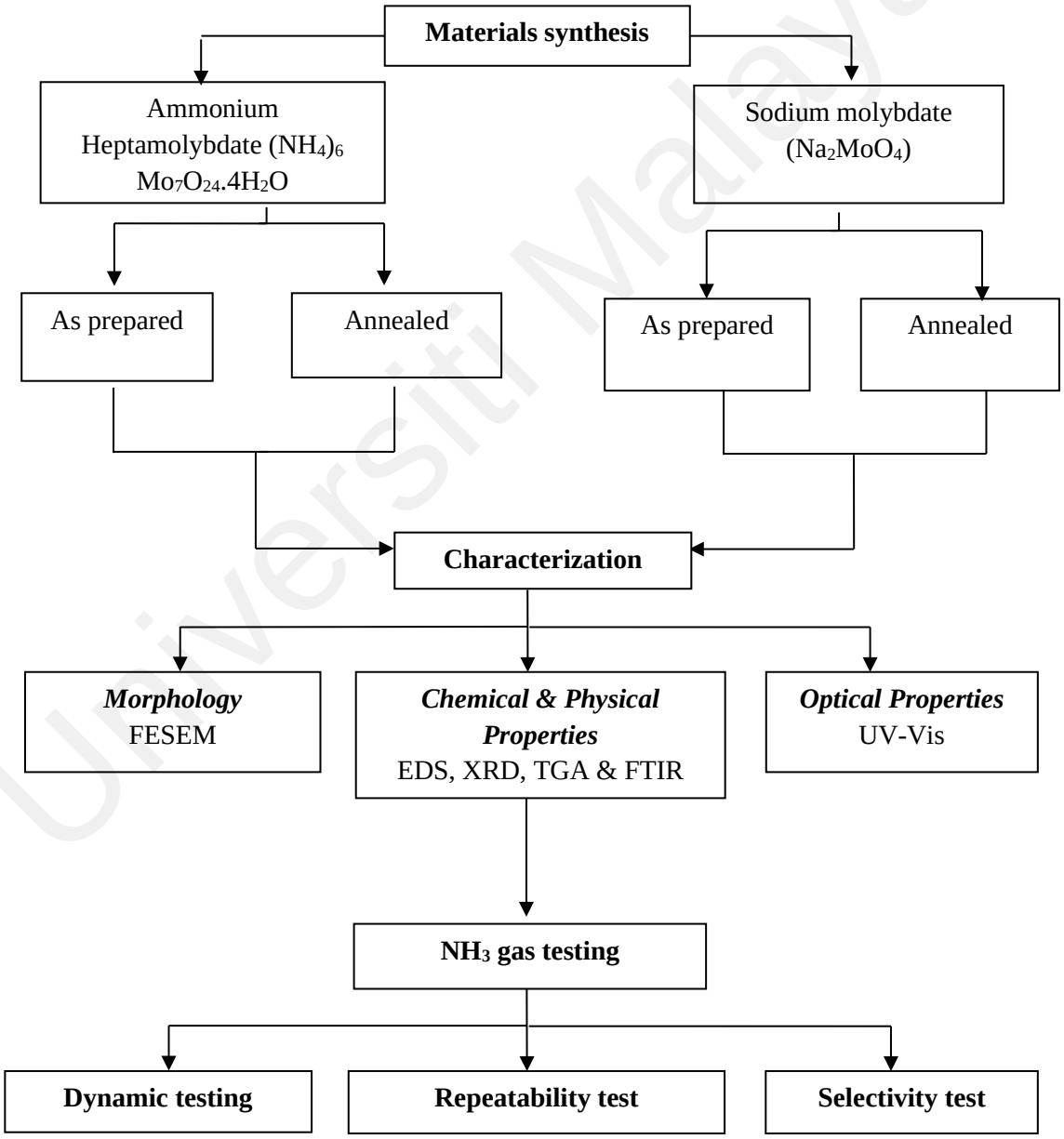

Figure 3.1: Research flowchart of the project

3.2 Fabrication and Synthesis of *h*-MoO_3 optical fiber NH_3 sensor

In the synthesis process consist of two main parts, the modification of optical fiber via tapering process and the synthesis of MoO_3 nanostructure via chemical bath deposition. The modification of the optical fiber must be done before the coating of nanostructure MoO_3 to ensure that maximum evanescence wave interaction with the material at the tapered region during gas sensing.

3.2.1 Modification of optical fiber via tapering process

In this research, multimode optical fiber (MMF) has been modified with tapering technique to remove the fiber cladding. By tapering, it was anticipated that the evanescent field produced is sufficient to activate the MoO_3 material for gas sensing. The tapered optical fiber was then coated with MoO_3 hence it exhibited optical signal respond when exposed to NH_3 with different concentration.

The optical fiber used in this research is silica (SiO_2) type multimode optical fiber (MMF) bought form OFS Furukawa Company. The diameter of fiber core is 62.5 μm and the total diameter including the cladding is 125 μm. MMF core has a larger diameter which allows strong light interaction with the sensing later coated on the tapered region.

The Vytran GPX-3400 optical glass fiber processer as shown below in Figure 3.1. and Figure 3.2. was used during the tapering process.

Figure 3.2: Vytran GPX-3400 optical glass fiber processor

Figure 3.3: Optical fiber tapering machine

The dimension of the optical fiber can be controlled when heat is applied by the graphite filament heater. Tapered profile such as waist diameter, length and up/down tapered can be set according to the dimension acquired. The parameter set for this research is a waist diameter of 20 μm, tapered length of 10 mm and a up/down tapered of 5 mm at

a desire section of the fiber. Figure 3.3 shows the FESEM image of the fiber before and after tapering process. After the tapering process was performed, the modified optical fiber was then carry on with the coating of *h*-MoO_3 using chemical bath deposition technique.

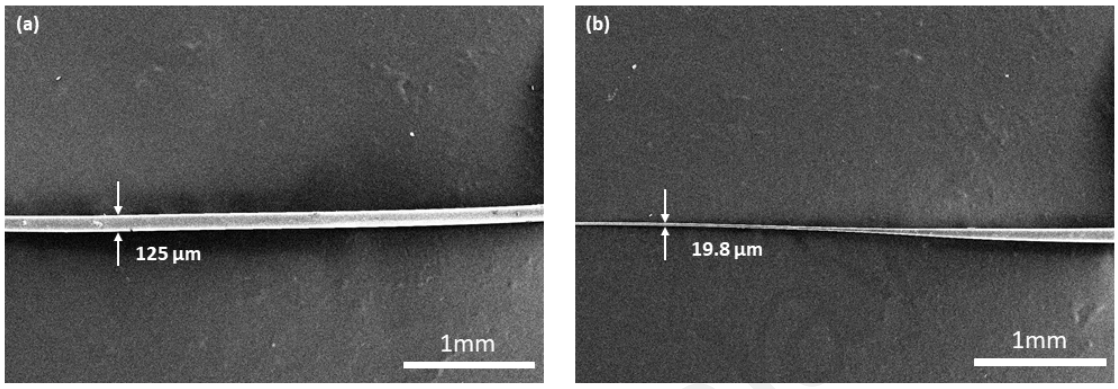

Figure 3.4: FESEM image of (a) Untapered MMF and (b) Tapered MMF

3.2.2 Synthesis and deposition of *h*-MoO_3 nanostructure via CBD

For the synthesis part of *h*-MoO_3, Ammonium heptamolybdate [$(NH_4)_6\ Mo_7O_{24}.4H_2O$] a.k.a (AHM), Sodium molybdate (Na_2MoO_4) a.k.a (SM) and Nitric acid (HNO_3) were purchase from FULLTIME ASIA SDN BHD. All of the reagents were analytical grade and used as received without further purification. Before the deposition, the tapered MMF was rinsed with distilled water and sonicated in ethanol for 20 minutes to obtained a clean surface. Next, the two stage synthesis chemical bath deposition applied is based on Arpan Dhara el al(Dhara et al., 2014) with modification. For the two-stage deposition, 15 ml of 0.65M HNO_3 was combined with 30 ml 0.01M, 0.025M and 0.5M of Ammonium heptamolybdate $(NH_4)_6\ Mo_7O_{24}.4H_2O$ solution with continuous stirring. The mixture solution was then placed into a water bath at a constant temperature of 85^{o}C. Later, the cleaned and dried MMF were placed into the solution for 20 minutes. This first stage

deposition is considered as nucleation step. According to Chithambararaj (Chithambararaj & Chandra Bose, 2014), the chemical reaction was introduced by the ions of precursor which is ammonium heptamolybdate (AHM) and nitric acid (HNO_3) in the water solvent medium. The reaction mechanism can be written as in the equation 3.1.

$$[NH_4]_6Mo_7O_{24} \cdot 4H_2O\ (aq) + 6HNO_3 \rightarrow$$

$$[H_4N]_x \cdot 7MoO_{3-y}[OH]_z + 6NH_4NO_3(aq) + 7H_2O\ (l) \quad \text{..... (Eq 3.1)}$$

After that, fiber were removed from the solution and rinsed thoroughly with distilled water. Later on, the fiber were again put into the same solution for another 10 mins as this 2nd stage deposition is consider as the growth step. After the 2nd deposition, the fibres were washed and dried in the oven with 85°C for 30 mins to remove the water molecules on the surface. The coated fiber is then annealed in temperature of 150°C. These steps were repeated for the deposition using 0.1M of Sodium molybdate (Na_2MoO_4) precursor when preparing the sodium-based *h*-MoO_3. The reaction mechanism for Sodium Molybdate and nitric acid can be written as in the equation 3.2.

$$Na_2MoO_4(aq) + 2HNO_3 \rightarrow MoO_3 + 2NaNO_3(aq) + H_2O\ (l) \text{.....(Eq 3.2)}$$

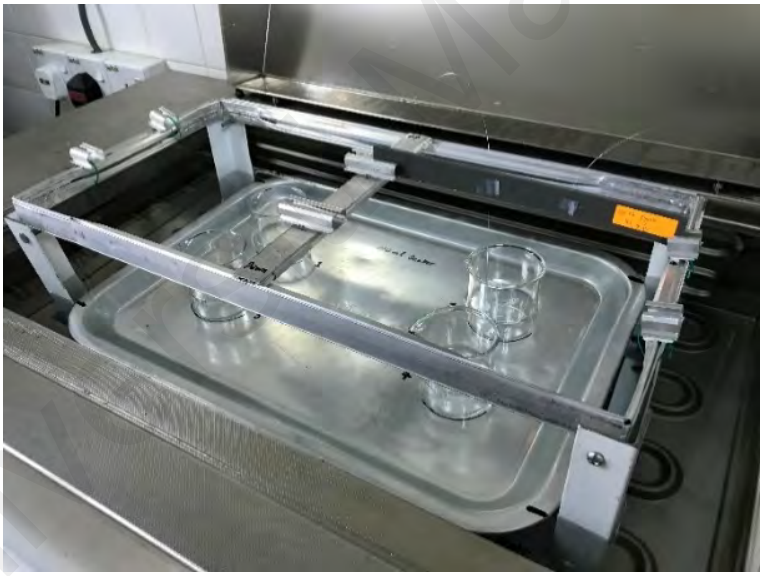

3.3 Material characterization

There are several techniques of characterization used throughout this research work which include field emission scanning electron microscope (FESEM), energy dispersive spectroscopy (EDS), Selected area electron diffraction (SAED), X-ray photoelectron spectroscopy (XPS), X-ray diffraction (XRD), Fourier-transform infrared spectroscopy (FTIR), thermogravimetric analysis (TGA) and UV-visible spectroscopy (UV-Vis). All these characterizations are aimed to obtained the sample morphology, chemical composition, crystal structure, thermal properties and also the optical properties of the material. This will then use to compare with the sensing performance of the synthesised nanomaterial.

3.3.1 FESEM

FESEM provides visual image of very tiny topographic details using the bombardment of electrons. The FESEM is capable for viewing morphology down to 1 nm scale of the nanomaterial. The magnification of imaging can be adjusted based on the requirements of the observation.

The FESEM is a type microscope that uses electrons with a negative charge instead of the traditional spectroscope which uses light to display the sample image. The source of electrons in FESEM is a field emission gun that produces very high concentrated and low-energy electron beams. The electrons then accelerate at a high velocity in a high electrical field gradient. The source electrons are concentrated and deflected by objective lenses in the column chamber, which is high in vacuum, to generate a narrow scan beam that targets the sample. This bombardment of high-speed electron causes the secondary electrons to release from the sample. The angle and velocity of these emitted secondary electrons are strongly influenced by the sample's surface characteristics. A detector that receives and generates an electrical signal from the secondary electrons generated. As a result, this

signal is amplified and shown on a monitor as a digital picture (Abd Mutalib, Rahman, Othman, Ismail, & Jaafar, 2017).

Figure 3.7: FESEM Hitachi SU8030 at MIMOS Sdn. Bhd

Figure 3.8: FE-SEM Hitachi SU5000 at HI-TECH INSTRUMENTS

The sample need to be conductive enough to obtained a high-resolution image. If the sample is not conductive enough, electric charging occurs which will cause a low quality and a blurry image. Hence, a thin (1.5 – 3.0 nm) of conductive material such as gold (Au), platinum (Pt) is needed. In this research, the morphologies were inspected using FESEM Hitachi SU5000 at HI-TECH INSTRUEMNTS and FESEM Hitachi SU8030 at MIMOS Sdn. Bhd as shown in Figure 3.6 and Figure 3.7. It was set at an operating voltage of 2–3 kV during sample testing.

3.3.2 EDS

EDS is a chemical analysis technique that is used in conjunction with scanning electron microscopy to analyse the surface of a sample (SEM). The electron bombardment will produce a specific sort of X-rays, which will be collected by the EDS and used to identify the chemical composition of the sample.

After being bombarded by the electron beam from the source, electrons are expelled from the atoms on the sample's surface. This resulted in the development of electron vacancies, which will be filled by higher-energy electrons. To balance the energy disparities, an X-ray is emitted as an electron shifts from one state to another. Thus, this released X-ray energy provides information regarding element from which it was emitted. And by detecting this emitted X-ray will help to identify the chemical composition of the material, as each incident X-ray will transfer to a computer for data evaluation. The EDS output are presented in the from of intensity peak versus beam energy spectrum(Mishra, Zachariah, & Thomas, 2017).

The EDS (Energy Dispersive X-ray, EDAX Octane Elect EDS System) connected to the FESEM at HI-TECH INSTRUEMNTS was employed in measuring the samples' elemental composition in this work.

3.3.3 XPS

X-ray photoelectron spectroscopy (XPS), also known as electron spectroscopy for chemical analysis (ESCA), is a technique for analyzing a material's surface chemistry. XPS can measure elemental composition as well as the chemical and electronic state of the atoms within a material. XPS spectra are obtained by irradiating a solid surface with a beam of X-rays and measuring the kinetic energy of electrons that are emitted from the top 1-10 nm of the material. A photoelectron spectrum is recorded by counting ejected electrons over a range of kinetic energies. The energies and intensities of the photoelectron peaks enable identification and quantification of all surface elements (except hydrogen).

In this work, the element compositions and chemical states of the *h*-MoO_3 synthesised from SM precursor were obtained by X-ray photoelectron spectroscopy (XPS) conducted with a ULVAC-PHI Quantera II electron spectrometer using Al Kα monochromatic X-Ray Source.

3.3.4 SAED

Selected area electron diffraction (abbreviated as SAD or SAED), is a crystallographic experimental technique that can be performed inside a transmission electron microscope (TEM). In this work, only the annealed *h*-MoO_3 sample synthesised from SM precursor was investigated using high resolution transmission electron microscopy (HR-TEM) (Hitachi HT7800) with accelerating voltage of 100 kV to obtain the SAED diffraction.

3.3.5 XRD

XRD is a technique for determining a material's crystallographic structure. The identified sample could be prepared as a thin film or as a solid object. XRD works by bombarding a material with incoming X-rays and then measuring the intensities and scattering angles of the X-rays that escape.

An X-ray source, a sample container for powder or thin film sample, and an X-ray detector are the three basic components of an XRD. The cathode ray tube produces X-rays, which are then filtered to create monochromatic radiation and aimed towards the sample on the holder. The intensity of the reflected X-rays is recorded when the sample and detector are rotated. A constructive interference occurs when the angle of the incident X-rays irradiating the sample fulfils the Bragg Equation, resulting in the development of a substantial peak of greater intensity. This X-ray radiation is detected by a detector, which converts it to a count rate, which is then shown on a computer monitor. Data is gathered at 2 angles ranging from 5° to 70° for typical powder patterns, angles that are present in the X-ray scan. Each of the sample have its own unique pattern of diffraction dues to its different arrangement of atom(Epp, 2016). This can be identified and matched using software such as HighScorePlus which containing thousands of references to match and cross check. The other most reliable and recognized scientific organization that provides a reference database is the international Centre of Diffraction Data (ICDD).

In this work, the XRD used for examination of the phase and crystal structure was performed with a Bruker D8 Advance and a CuKα (λ = 1.5406 Å).The XRD was conducted in the range of $2\theta = 5^{\circ}–80^{\circ}$ and a step size of 0.02°. It is located at NANOCAT, Institute of Advance Studies in University of Malaya which is illustrated in Figure 3.8.

Figure 3.9: Bruker D8 Advance located at NANOCAT, Institute of Advance Studies, UM

3.3.6 FTIR

FTIR is a simple and fast analytical method for identifying functional groups in a sample's chemical properties. Infrared light is used in the FTIR study to determine chemical composition. First, the light source shines 10,000 to 100 cm^{-1} infrared radiation through a sample, with part of it absorbed by the sample and some passing through. In order to release the absorbed energy, functional group of the sample will undergo movement such as spinning motion and/or vibrating motion. As a result, the received signal will be shown as a spectrum, generally ranging from 4000 cm^{-1} to 400 cm^{-1}, revealing the sample's chemical fingerprint peaks. At a particular wavenumber, each functional group vibration or rotational movement will create a distinct spectral fingerprint(X.-T. Li et al., 2011).

Attenuated Total Reflectance (ATR) technique uses the reflectance technique to determine a sample's functional group. To transmit the incoming energy, ATR employs a phenomenon known as total internal reflectance. The incident light is directed at a crystal at an angle that allows it to reflect at the bottom and top of the crystal before leaving the crystal on the opposite side. The sample is then placed on the crystals to allow it to come into contact with the incident light, allowing for energy transfer at the crystal and sample interface. The author utilised a Monolithic diamond ATR with a wide spectral range from 4000 to 400 cm^{-1} and into the far IR at the University of Malaya's (UM) Chemistry department for this study which shows in Figure 3.9.

Figure 3.10: Monolithic diamond ATR located at the Chemistry department, UM

3.3.7 TGA

TGA is a crucial characterization for determining a sample material's thermal behaviour and characteristics. TGA measures the mass change of the sample as a function of changes in the surrounding temperature. During the process of sample heating, the sample will undergo weight changes and might encounter total decomposition when reaches a higher temperature. By knowing the weight change of the sample, we are able to determine the synthesis parameter for our metal oxide annealing temperature.

Inside the components of a TGA, it consists of a sample holder which is connected by a highly precise balance to measure the weight change of the sample in a microscopic level. The process of heating occurs in the part of the furnace. The environment inside the furnace is fully controlled by constantly purging an inert gas or a normal synthetic air and escape through the exhaust of the furnace. By using the analyser, the important quantified information such as loss of water, loss of solvent, decarboxylation, pyrolysis, oxidation and decomposition can be obtained. The TGA instrument used in this research work was Mettler Toledo TGA/SDTA851 located at the Faculty of Mechanical Engineering, UM as shown in the Figure 3.10 and 3.11. The experiment was carried out in a dynamic nitrogen atmosphere with a 10°C/min heating rate.

Figure 3.11: Mettler Toledo TGA/SDTA851 at Faculty of Mechanical Engineering, UM

Figure 3.12: Mettler Toledo TGA/SDTA851 at Faculty of Mechanical Engineering, UM

3.3.8 UV-Vis

UV-Vis spectroscopy is by far a relatively fast, simple and inexpensive method to determine the concentration of an analyte and also the optical absorbance, transmittance and also reflectance of a sample. this characterization uses a UV or Visible light source wavelength to be passed through a sample. The magnitude of the absorbance or reflectance light wave can be determined by comparing to the reference set. Hence with all these information, an optical band gap of the sample material can be estimated.

However, in this research, the sample for this particular characterization is in the form of thin film. Hence the Cary 7000 Universal Measurement Spectrophotometer (UMS) from MIMOS Sdn. Bhd. as displayed in Figure 3.12. Was used in this research as it can perform the characterization on solid sampling. It uses the light source of Tungsten halogen visible and deuterium arc UV and a light wavelength of 200nm to 1000nm was used.

Figure 3.13: Cary 7000 Universal Measurement Spectrophotometer (UMS) from MIMOS Sdn. Bhd.

After characterised using the UV-Vis, the obtained optical spectrum were used to do estimation of optical band gap of material by applying Tauc plot principle in which the optical absorbance strength depends on the difference between the photon energy. The relationship is represented in the equation 3.3 as follows:

$$(ahv)^2 = A(hv - E_g) \quad \textbf{(Eq 3.3)}$$

Where h is the plank constant, v is the photon's frequency, a is the absorption coefficient, E_g is the bandgap and A is the proportionality constant. By plotting the $(ahv)^2$ vs hv, an estimation of the band gap can be obtained by Tauc plot. The liner extrapolation of the plotted curve is the estimation value of the band gap.

3.4 Gas Sensing Measurement Setup

3.4.1 Absorbance Measurement Setup

In the gas sensor setup as shown in Figure 3.13, tungsten halogen (HL-2000 Ocean Optics USA) that provide output from 360 nm to 2500 nm was used as the light source. The absorbance was determined using spectrometer (USB4000 VISNIR, Ocean Optics USA) from the gas chamber. Standard SMA optical fiber was used to link the whole assembly for light propagation. The standard connection MMF to SMA terminated cable is 1.4 dB with an estimated coupling effectiveness of 99.6%, according to the adapter specification sheet. The SMA fibre was immediately spliced with the h-MoO_3 coated tapered optical fibre sensor, which was then placed in the sealed customised gas chamber. The NH_3 gas was diluted using pure synthetic air by the mass flow controller (MFC) to the required concentration of 100 ppm - 5000 ppm. To examine the sensor's dynamic response, the NH_3 gas and pure synthetic air were purged for 8 minutes and 10 minutes, respectively, to allow the sensing material to react and recover.

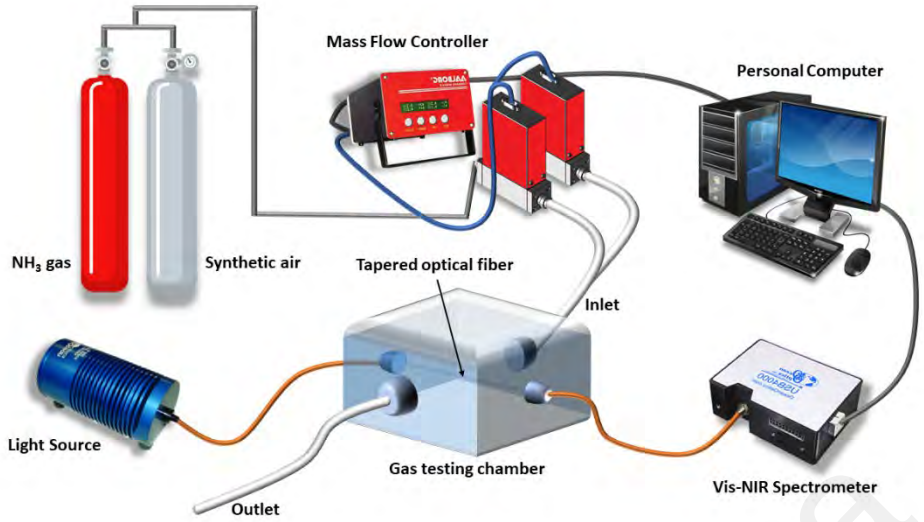

Figure 3.14: Gas sensing set up for RT NH_3 gas sensing

The spectrometer was connected to a Spectrasuite software in the personal computer to monitor the absorbance measurement. The software calculates the absorbance (A_λ) by the equation 3.4:

$$A_\lambda = -log_{10}\left(\frac{S_\lambda - D_\lambda}{R_\lambda - D_\lambda}\right) \quad \textbf{(Eq 3.4)}$$

Where:

S_λ = is the light intensity detected at wavelength, λ during the presence of target analyte

D_λ = is defined as a stored 'dark' intensity during the absence of light passing through the optical fiber which refer to background ambient lights.

R_λ = is the stored 'reference' intensity when the carrier gas of synthetic air is presence

All the measurement was normalized with respect to the sample substrate. Thus, the absorbance spectra measured are responsible by the sensing material.

The gas calibration system (Aalborg, Command Module) is linked to a Labview application on the computer, which controls gas purging into the chamber through a mass flow controller (Aalborg, MFC), which also keeps the air flow at 200 sccm. To adjust the concentration of NH_3 in the chamber, the 1 percent NH_3 gas was diluted with high purity dry synthetic air. Both NH_3 and synthetic air gas cylinders are certified from Linde, Malaysia-Singapore Sdn Bhd, that was used in the mixing and purging of the gases into the chamber.

3.4.2 Gas chamber construction for optical fiber sensor

The self-modified gas chamber used for NH_3 sensing is shown in the Figure 3.14 below. The chamber consists of two main ports for gas inlet and gas outlet, a main heating plate located at the centre of the chamber which connected with two electrical points attached with the volt supply and an input for the thermocouple. The Teflon at both sides was drilled with a micro hole for the insertion of optical fiber. The optical fiber was spliced with a pigtail connected to FC-SMA cable that was linked to the light source and the spectrometer.

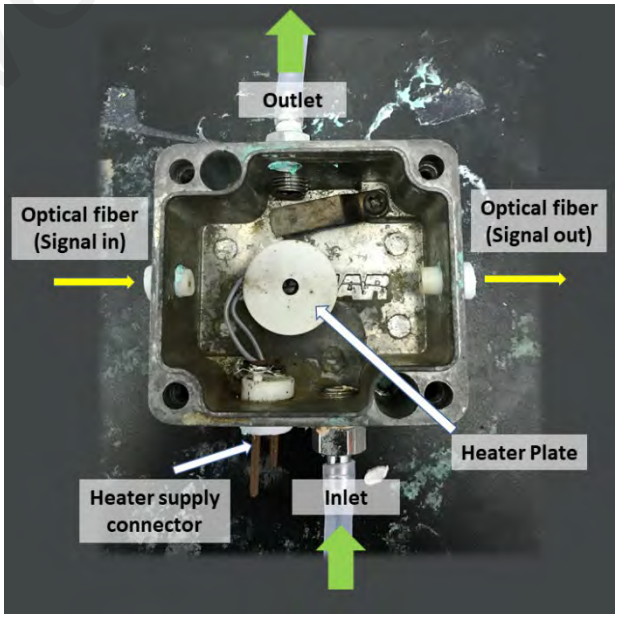

Figure 3.15: Gas chamber for optical fiber

Figure 3.15 shows the light that travels into the tapered region of the optical fiber. From the image, the leakage light is responsible with the interaction of the sensing layer which will changes its properties when exposed and react with NH_3 gas.

Figure 3.16: Light propagates into the tapered optical fiber sensor.

3.4.3 Gas testing system and procedure

The performance of the optical fiber sensor toward NH_3 was measured in this work. The sensor was initially exposed to 30 minutes of synthetic air in order to allow the optical fiber to archive its steady state. The sensor was than exposed to 8 minutes to the target gas, NH_3 to observe the duration require to reach its steady state. Then, pure synthetic air was purged in to the chamber for 10 minutes to allow the sensor undergoes its recovery process until it reaches it baseline. A standard procedure was deployed in this work, where three cycles were tested with different concentration of NH_3 alternately with pure synthetic air to obtained a much more average result.

3.5 Optical sensing parameter

Optical sensing parameters under studies for developed optical fiber sensor are response and recovery time, sensitivity, repeatability and selectivity.

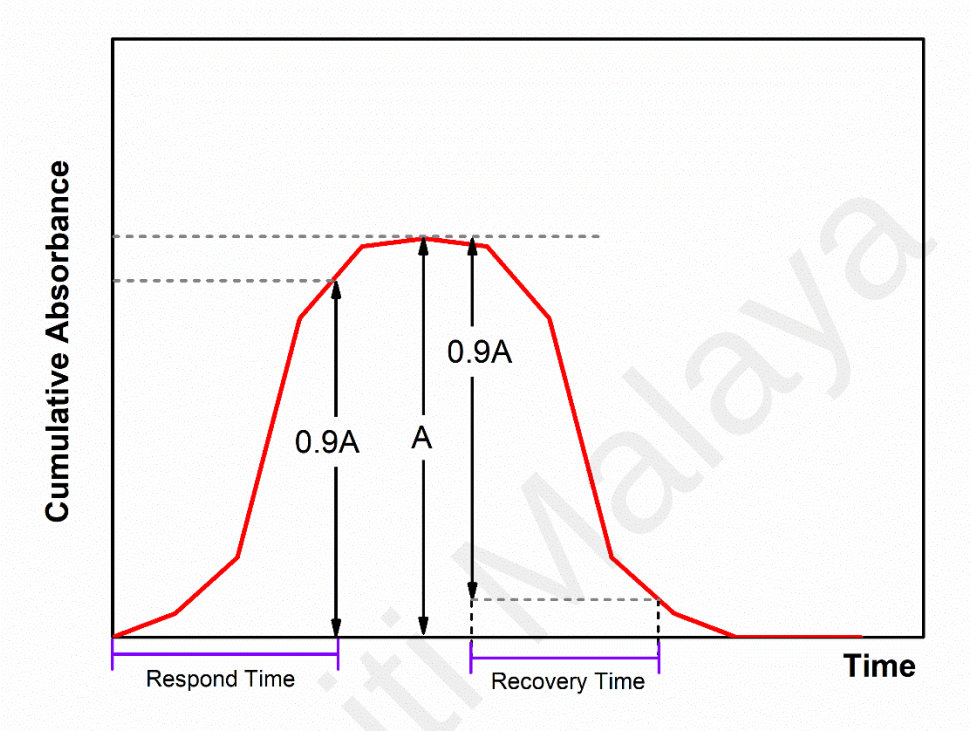

Figure 3.17: Illustration of response and recovery time

Respond time is defined as the time acquire by the sensor to achieve at a stable value for example the time at which the output is 90% if its final value. Meanwhile recovery time is defined in a similar was but conversely.

Sensitivity is defined as a change of measure signal per analyte concentration unit, for example the slope of the calibration curve. In absorbance measurement, the sensitivity can be expressed as shown in equation 3.5:

$$S = \frac{A_S - A_O}{C} \quad \textbf{(Eq 3.5)}$$

Whereas, A_s is the absorbance response with the present of analyte, A_o is the absorbance response in synthetic air and C is the concentration of the analyte in (%).

Repeatability is the sensor's ability to produce the same response for successive measurements of the same input, when all operating and environment condition remain constant. The developed sensor in this work were tested for three cycles to determine its repeatability.

Selectivity refers to the characteristics that determine whether a sensor can respond selectively to a group of analyses or even specifically to a single analyte. In this work, the samples were exposed to other gases such as hydrogen (H_2) and methane (CH_4).

CHAPTER 4: RESULTS AND DISCUSSION

4.1 *h*-MoO_3 using Ammonium Heptamolybdate (AHM) as precursor

In this part, the development of *h*-MoO_3 using two different precursors Ammonium Heptamolybdate $(NH_4)_6$ $Mo_7O_{24}.4H_2O$), also known as (AHM) and also Sodium molybdate (Na_2MoO_4), also known as (SM) was discussed in term of its characterization and its NH_3 gas sensing performance.

Characterization measurement for the *h*-MoO_3 was performed to check on the physical and chemical properties of the material. The morphology of the sensing layer was examined by Field Emission Scanning Electron Microscopy (FESEM). To confirm on the material element, Energy Dispersive Spectroscopy (EDS) was use as well. The crystal phase transition and its crystallinity were determined via the X-Ray Diffraction (XRD) method and the Selected area electron diffraction (SAED). X-ray photoelectron spectroscopy (XPS) and Fourier-transform infrared spectroscopy (FTIR) which provide information on the chemical bond existed in the material. Further investigation on the thermal and optical properties of the material was done using Thermogravimetric analysis (TGA) and Uv-Vis measurement.

The sensing performance of the developed sensor were analysed in absorbance response exhibits during the NH_3 exposure. The dynamic respond was also measured so that the respond and recovery time can be determined. The sensitivity of the sensor was calculated and the selectivity test of the sensor towards other gases was also carried out.

4.1.1 Characterization of *h*-MoO_3 using Ammonium Heptamolybdate (AHM) on tapered optical fiber

4.1.1.1 FESEM

Physical properties such as surface morphology of the coated sensing later is important in determining the sensing performance of the developed sensor. As a larger total surface of the nanostructure formed is highly beneficial towards gas sensing. The surface morphology of the *h*-MoO_3 coated on the tapered optical fiber was observed via FESEM as shown in Figure 4.1. The figure shows the deposition on the *h*-MoO_3 on the tapered region is still consider quite well distributed on the surface with some uncoated spot. 2 types of samples have been prepared for this research which is the as prepared sample Figure 4.1 (b) and the 150^{o}C annealed sample Figure 4.1 (c).

Generally, the *h*-MoO_3 nanostructure shows a formation of nanograin like structure of 40 nm- 70 nm size for as prepared sample and a slightly larger 60 nm- 90 nm of nanograin for annealed sample. In the other hand, the annealed sample observed to be more denser comparing to the as prepared sample. This is largely caused by the annealing effect. The formation of the *h*-MoO_3 nanograins begins with nucleation, aggregation and coalescence of particles to form the nanostructure, accordingly(Chithambararaj et al., 2016; de Castro et al., 2017).

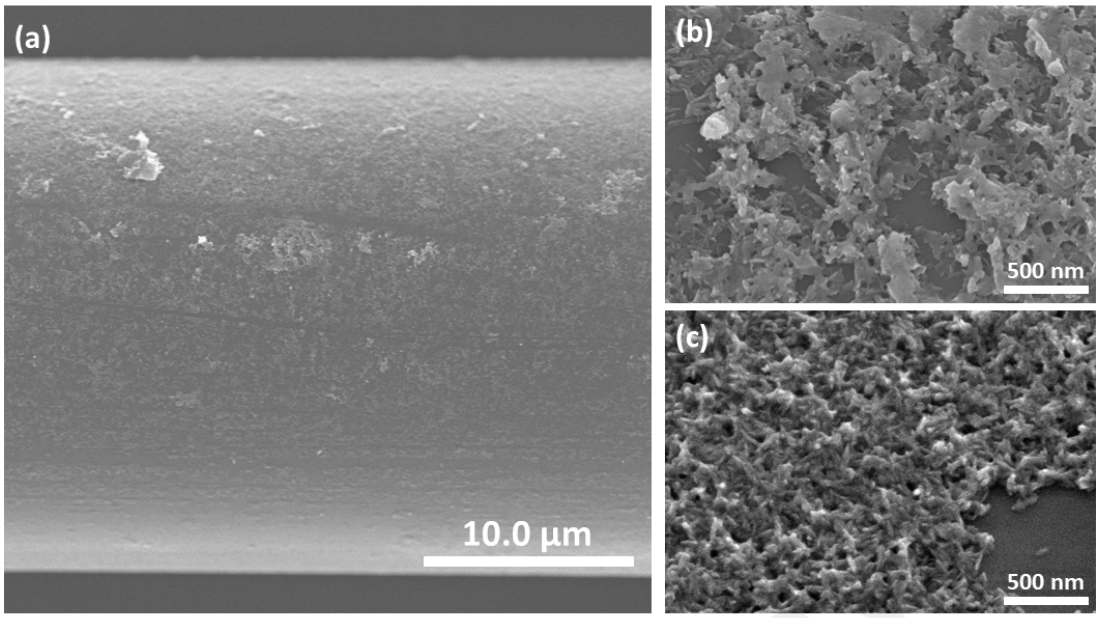

Figure 4.1: FESEM image of (a) tapered MMF coated with *h*-MoO_3 nanograins, (b) as prepared sample and (c) 150°C annealed sample

4.1.1.2 EDS

EDS was performed to verify the element that exists in the synthesized *h*-MoO_3. The EDS pattern displayed in Figure 4.2. shows the oxygen (O) with the highest peak which follow by the silicon (Si) which is due the material of the tapered optical fiber and lastly the Molybdenum (Mo). A carbon (C) peak has been detected in the EDS around 0.2-0.3 keV, this is due to the carbon introduce from the environment. Hence, it's not included in the calculation. EDS mapping in figure 4.3 shows that *h*-MoO_3 has been coated on the optical fiber.

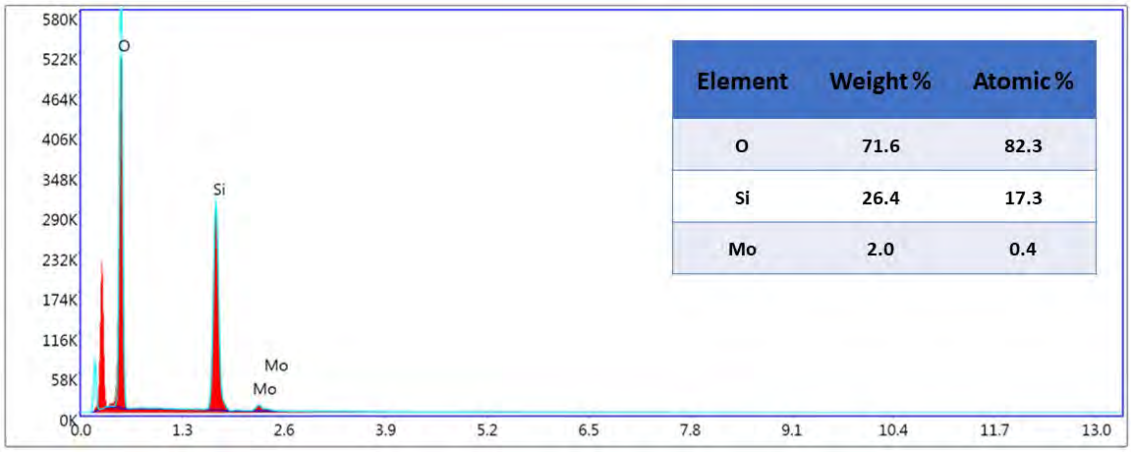

Element	Weight %	Atomic %
O	71.6	82.3
Si	26.4	17.3
Mo	2.0	0.4

Figure 4.2: EDS measurement of *h*-MoO_3 nanostructure

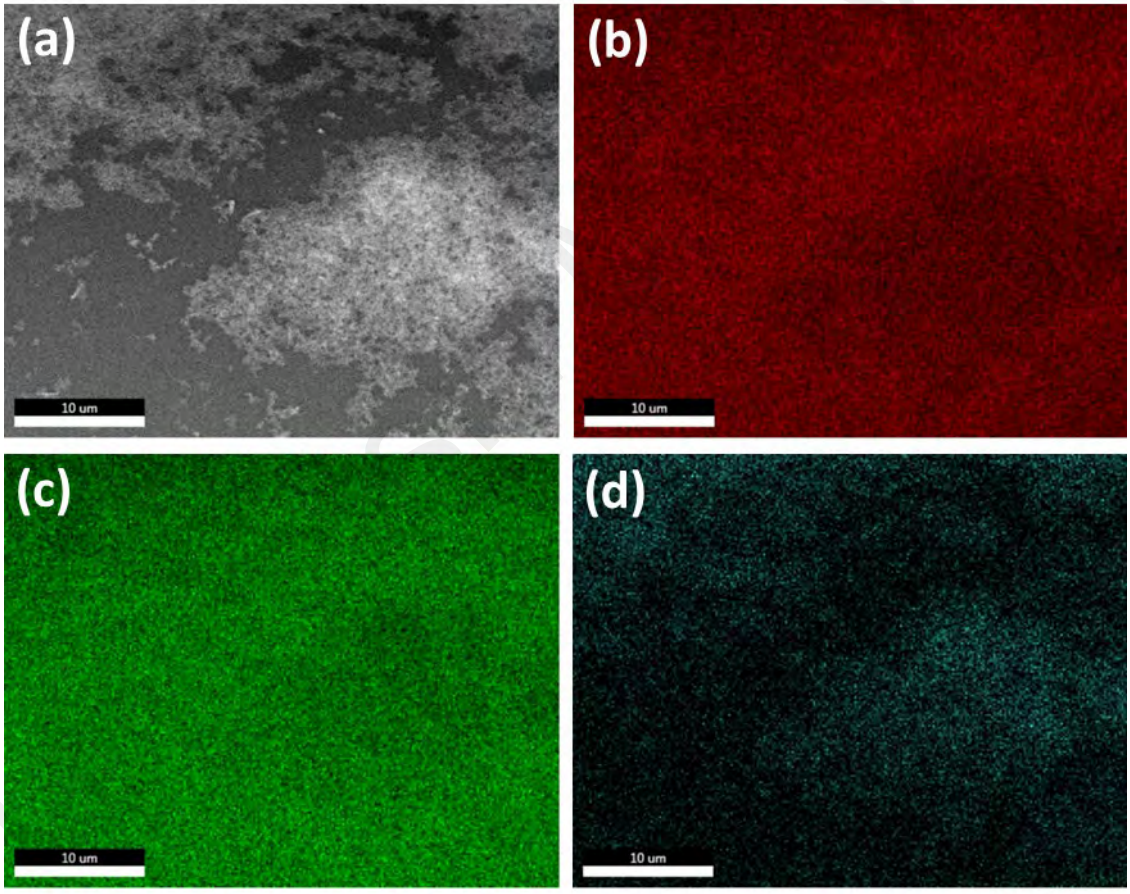

Figure 4.3: (a) FESEM image of *h*-MoO_3; (b)-(d) EDS mapping of the distribution of each element; (b) Oxygen, (c) Silica and (d) Molybdenum

4.1.1.3 XRD

XRD analysis of the synthesised *h*-MoO_3 powder in Figure 4.4 shows a very significant peak at $2\theta = 9.8^o$, 19.8^o, 26.3^o and 29.5^o are indexed at (100), (200), (210) and (300) crystal planes of *h*-MoO_3 phase, respectively with the reference to the JCPDS data card no. 00-021-0569. The lattice constant for the sample obtained are a=b=10.5310 Å and c=14.8760 Å which also matches with the reference card. The XRD peak of the annealed sample and the as prepared are put together and compared. It was observed that no phase transition occurs in this temperature range which all the peak exhibits in the same angle. However, the annealed sample show better crystallinity which proved from its higher intensity and sharper in peak. It has been proved that heat treatment via annealing will improve its crystallinity and increase the active sites for gas sensing, hence enhancing the gas sensing performance(Bolokang & Motaung, 2019; S. Yang et al., 2015; C. Zhang et al., 2020).

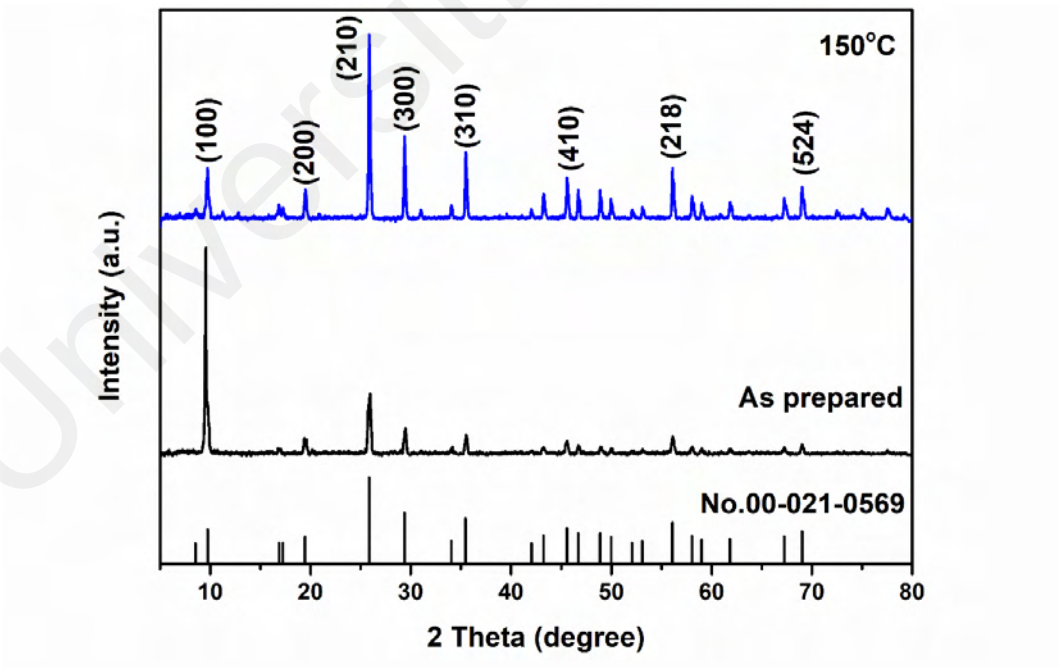

Figure 4.4: XRD pattern for both samples as-prepared and annealed *h*-MoO_3

4.1.1.4 FTIR

The element composition of the prepared and annealed *h*-MoO_3 is proved by the FTIR analysis. The FTIR spectra of the as prepared sample and the annealed sample are shown in Figure 4.5. Both the sample shows the characteristic vibrational peak of *h*-MoO_3. The peaks observed between 1000 cm^{-1} and 400 cm^{-1} are responsible to the Mo-O functional group. The most significant peak observed at 862 cm^{-1} and 964 cm^{-1} are assigned to the stretching vibration of Mo=O. Furthermore, the peaks at around 685 cm^{-1} are attribute to the Mo-O stretching bond. The stretching and bending vibration of water molecules bonds are shown by the peaks located at 3438 cm^{-1} and 1610 cm^{-1}. And lastly, the peaks located at 3197 cm^{-1} and 1410 cm^{-1} are assigned to the stretching and bending vibration of N-H related group(Chithambararaj et al., 2016). So, it can be seen that the peaks related to the water molecules and also the N-H related group reduce with the increase of annealing temperature. This is due to the desorption of water molecules and elimination of the surface adsorbed nitrates and ammonium ions.

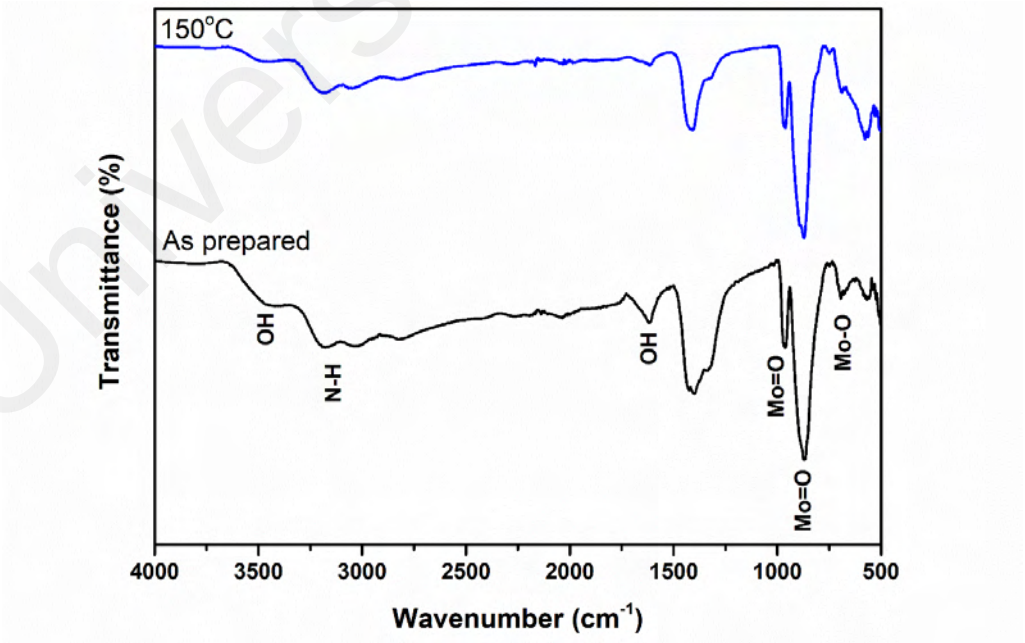

Figure 4.5: FTIR spectra of as prepared and annealed *h*-MoO_3

4.1.1.5 TGA

TGA allow the understanding of the sample's thermal stability which helps in determining the annealing temperature in the process of nanostructure modification. Based on Figure 4.6 shown below, there are 4 main mass losses of *h*-MoO_3 along the increment of temperature: the first mass loss is due to the desorption of water molecules that are physically adsorbed on the surface of the *h*-MoO_3 particles which happens in the temperature between 100^{o}C and 170^{o}C. Follow by the elimination of the surface adsorbed nitrates and ammonium ions between 200^{o}C and 250^{o}C. The last 2 mass losses which happens very close to each other recorded at 390^{o}C and 410^{o}C are accounted for the decomposition of the internal structure of *h*-MoO_3. Hence, this will result an unstable phase propagation form *h*-MoO_3 to α-MoO_3(Chithambararaj et al., 2016). By comparison the α-MoO_3 are more thermodynamically stable which are able to withstand until around 800^{o}C before falling into complete decomposition. The temperature range tested from room temperature to 1000^{o}C, the synthesis MoO_3 are consider thermodynamically stable and in high purity because of the minimal and insignificant weight loss occurred.

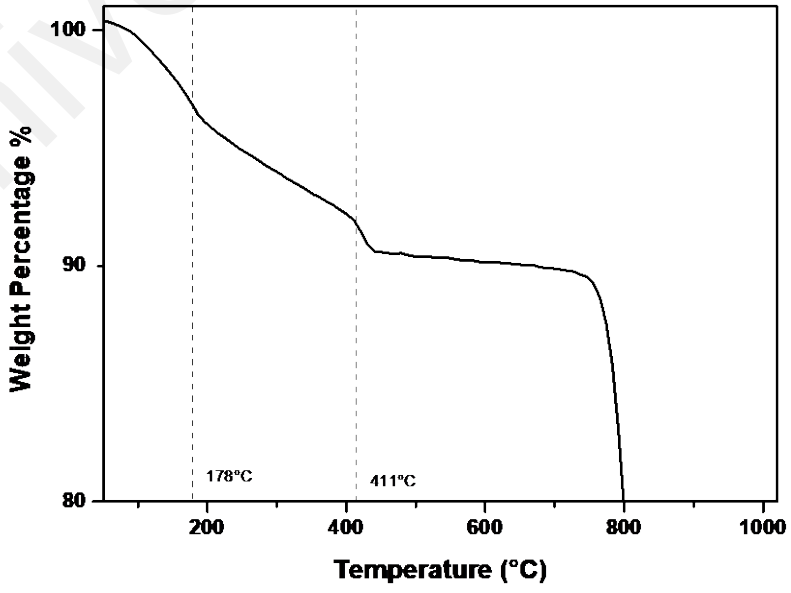

Figure 4.6: TGA curve of the synthesized MoO_3 powder

4.1.1.6 Uv-Vis

The optical band gap of synthesized and annealed *h*-MoO_3 can be estimate with the plot $(ahv)^2$ versus hv. The value of the optical band gap (E_g) can be measured by taking the tangent to the curve across the hv axis as demonstrated in Figure 4.7. From the graph, the estimated band gap is 3.98eV for as prepared *h*-MoO_3 and 4.03eV for annealed *h*-MoO_3. The result shows the slight increase of band gap when the increase of annealed temperature to 150^{o}C(Ali & Farrukh, 2018). The increases of optical band gap after annealing process is highly influenced by the gap states that are generated by the oxygen vacancies (Yao et al., 2019)and the change in charge carriers which can be explained by the Burstein Moss (BM) effect(Khelchand Singh & Rajkumari, 2019).

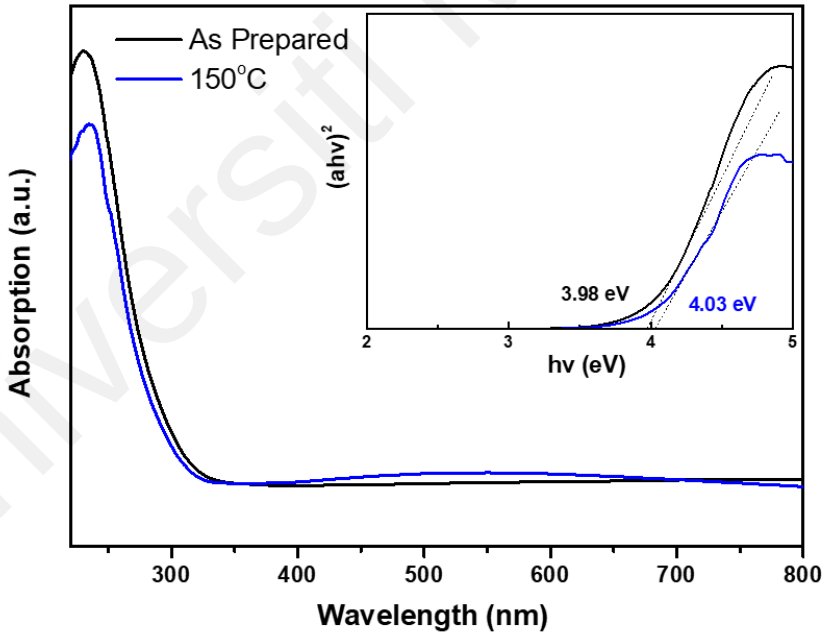

Figure 4.7: Estimated optical band gap of as prepared and annealed *h*-MoO_3.

4.1.2 Absorbance measurement of *h*-MoO_3 using Ammonium Heptamolybdate (AHM) on tapered optical fiber towards NH_3 gas sensing

4.1.2.1 Untapered and tapered blank optical fiber sensing properties

Before proceeding to the NH_3 gas testing, preliminary work as reference needed to be done first. This including testing the untapered and also the tapered but blank optical fiber towards the NH_3 gas to confirm whether any responses arise from the experiment. This is important to verify before coating any material on it.

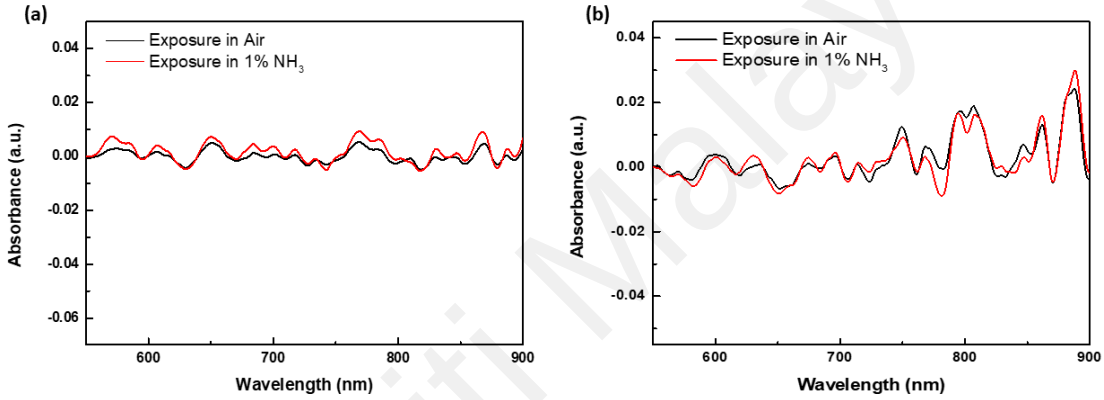

Figure 4.8: Absorbance respond versus wavelength of uncoated (a) untapered, (b) tapered MMF when exposed to 10 000 ppm of NH_3 at room temperature

The uncoated tapered and untampered optical fiber were exposed to 10 000ppm NH_3 at room temperature as shown in Figure 4.8, it is observed that no significant change of absorbance magnitude for both the sample even when 10 000ppm of NH_3 was purged in to the gas testing chamber. It can be concluded that both the untapered and tapered optical fiber shows no absorbance when there is no material coated on the fiber. Hence, by coating light reactive functionalized material, we are expecting to enhance the sensitivity on its absorbance change towards NH_3 environment.

4.1.2.2 Tapered optical fiber coated with *h*-MoO_3 using Ammonium Heptamolybdate (AHM) as precursor

This section will discuss on the optical responses obtained when sensors exposed to different concentration of NH_3 gas. The sensing performance investigated were based in the response and recovery time, sensitivity and also repeatability and its selectivity. The sensor developed from *h*-MoO_3 nanostructure coated on tapered optical fiber were investigated in terms of its precursor concentration, deposition time during the CBD and also the annealing effect.

4.1.2.2.1 Sensing performance of *h*-MoO_3 using different concentration of Ammonium Heptamolybdate (AHM) precursor

In this section, the concentration of the AHM precursor used to coat on the tapered optical fiber ranges from 0.01M, 0.025M and 0.05M. All the other parameter of the experiment such as temperature and deposition time is fixed to ensure that the sample have similar coating time. The NH_3 gas sensing was conducted in room temperature. Figure 4.9 shows the dynamic respond of different concentration of precursor used for the chemical bath deposition process. Optimizing the most suitable concentration of the precursor used will help to ensure a steady nucleation process for better coating and better morphology.

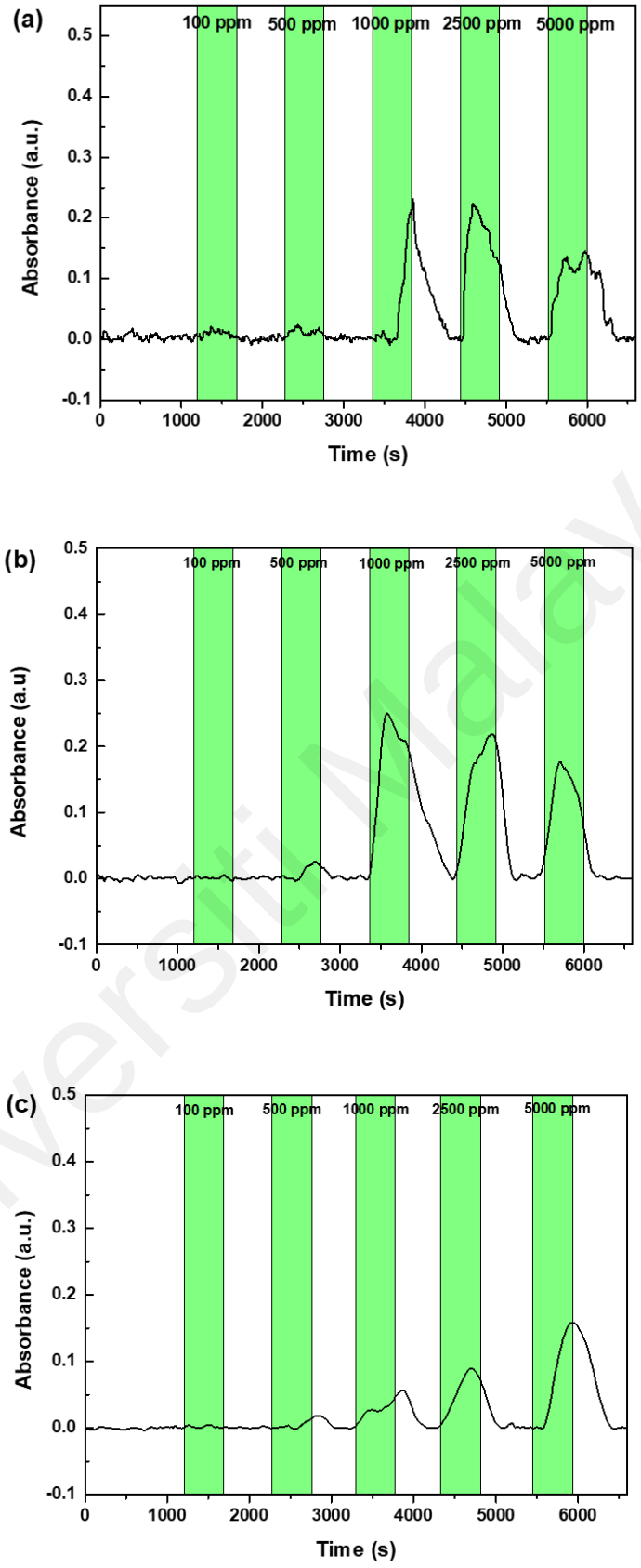

Figure: 4.9: Dynamic respond of a) 0.01M, b) 0.025M and c) 0.05M of *h*-MoO_3 when exposed to 100-5000 ppm of NH_3

Among the three different concentrations of precursor used, 0.025M of AHM used show a more significant and stable absorbance when compare to 0.01M and 0.05M AHM used. This might due to the under-deposition or over-deposition of MoO_3 on the tapered region when using 0.01M and 0.05M of AHM. An over-deposited sensing layer will cause insufficient of evanescent wave to functionalized the material surface which is important for gas-material interaction. As shown in Figure 4.9 (a) there is no absorbance when 500 ppm of NH_3 are purged in the gas chamber. This might due to the insufficient material needed for the reaction to take place. In the other hand, deposition using 0.05M of AHM shown in Figure 4.9 (c) causes absorbance signal drop. Hence, 0.025M of AHM is the optimum concentration and will be used throughout the whole NH_3 testing experiment.

4.1.2.2.2 Sensing performance of *h*-MoO_3 using different deposition time with Ammonium Heptamolybdate (AHM) precursor

0.025M of AHM precursor was continued to be used for this testing parameter. Deposition time is also another crucial parameter to fine tune the MoO_3 deposition. The chemical bath deposition method used in this research is two stage deposition inspired by Arpan Dhara (2014). Which he mentions that the first stage of the deposition is mainly focusing on the nucleation and second stage is growth focused. The shorter the time in the first stage bath, the greater is the width of the rods. This can be explained in general by lower nucleation density on the substrate resulting in larger rods since the same amount of available reactant is divided by a smaller number of nuclei. So, by adjusting these two different time durations we are able to adjust the nanostructure growth on the tapered optical fiber. In this section, the deposition time has changed to 30 minutes for the first stage and maintaining10 minutes for the second stage respectively.

Figure 4.10. shows the absorbance respond for the 30 minutes deposition of MoO_3 which shows a much more unstable result comparing the 20 minutes deposition. This might due to the thicker nanostructure formed on the fiber and restrict the propagation of the evanescent wave to functionalized the MoO_3 surface. Hence, the further experiment was carried out with 20 minutes first stage deposition and 10 minutes for the second stage deposition.

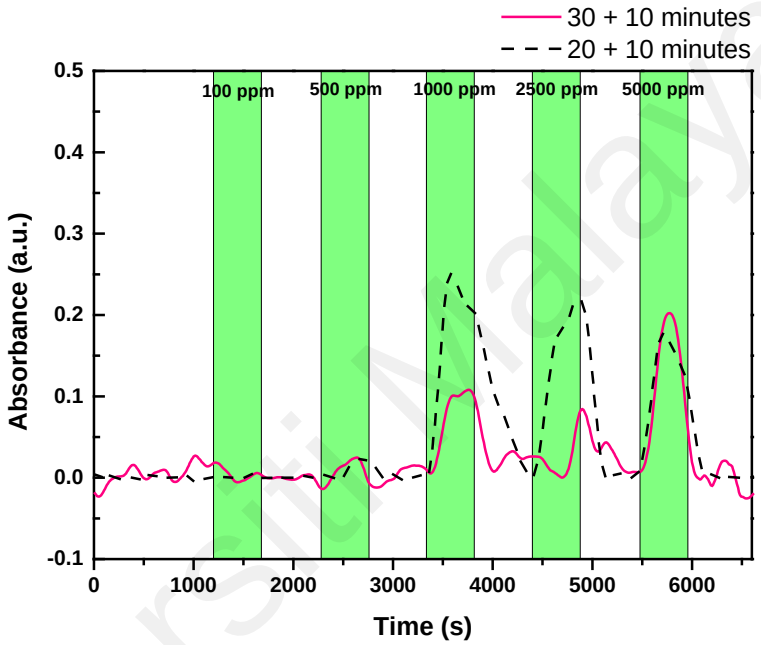

Figure 4.10: Dynamic respond of AHM precursor deposited in 30+10 minutes and 20+10 minutes when exposed to 100-5000 ppm of NH_3

4.1.2.2.3 Sensing performance of annealing effect on *h*-MoO_3 deposited from Ammonium Heptamolybdate (AHM) precursor

In semiconductor metal oxide gas sensor, many reported that annealing the sensing material will have an effect on the physical and chemical properties which will then affect the gas sensing capability(Al-Hashem, Akbar, & Morris, 2019; S. Yang et al., 2019b). To further investigate the effect of annealing, the sensing performance of sample annealed at 150^{o}C has been compared with the as prepared sample.

Figure 4.11 (a) shows the dynamic respond of both the annealed sample and the as prepared sample and Figure 4.11 (b) shows the absorbance shift of the annealed sample in an absorbance vs wavelength graph. It can clearly be seen that the annealed sample shows more sensitive respond compare to the as prepared sample as the annealed sample can detect 500 ppm of NH_3 gas. This has proved that by annealing the *h*-MoO_3 material will then increase the active sites on the material surface which will improve the sensing ability. But the sensor respond is not consistent along the increasing of NH_3 concentration. This might cause residual absorbed H^+ from the NH_3 gas does not remove all from the MoO_3 sensing layer by the purging of synthetic air(Borgschulte et al., 2017). In the other hand, without elevated temperature, the hydroxyl ions and water molecules that still exists in the crystal lattice may hinder the desorption process accordingly(C. Wang, Yin, Zhang, Xiang, & Gao, 2010b). In the absorbance vs wavelength graph, the higher the concentration of the NH_3 gas purged the higher the intensity of the wavelength shift.

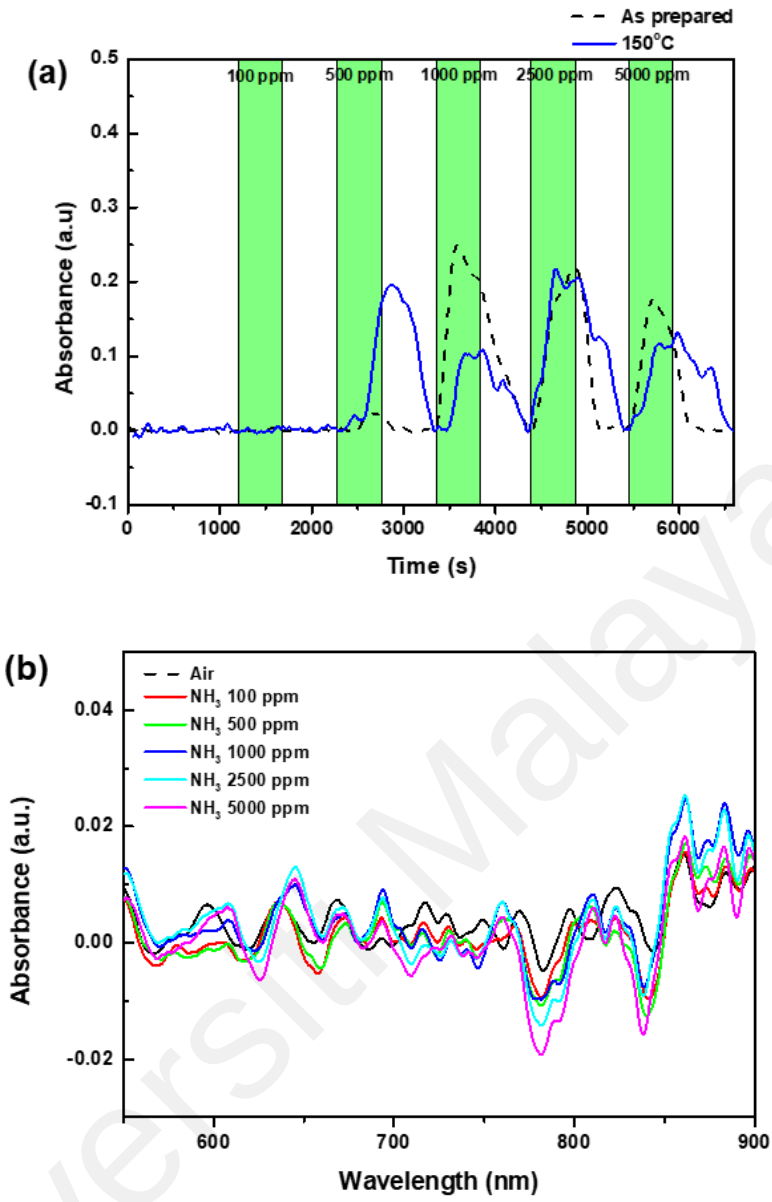

Figure 4.11: (a) Dynamic respond of 150°C annealed sample compare with as prepared sample and (b) absorbance vs wavelength graph when exposed to 100-5000 ppm of NH_3

The response time and recovery times for all the sample under exposure of NH_3 concentration form 100 ppm to 5000 ppm has been tabulated in Figure 4.12.(a) and (b). The respond and recovery time of this sample show not much significant improvement even after annealing treatment.

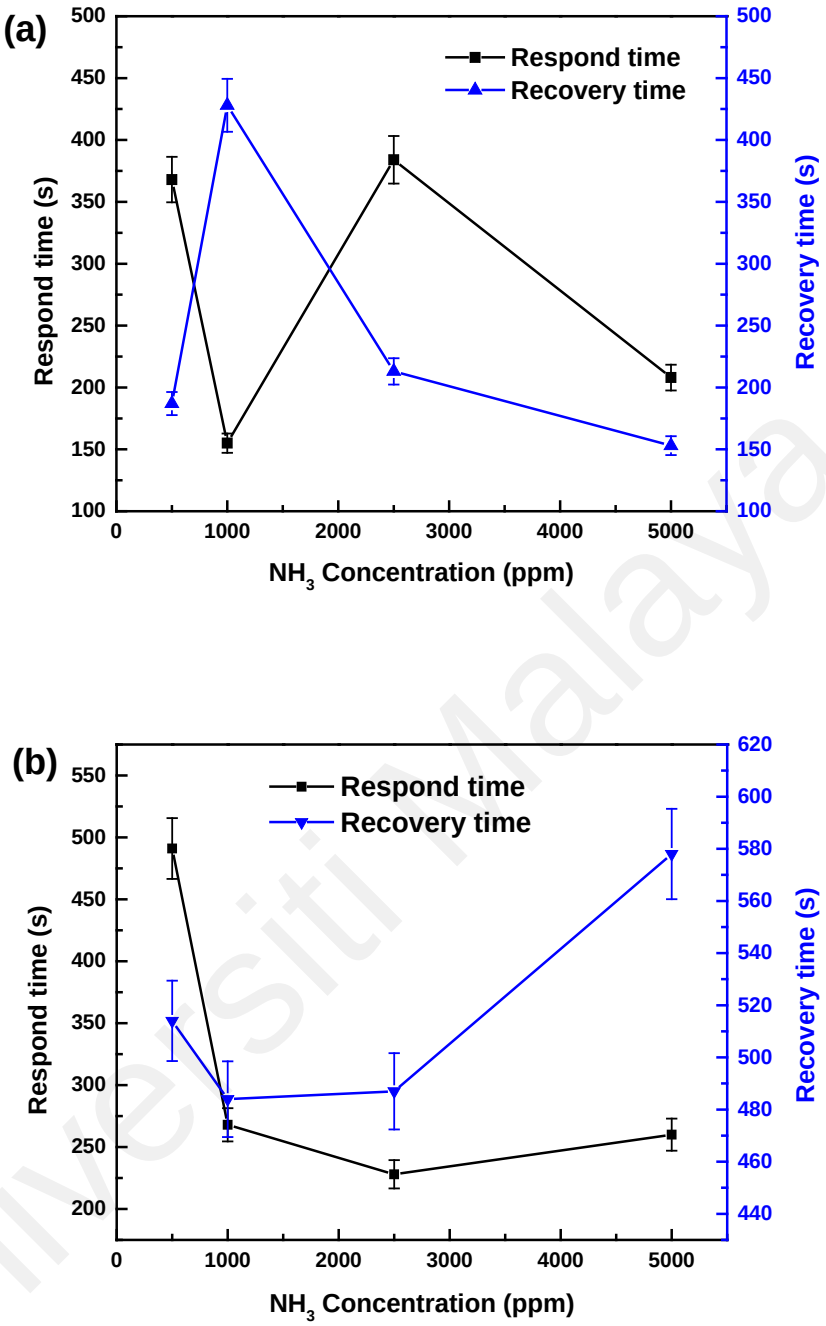

Figure 4.12: (a) Respond and recovery time for as prepared sample compare with (b) annealed sample when exposed to 500-5000 ppm of NH_3

The average value of the sensitivity respond for the annealed sample at each concentration was calculated and plotted a sensitivity curve shown in Figure 4.13. Based in Figure 4.13., the relationship of the absorbance and the exposed concentration shows a typical saturation pattern. A log fitting was use to fit the experimental data with a relatively good coefficient shown in the Figure 4.13.

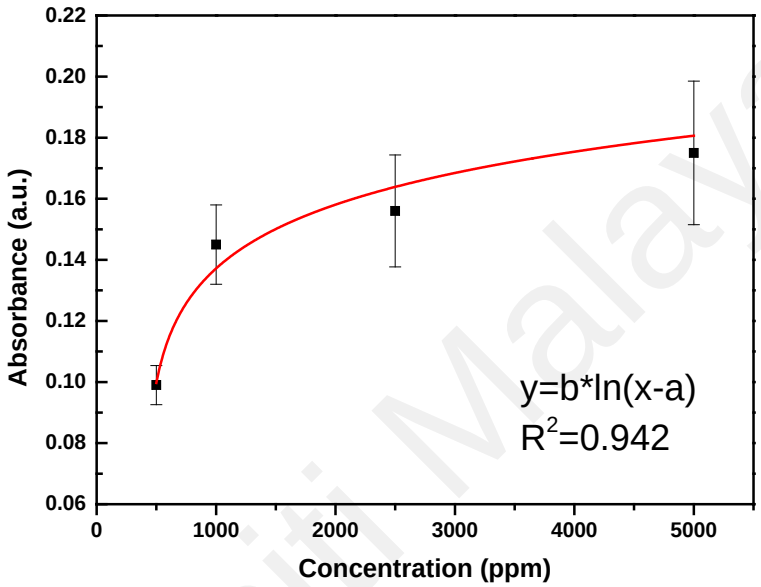

Figure 4.13: Sensitivity curve of the average absorbance change as a function of NH_3 concentration of sensor annealed *h*-MoO_3

4.1.2.2.4 Repeatability and selectivity test of annealed *h*-MoO_3 deposited from Ammonium Heptamolybdate (AHM) precursor

In order to test the repeatability of the annealed *h*-MoO_3, the sample was purged with 10 000 ppm of NH_3 in three on/off cycle. As shown in the Figure 4.14(a) the annealed sample exhibits a good repeatability of constant gas flow with around 0.1 a.u. in the 3 cycles. However, in the selectivity test as shown in Figure 4.14 (b), the annealed sample shows a relatively weak selectivity as all the different gases such as 10 000 ppm of H_2 gas and CH_4 gas purged into the camber will have reaction with the sensing material. Hence, ammonia-based MoO_3 is not a suitable candidate to fabricate a fast respond NH_3 gas sensor due to its inconsistency on absorbance over increment of concentration of NH_3 and also its weak selectivity performance despite its slightly higher in sensitivity after annealing treatment.

This inspired us to explore different type of precursor in order to synthesis a NH_3 sensitive MoO_3 sensing layer. The next section will present and discuss on the MoO_3 nanostructure synthesis using Sodium molybdate (Na_2MoO_4). The investigation covers on the MoO_3 characterization and its NH_3 sensing properties.

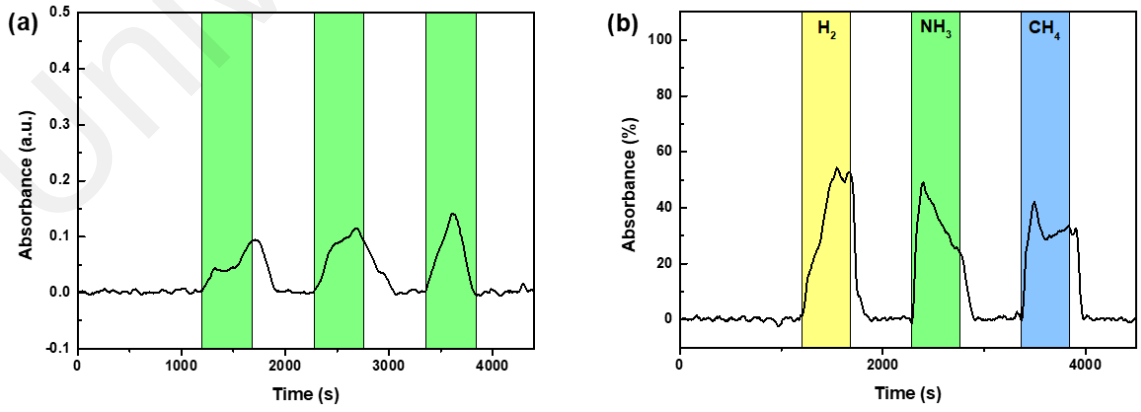

Figure 4.14: (a) Repeatability and (b) selectivity test of the annealed *h*-MoO_3 NH_3 sensor

4.2 *h*-MoO_3 using Sodium molybdate (SM) as precursor

4.2.1 Characterization of *h*-MoO_3 using Sodium molybdate (SM) on tapered optical fiber

4.2.1.1 FESEM

As mention previously that the morphology of the nanostructure formed will greatly affect the gas sensing capability of the material. Hence in this section, we will explore the different characteristic of the MoO_3 prepare by using different type of starting precursor which is the Sodium molybdate (SM).

The *h*-MoO_3 nanorod are well deposited on the tapered optical fiber shown in the FESEM image in Figure 4.15 (a) & (b). The as grown *h*-MoO_3 nanorods are around 14-20 nm thick with a rod length of 400-500 nm as determined by the FESEM is shown in Figure 4.15 (c). The Figure 4.15 (d) and (e) shows the *h*-MoO_3 nanorod annealed at 150^{o}C and 200^{o}C and that the nanorods have diameters of around 23 nm–37nm and 47 nm–57 nm. However, the length of the nanorod doesn't change much which stays around 400 nm-500 nm. This shows an increase of nanorod thickness when increase the annealing temperature. The figure 4.15 (e) shows a seed-like structure on the edge of the nanorod and the top of the substrate, which is the Pt sputtering coating before the FESEM imaging.

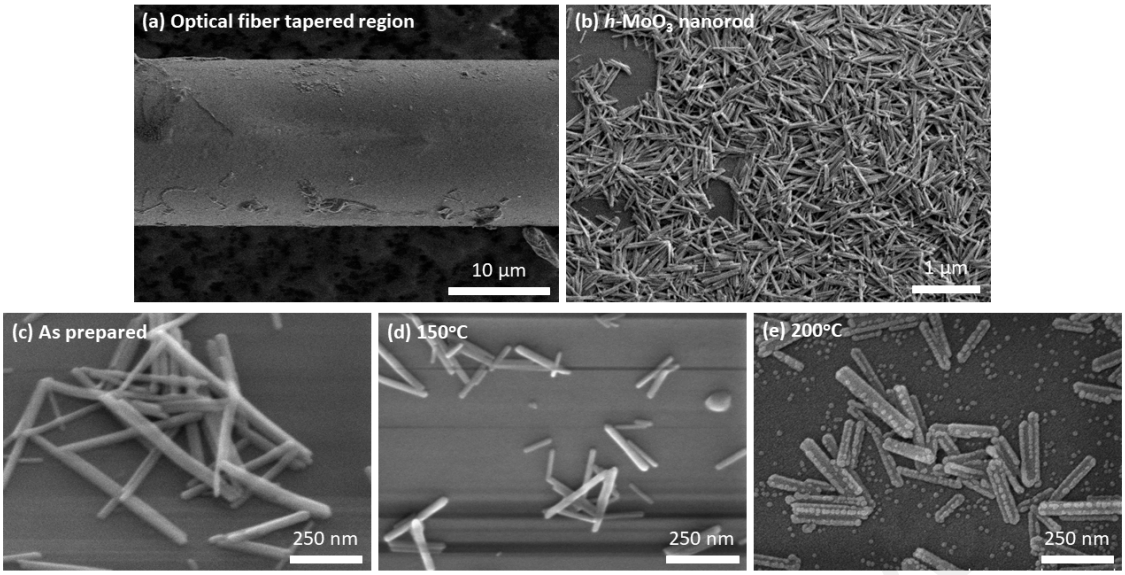

Figure 4.15: FESEM image of (a) tapered MMF coated with *h*-MoO_3 nanorod, (b) *h*-MoO_3 nanorod, (c) as prepared sample, (d) 150°C annealed sample and (e) 200°C annealed sample.

4.2.1.2 EDS

EDS was performed to verify the element that exists in the synthesized *h*-MoO_3. The EDS pattern displayed in Figure 4.16. shows the oxygen (O) with the highest peak which follow by the silicon (Si) which is due the material of the tapered optical fiber and lastly the Molybdenum (Mo). There is also detection of sodium element (Na) which is due to the choice of precursor used. A carbon (C) peak has been detected in the EDS around 0.2-0.3 keV, this is due to the carbon introduce from the environment. Hence, it's not included in the calculation. EDS mapping in figure 4.17 shows. *h*-MoO_3 has been coated on the optical fiber. This was then further confirmed with the FTIR characterization.

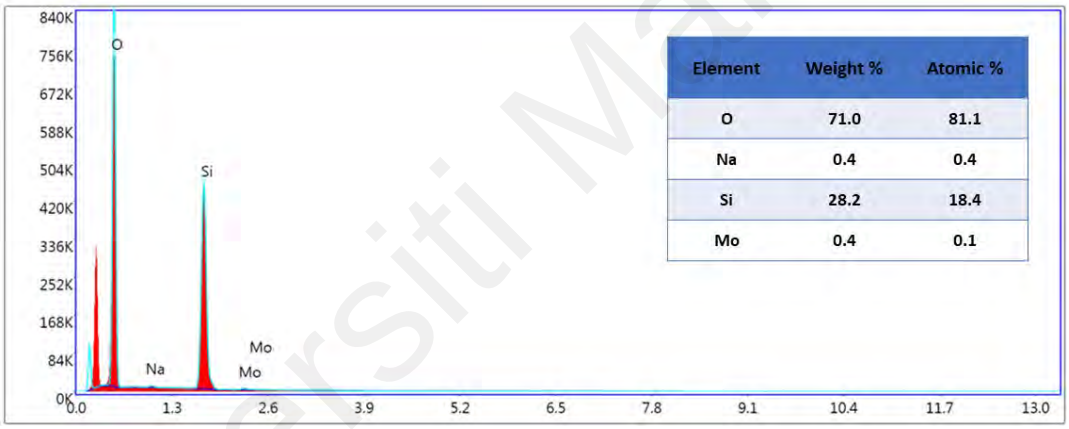

Element	Weight %	Atomic %
O	71.0	81.1
Na	0.4	0.4
Si	28.2	18.4
Mo	0.4	0.1

Figure 4.16: EDS measurement of *h*-MoO_3 nanostructure

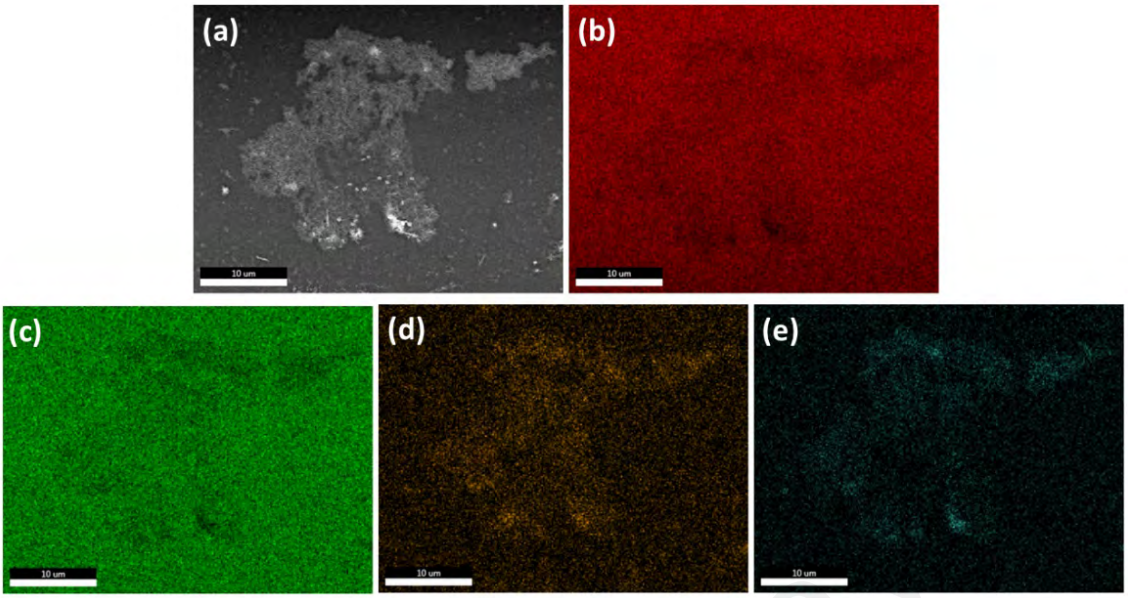

Figure 4.17: EDS mapping of (a) *h*-MoO_3 nanostructure coated on optical fiber with (b) Oxygen, (c) Silica, (d) Sodium, and (e) Molybdenum

4.2.1.3 XRD and SAED

The XRD patterns of all two samples (as prepared & 150°C) are shown in the Figure 4.18. The diffraction peaks of all sample can be indexed to the hexagonal phase of MoO_3 (JCPDS Card No. 00-021-0569) with a space group *P*63(Hu, Deng, Xu, Zhang, & Sun, 2015). The sharp peak at 2 theta = 9.6°, 19.2°, 25.5°, 29.3° are indexed as (100), (200), (210) and (300) crystal plane of *h*-MoO_3 phase. The obtained sample are single crystalline hexagonal phase without any secondary phase. The significant of the (300) peak proves the presence of Na atom in the sample (JCPDS Card No. 00-022-0948). This shows that the sample shares the same structure with the previously deposited *h*-MoO_3 using AHM as precursor. Fig. 4.19 shows a typical hexagonal SAED pattern for the *h*-MoO_3 nanorod, which is consistent with the XRD's result.

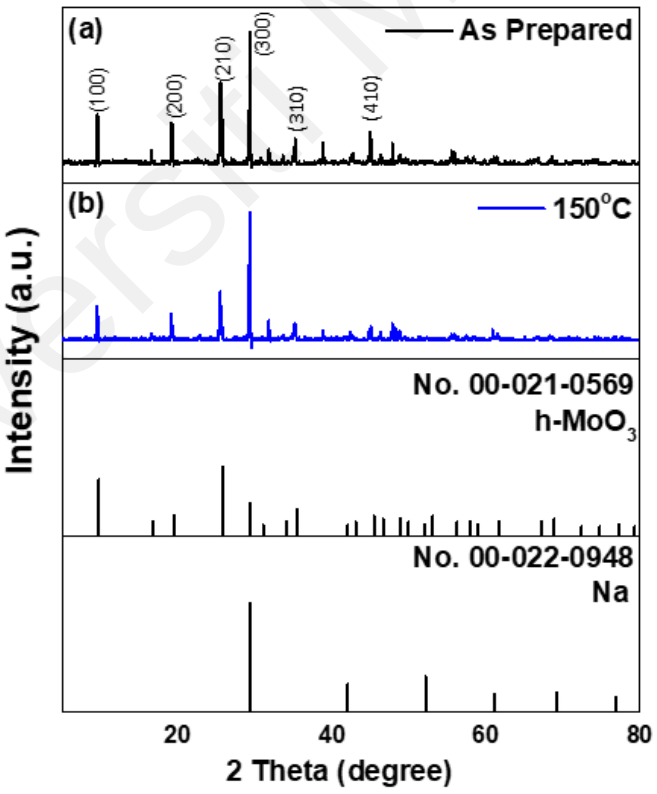

Figure 4.18: XRD pattern for both sample (a) as- prepared and (b) annealed *h*-MoO_3

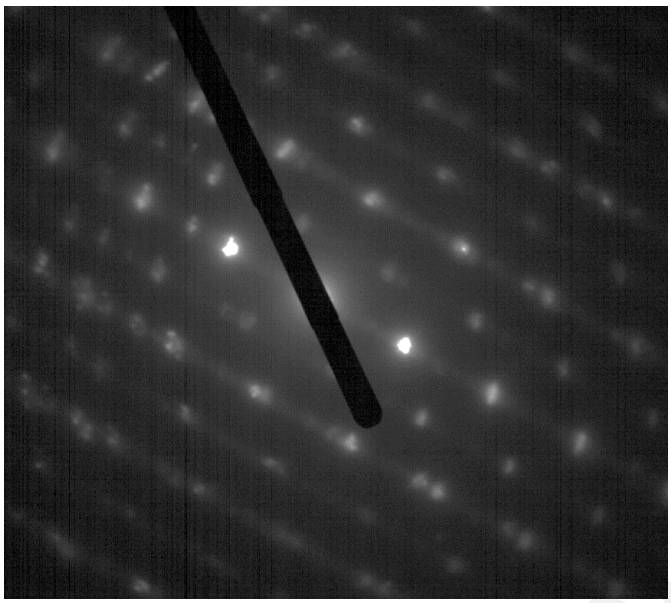

Figure 4.19: SAED patterns for *h*-MoO_3 sample annealed at 150°C

4.2.1.4 FTIR

The element composition and the phase of the prepared and annealed *h*-MoO_3 is well supported by the FTIR analysis. The FTIR spectra of the as prepared sample and the annealed sample are shown in Figure 4.20. Both the sample shows the characteristic vibrational peak of *h*-MoO_3. Here the Mo-O peaks are observed between 1000 cm^{-1} and 400 cm^{-1}. The most significant peak observed at 897 cm^{-1} and 968 cm^{-1} are attribute to the stretching vibration of molybdenum atom double bonded to oxygen atom (Mo=O). the peaks at around 693 cm^{-1} are corresponds to the Mo-O stretching bond. Furthermore, the peaks observed at 3506 cm^{-1} and 1622 cm^{-1} are attribute to the stretching and bending vibration of water molecules(Chithambararaj et al., 2016; Z. Li et al., 2017).

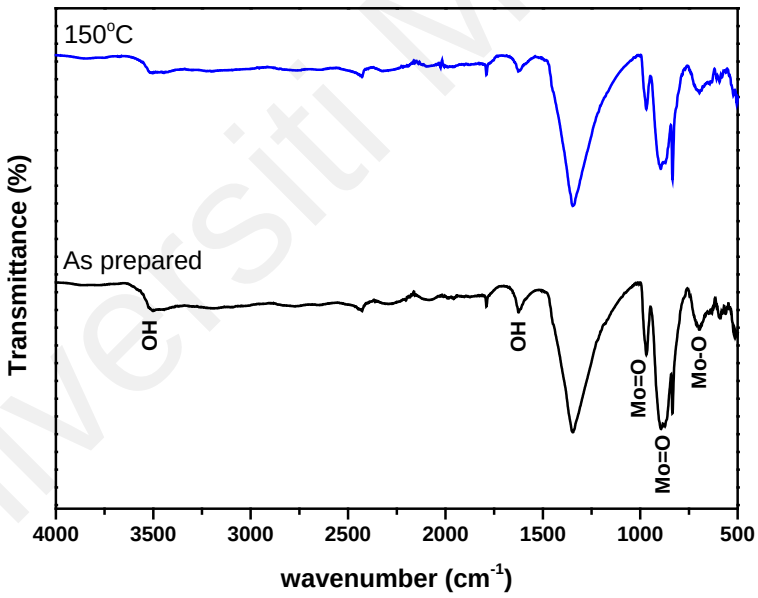

Figure 4.20: FTIR spectra of as prepared and annealed *h*-MoO_3

4.2.1.5 XPS

The valance state of Mo and the non-stoichiometry of *h*-MoO_3 nanorod play a vital role in optical gas sensing, as they act as the active sites for the material–gas interaction.(S. Bai et al., 2015; de Castro et al., 2017; S. Yang et al., 2015) Fig. 4.21 shows the narrow scan XPS spectra of Mo 3d and O 1s' energy region for the *h*-MoO_3 nanorod when annealed at different temperatures. In Fig. 4.21(a), the $3d_{5/2}$ and $3d_{3/2}$ peaks, which are located at 236 eV ± 0.1 eV and 232.8 eV ± 0.1 eV, respectively, can be assigned to the spin orbit doublets of Mo6+ in the samples. However, the Mo^{5+} ions are represented by the lower peaks in the pattern of dotted lines, which shifts to lower binding energies (S. Yang et al., 2015). After annealing, the Mo^{5+} oxidation state appears to increase. This shows that the reduction of Mo^{6+} to Mo^{5+} is caused by a large number of oxygen vacancies, which are introduced by annealing the *h*-MoO_3 (Xiang, Han, Zhang, & Chen, 2015). None of the peaks corresponded to the Mo metal has been detected. Fig. 4.21(b) shows the XPS spectra in the O 1s energy region, which consists of peaks related to oxides and other types of chemisorbed oxygen species. The peak at 530.5 eV ± 0.1 eV is associated with the oxygen atom bonding with the Mo ions (Mo–O), whereas the peaks that occur at around 532.8 eV ± 0.1eV are associated with the other oxygen species that are attached to the surface and around the sample.

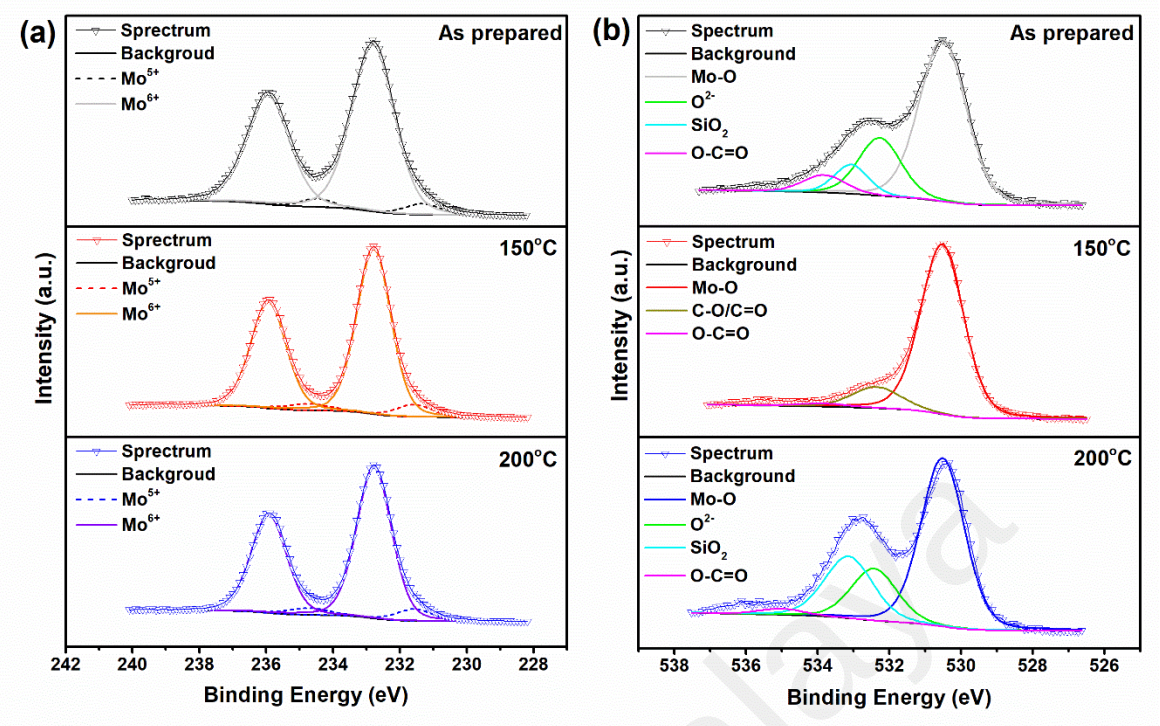

Fig. 4.21: XPS spectra of (a) Mo 3d and (b) O 1s core level spectra of *h*-MoO_3 nanorod in different annealing temperature.

4.2.1.6 TGA

TGA allow the understanding of the sample's thermal stability which helps in determining the annealing temperature in the process of nanostructure modification. Based on Figure 4.22 shown below, the mass loss of *h*-MoO_3 is slightly different from Ammonia based MoO_3. Sodium based MoO_3 doesn't undergoes any phase change when increase in temperature. However, it just continues to loss it's mass proportional with the increasing of temperature of 10^{o}C/min until the whole material decompose. Hence, this shows that the sodium-based *h*-MoO_3 have a lower melting point than the ammonia bases *h*-MoO_3 which unable to withstand a high temperature. Annealing the sodium-based *h*-MoO_3 might cause the decomposition of the Mo in the material.

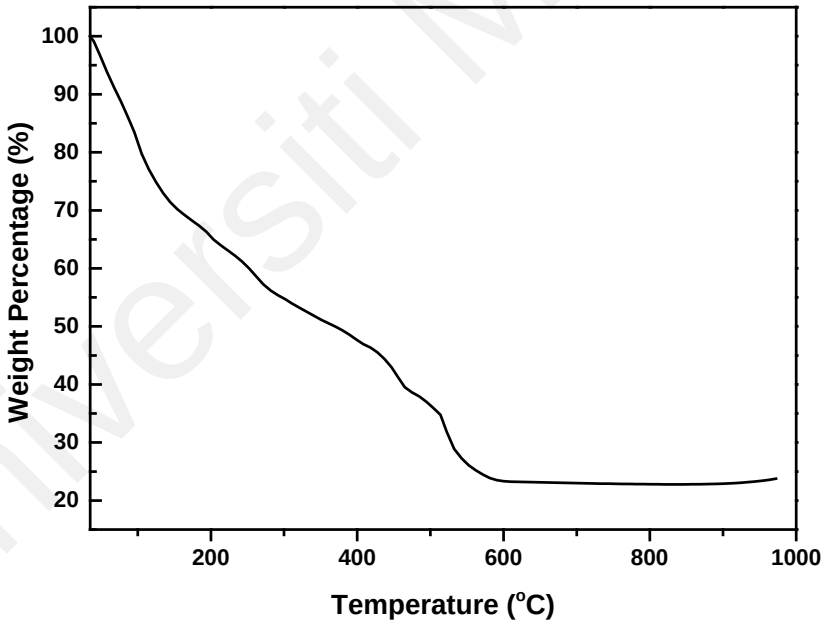

Figure 4.22: TGA curve of the synthesized *h*-MoO_3 powder

4.2.1.7 Uv-Vis

The optical band gap of synthesized and annealed *h*-MoO_3 can be estimate with the plot $(ahv)^2$ versus hv. The absorbance spectrum obtained from the Uv-Vis measurement is use to plot $(ahv)^2$ versus hv so that the optical band gap can be estimated using Tauc plot(Makuła, Pacia, & Macyk, 2018). The value of the optical band gap (E_g) can be measured by taking the tangent to the curve across the hv axis as demonstrated in Figure 4.23. From the graph, the estimated band gap is 3.50eV for as prepared *h*-MoO_3 and 3.70eV for annealed *h*-MoO_3 which has a smaller optical band gap comparing with AHM precursor. The result shows the slight increase of band gap when the increase of annealed temperature to 150^{o}C. The increases of optical band gap after annealing process is highly influenced by the gap states that are generated by the oxygen vacancies (Yao et al., 2019)and the change in charge carriers which can be explained by the Burstein Moss (BM) effect(Khelchand Singh & Rajkumari, 2019).

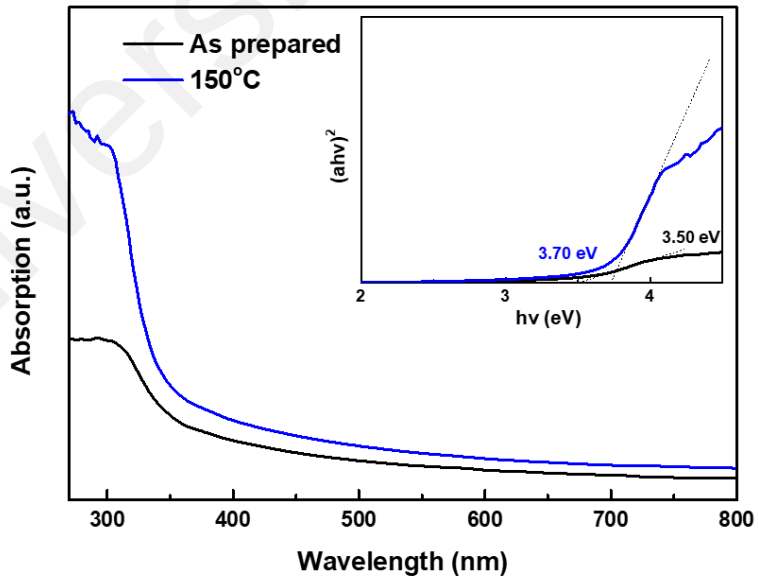

Figure 4.23: Estimated optical band gap of as prepared and annealed *h*-MoO_3.

4.2.2 Absorbance measurement of *h*-MoO_3 using Sodium Molybdate (SM) on tapered optical fiber towards NH_3 gas sensing

This section will discuss on the optical responses exhibited when sensors exposed to different concentration of NH_3. The sensing performance investigated were based in the response and recovery time, sensitivity and also repeatability and its selectivity. The sensor developed from *h*-MoO_3 nanostructure coated on tapered optical fiber were investigated in terms of its precursor concentration, deposition time during the CBD and also the annealing effect.

4.2.2.1 Sensing performance of as prepared *h*-MoO_3 using 0.1M Sodium Molybdate (SM) precursor

In this section, we only use the concentration of 0.1M Sodium Molybdate (SM) to coat on the tapered optical fiber. This is because concentration lower than 0.1M have little to none visible deposition on the gas substrate during the testing of deposition. Hence, the experiment was proceeded with 0.1M of SM in the further experiment. All the other parameter of the experiment such as temperature and deposition time is fixed to ensure that the sample have similar coating time. The NH_3 gas sensing was conducted in room temperature. Figure 4.24 shows the dynamic respond of 0.1M SM from the chemical bath deposition process.

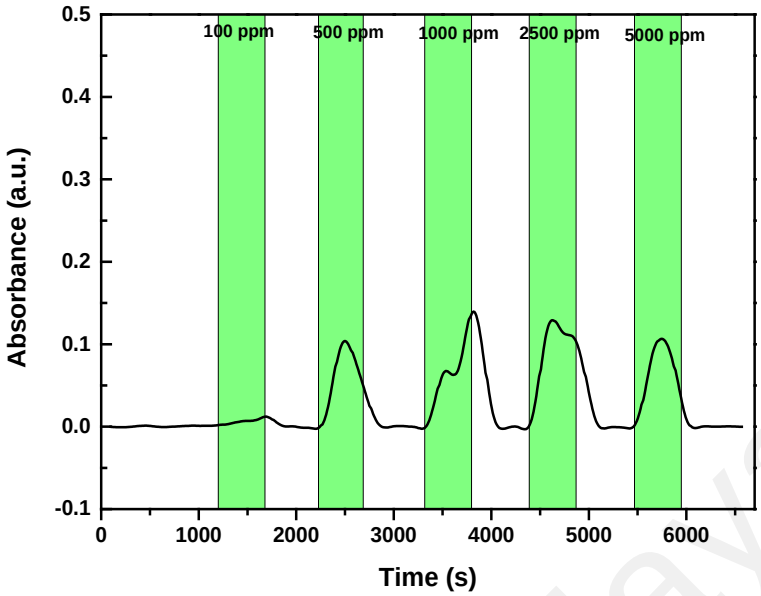

Figure: 4.24: Dynamic respond of *h*-MoO_3 from 0.1M of SM precursor when exposed to 100-5000 ppm of NH_3

The as prepared sample shows a relatively stable absorbance towards 500 ppm to 5000 ppm of NH_3 which is around 0.1-0.15 of absorbance unit. It also shows a very small respond of absorbance when only 100 ppm of NH_3 gas was purged into the chamber.

4.2.2.2 Sensing performance of different deposition time of *h*-MoO_3 using Sodium molybdate (SM) as precursor

0.1M of SM was continue to be used for this testing parameter. Deposition time is also another crucial parameter to fine tune the MoO_3 deposition. The chemical bath deposition method used in this research is two stage deposition inspired by Arpan Dhara et al. (2014). Which he mentions that the first stage of the deposition is mainly focusing on the nucleation and second stage is growth focused. The shorter the time in the first stage bath, the greater is the width of the rods. In this section, the deposition time has changed to 30 minutes for the first stage and 10 minutes for the second stage respectively.

As shown in Figure 4.25 the absorbance respond for the 30 minutes deposition of MoO_3 shows a much more unstable result comparing the 20 minutes deposition. This might also due to the thicker coating that limit the evanescent wave to functionalized the MoO_3. The further experiment was carried out with 20 minutes first stage deposition and 10 minutes for the second stage deposition.

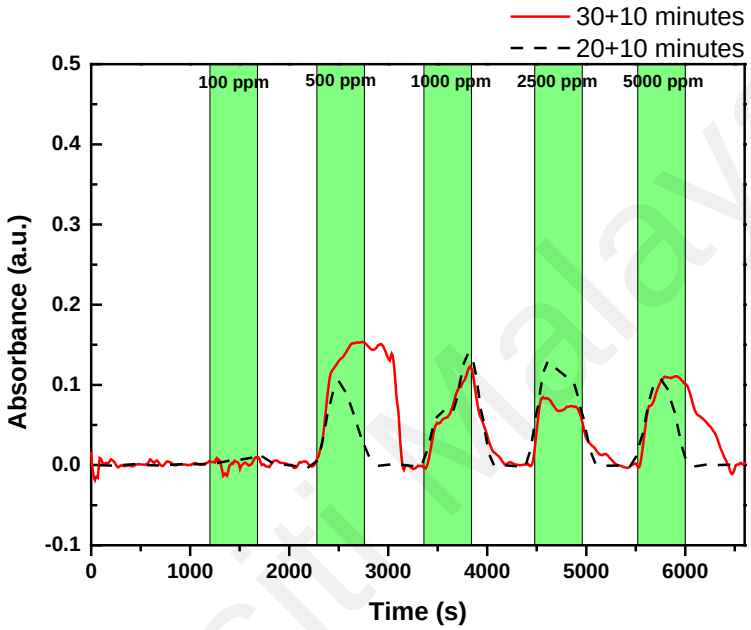

Figure 4.25: Dynamic respond of *h*-MoO_3 deposited in 30+10 minutes and 20+10 minutes when exposed to 100-5000 ppm of NH_3

4.2.2.3 Sensing performance of annealing effect on *h*-MoO_3 deposited from Sodium Molybdate (SM) precursor

Different type of MoO_3 formed by using different precursor will have different effect upon the annealing treatment due to its different number of oxygen vacancy. This will also lead to a different sensing ability as oxygen vacancy will act as the gas sensing active site. To further investigate the effect of annealing, the sensing performance of sample annealed at 150^oC has been compared with the as prepared sample.

We can clearly see that in Figure 4.26 (a) the annealed sample have a higher sensitivity compare to the as prepared sample up to even 0.2 a.u. which is almost 100% more that as prepared sample in 500 ppm of NH_3. In other NH_3 concentration also shows a significant increase in absorbance unit. There are works reported on a significant increase on the gas sensing ability when using a Na doped metal oxide for gas sensing application(Chandra, Sahu, Dwivedi, & Mishra, 2017; Dai, Liang, & Lee, 2019). The author believes that forming sodium based-MoO_3 help in improving the overall sensitivity also respond and recovery time. Figure 4.26 (b) shows also a significant wave shifts when exposed to different concentration of NH_3 gas.

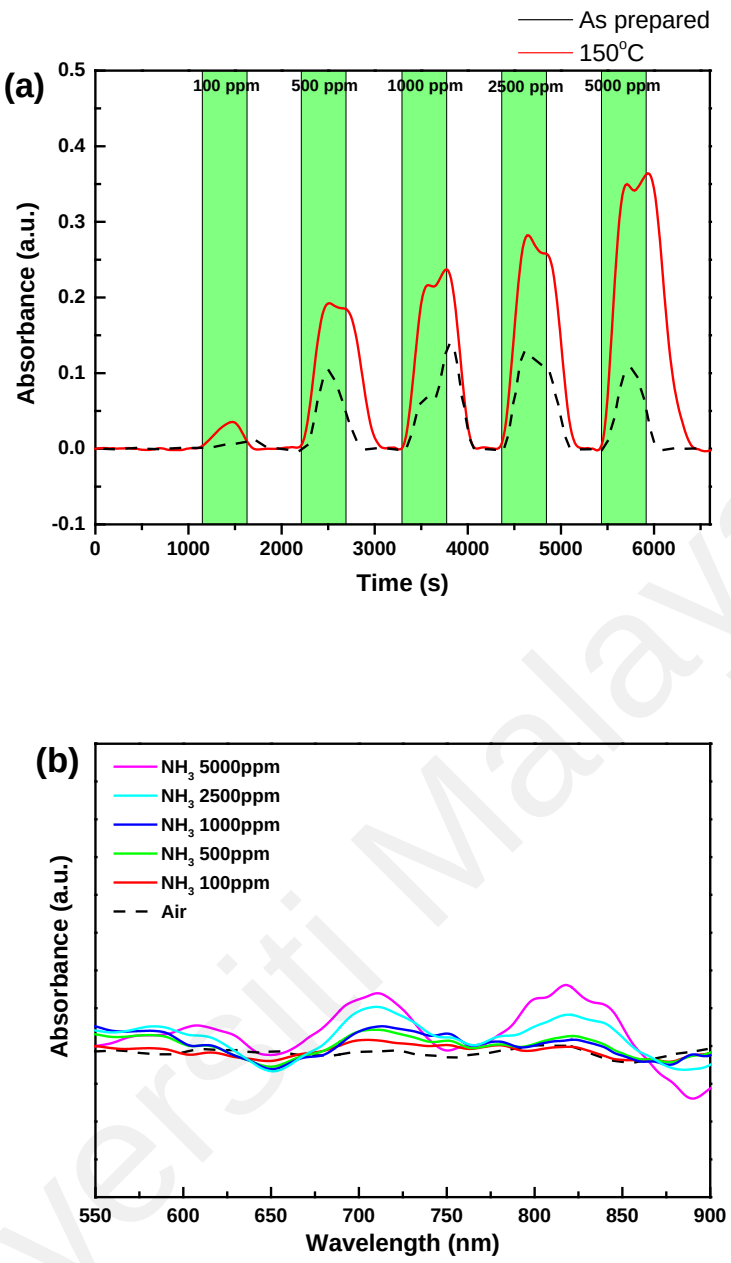

Figure 4.26: (a) Dynamic respond of 150ºC annealed sample compare with as prepared sample and (b) absorbance vs wavelength graph of annealed sample when exposed to 100-5000 ppm of NH_3

Due to its positive respond from the 150ºC sample, a different set of *h*-MoO_3 sample had annealed up to 200ºC to test its performance. The 200ºC sample shows a slight increase of sensitivity towards NH_3, but its losses the response consistence along the increment of NH_3 concentration as shown in Figure 4.27. This might due to the lower

thermal stability of the sodium-based MoO_3 which decomposes after increases in temperature. Hence, no further work was carried out for 200°C *h*-MoO_3 sample.

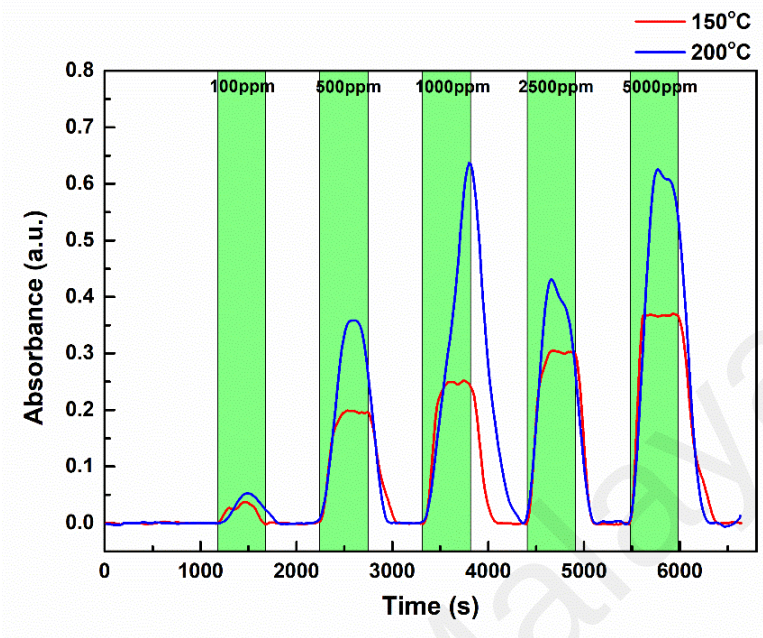

Figure 4.27: Dynamic respond of 150°C & 200°C annealed sample

The response time and recovery times for both the as prepared and annealed sample respond in NH_3 concentration form 100 ppm to 5000 ppm has been tabulated in Figure 4.28 (a) and (b) respectively.

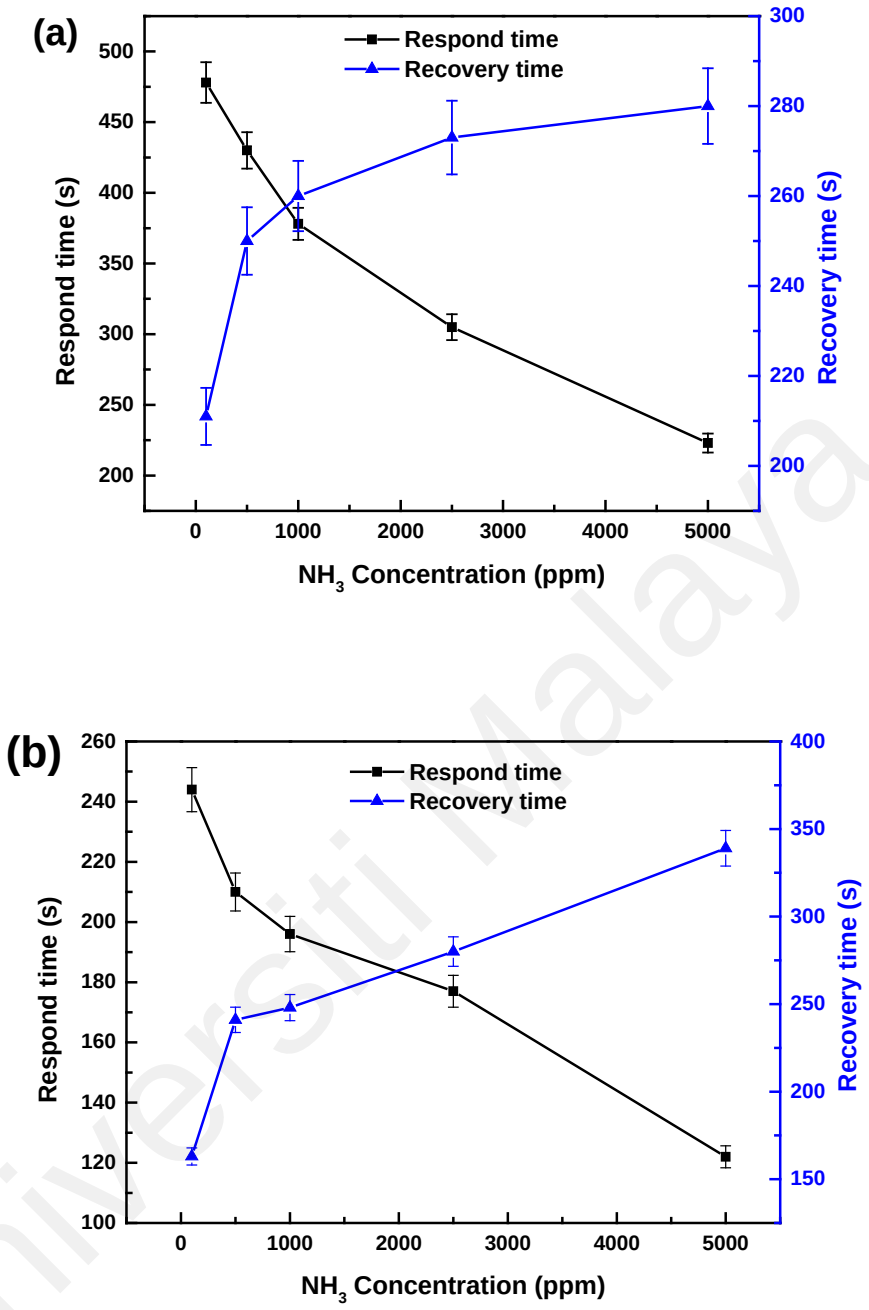

Figure 4.28: (a) Respond and recovery time for as prepared sample compare with (b) annealed sample when exposed to 100-5000 ppm of NH_3

This time, we are able to see significant improvement of respond and recovery time from the annealed sample. the annealed shows a reduce of 215 s when expose to 500 ppm of NH_3. As the recovery time also improve by reduced in 10 s.

The average value of the sensitivity respond at each concentration was calculated and plotted a sensitivity curve shown in Figure 4.29. Based in Figure 4.29.(a) and (b), the relationship of the absorbance and the exposed concentration shows a typical saturation pattern. A good log fitting was use to fit the experimental data with a relatively good coefficient shown in the Figure 4.29 below.

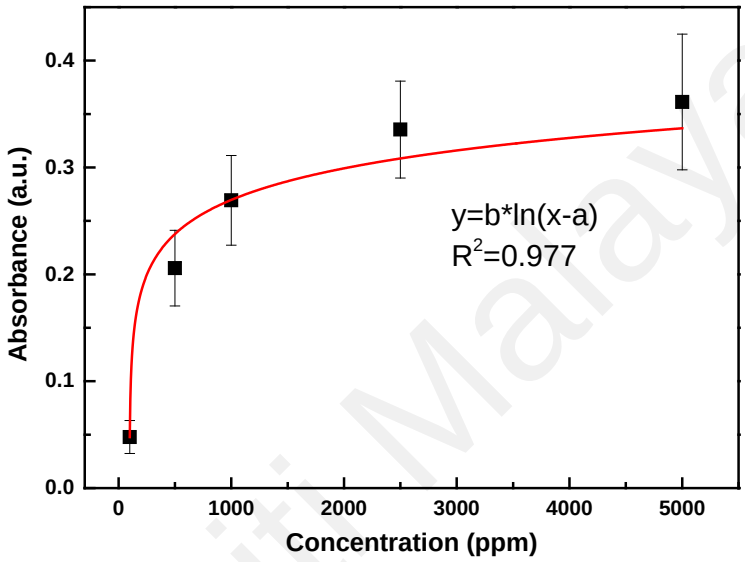

Figure 4.29: Sensitivity curve of the average absorbance change as a function of NH_3 concentration of sensor annealed *h*-MoO_3

4.2.2.4 Repeatability and selectivity test of annealed *h*-MoO_3 deposited from Sodium Molybdate (SM) precursor

In order to test the repeatability of the annealed *h*-MoO_3, the sample was purged with 10 000 ppm of NH_3 in three on/off cycle. As shown in the Figure 4.30 (a) the annealed sample exhibits a good repeatability of constant gas flow with around 0.32 a.u. in the 3 cycles. In addition, in the selectivity test as shown in Figure 4.30 (b), the annealed sample shows a relatively high selectivity towards NH_3 gas and a 50% respond towards CH_4 gas and only 10% detection towards H_2. This have shown a relatively high selectivity towards NH_3 gas.

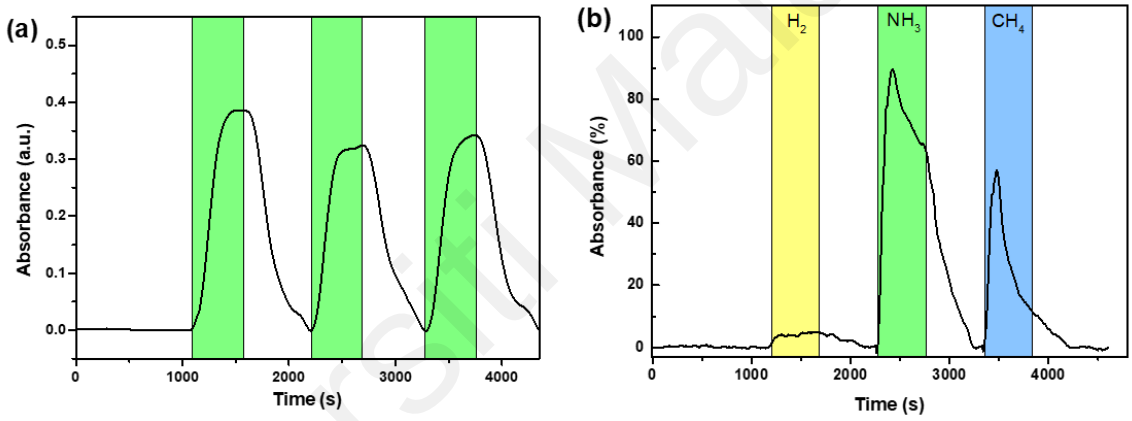

Figure 4.30: (a) Repeatability and (b) selectivity test of the annealed *h*-MoO_3 NH_3 sensor

4.3 Gas Sensing mechanism

As the metal oxide-based optical sensor has not yet been determined, this sensing mechanism is inspired by a chemiresistive sensing mechanism because the microscopic electrical properties of a SMO are closely related to its macroscopic optical properties. Figure 4.31 shows the graphical diagram of the NH_3 sensing mechanism of *h*-MoO_3 nanorod. Like the α-MoO_3, the sensing mechanism of *h*-MoO_3 comes from the Mo^{5+} ion-induced structural defects, where the Mo^{5+} ions act as adsorbing centres with a high affinity to gases(S. Yang et al., 2015).

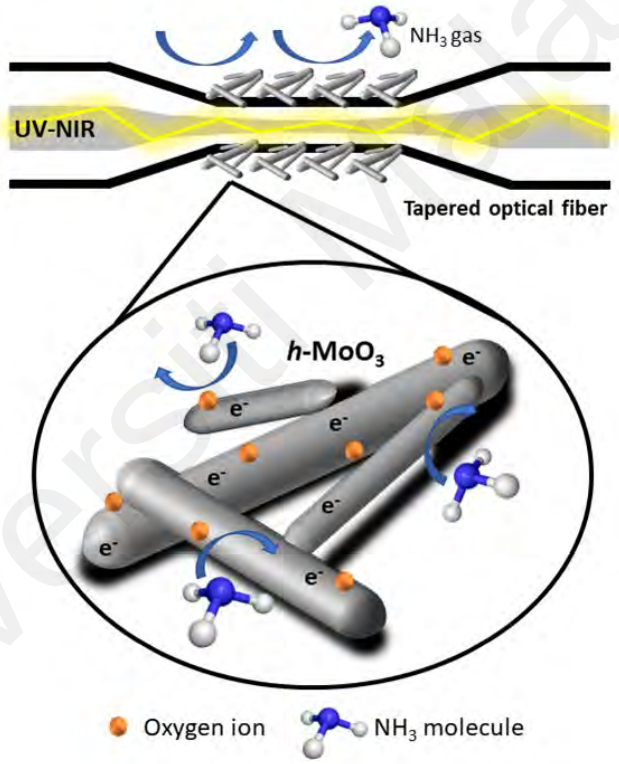

Figure 4.31: Graphical diagram of the NH_3 sensing mechanism of *h*-MoO_3 nanorod

First, the optical light propagates from the source to the detector, which passes through the *h*-MoO_3 coated tapered region. When the light is reflected in the tapered region, the evanescent wave that is produced will directly interact and activate the *h*-MoO_3's nanostructure.

When the sensor is exposed to an ambient environment, the oxygen molecule will adsorb onto the Mo^{5+} adsorbing centres on the *h*-MoO_3's surface as the oxygen vacant, as follows:

$$O_2\,(g) \longleftrightarrow O_2\,(ad) \quad \text{.....} \quad (4.1)$$

The chemisorption oxygen species will capture the free electron at the conduction band near the surface area, as follows(Dongwook Kwak et al.,2019):

$$O_2\,(ad) + e^- \longrightarrow O_2\,(ad) \quad \text{.....} \quad (4.2)$$

The free carrier absorption modifies the optical band gap, which is related to the interband transition and changes the evanescent wave at the interference of the sensing layer and the optical fiber(X. Zhang et al., 2019). This affects the transmittance of the light in the core region. Later, NH_3 gas is purged into the testing chamber and reacts with the chemisorbed oxygen ions, as follows(S. Kumar et al., 2020; N. K. Singh, Shrivastava et al., 2010):

$$4(MoO_3)\,O^- + 2NH_3 \longrightarrow 4MoO_3 + N_2O + 3H_2O + 4e^- \quad \text{.....} \quad (4.3)$$

or

$$3(MoO_3)\,O^- + 2NH_3 \longrightarrow 4MoO_3 + N_2 + 3H_2O + 3e^- \quad \text{.....} \quad (4.4)$$

or

$$5(MoO_3)\,O^- + 2NH_3 \longrightarrow 5MoO_3 + 2NO + 3H_2O + 5e^- \quad \text{.....} \quad (4.5)$$

This releases the previously trapped electrons and alters the optical band gap and the evanescent wave of the *h*-MoO_3, which increases the optical absorbance. Therefore, when the sensor is exposed to the surrounding air, the oxygen molecules in the air will be re-absorbed into the nanorod (mainly at the area of Mo^{5+}), which will trigger the restoration of the optical band gap. This model is sufficient to explain the sensing mechanism from the perspective of light(Andre at el., 2019).

CHAPTER 5: CONCLUSION

In this chapter, the overall research work and the findings of this Master thesis are summarised. The research contributions, achievements and suggestions for future work are outlined.

5.1. Conclusion

The objective of this research is to fabricate a hexagonal nanostructure molybdenum oxide for fast respond room temperature ammonia gas sensor. To accomplish this, a MMF was tapered and coated with MoO_3 nanostructure using 2 different precursors, which are ammonia heptamolybdate (AHM) and also sodium molybdate (SM). The sensor responds towards the NH_3 gas were measure based on the change of the absorbance within the visible-Infrared wavelength range. Generally, the fabricated sensor using both different precursor exhibits stable responds towards NH_3 in the concentration range of 100 ppm to 5000 ppm at room temperature. The sensing mechanism for the interaction of NH_3 gas and also the *h*-MoO_3 was determined and discussed. Referred on the comprehensive characterization and sensing result, the objectives outlined for this research project have successfully addressed.

The major findings of this research project based on the set objectives

Objective 1: To design and synthesize hexagonal molybdenum oxide nanostructures via chemical bath deposition

- The synthesis method of using low temperature Chemical Bath Deposition has successfully coated and deposited *h*-MoO_3 on the tapered region of the optical fiber for gas sensing.

- The use of different material-based precursor will result in the different morphology growth of nanostructure. The ammonia heptamolybdate (AHM) precursor favour the growth of nanograin like nanostructure and the sodium molybdate (SM) precursor favour the growth of nanorod like structure. The rodlike nanostructure is more favour in gas sensing application as it exhibits a larger total surface area for material and gas interaction.

- Annealing treatment on the *h*-MoO_3 has helped in improving the crystallinity of the *h*-MoO_3 as revealed in the XRD result. In addition to that, annealing will generate more oxygen vacancies in the metal oxides lattice in which acts as the active sites for gas adsorption resulting better sensing ability. This can be proved by comparing the as prepared and the annealed sample. Annealed *h*-MoO_3 formed using ammonia heptamolybdate (AHM) precursor shows a 0.2 a.u. of absorbance at 500 ppm but as prepared sample show almost none. In the other hand, annealed *h*-MoO_3 formed using sodium molybdate (SM) precursor shows more than 100% of absorbance increment when compare to the as prepared sample.

Objective 2: To fabricate a short respond time, highly sensitive, good repeatability and selective room temperature optical sensor for Ammonia gas.

- The respond and recovery time were also improved with the annealing treatment. By annealing, it has improved the material properties that promote fast sensing response. It was observed that the annealed *h*-MoO_3 using sodium molybdate precursor exhibits a respond time of only 210 s under 500 ppm of NH_3 in room temperature compare to the as prepared sample with 430 s.

- By comparing ammonia heptamolybdate (AHM) and sodium molybdate (SM) precursor, the *h*-MoO_3 formed using SM precursor acquire a more superior gas sensing ability in term of overall response sensitivity, respond and recovery time, repeatability and also selectivity. This is due to 2 main reasons, the nanorod like structure favours the gas sensing application and also the presence of Na species which reported improving in gas sensing performance and also higher NH_3 selectivity in this work.

As a summary, the research objectives on investigating and fabricating an optical NH_3 room temperature optical gas sensor coated with *h*-MoO_3 using chemical bath deposition has been successfully achieved.

5.2. Future Works

In this Master work, different synthesis parameter of *h*-MoO_3 such as (types of precursors used, concentration of precursor, deposition time and annealing temperature) was used to fabricate a room temperature NH_3 optical gas sensor. Throughout implementing the research work, several interesting research directions have been identified. Recommendations for future works are mentioned below:

- Doping plays an important factor in affecting the sensing ability of a sensor. In fact, by using sodium molybdate precursor result a doping phenomenon of *h*-MoO_3 produced. Which resulting to a better sensing performance when compare to ammonia-based precursor. Hence, types of doping can be further explored in the future work.
- Study on the nanocomposite of different type of metal oxide nanostructure. Incorporating different type of metal oxide nanostructure may help to stabilized the material in gas sensing reaction.

REFERENCES

Abashar, M. E. E. (2018). Ultra-clean hydrogen production by ammonia decomposition. *Journal of King Saud University - Engineering Sciences*, *30*(1), 2–11. https://doi.org/10.1016/j.jksues.2016.01.002

Abd Mutalib, M., Rahman, M. A., Othman, M. H. D., Ismail, A. F., & Jaafar, J. (2017). Scanning Electron Microscopy (SEM) and Energy-Dispersive X-Ray (EDX) Spectroscopy. In *Membrane Characterization* (pp. 161–179). https://doi.org/10.1016/B978-0-444-63776-5.00009-7

Abduldaem Mohammed, H., & Hanif Yaacob, M. (2020). Modified Single Mode Optical Fiber Ammonia Sensors Deploying PANI Thin Films. In *Optical Fiber [Working Title]*. https://doi.org/10.5772/intechopen.94001

Adschiri, T., Hakuta, Y., Sue, K., & Arai, K. (2001). Hydrothermal Synthesis of Metal Oxide Nanoparticles at Supercritical Conditions. *Journal of Nanoparticle Research*, *3*(2/3), 227–235. https://doi.org/10.1023/A:1017541705569

Al-Hashem, M., Akbar, S., & Morris, P. (2019, December 12). Role of Oxygen Vacancies in Nanostructured Metal-Oxide Gas Sensors: A Review. *Sensors and Actuators, B: Chemical*, Vol. 301, p. 126845. https://doi.org/10.1016/j.snb.2019.126845

Albaris, H., & Karuppasamy, G. (2020). Investigation of NH3 gas sensing behavior of intercalated PPy–GO–WO3 hybrid nanocomposite at room temperature. *Materials Science and Engineering B: Solid-State Materials for Advanced Technology*, *257*. https://doi.org/10.1016/j.mseb.2020.114558

Aldhafeeri, T., Tran, M. K., Vrolyk, R., Pope, M., & Fowler, M. (2020, September 1). A review of methane gas detection sensors: Recent developments and future perspectives. *Inventions*, Vol. 5, pp. 1–18. https://doi.org/10.3390/inventions5030028

Ali, S., & Farrukh, M. A. (2018). Effect of Calcination Temperature on the Structural, Thermodynamic, and Optical Properties of MoO3 Nanoparticles. *Journal of the Chinese Chemical Society*, *65*(2), 276–288. https://doi.org/10.1002/jccs.201700163

Andre, R. S., Mercante, L. A., Facure, M. H. M., Mattoso, L. H. C., & Correa, D. S. (2019). Enhanced and selective ammonia detection using In 2 O 3 /reduced graphene oxide hybrid nanofibers. *Applied Surface Science*, *473*, 133–140. https://doi.org/10.1016/j.apsusc.2018.12.101

Anil Kumar, Y., Singh, S., Kulurumotlakatla, D. K., & Kim, H. J. (2019). A MoNiO4 flower-like electrode material for enhanced electrochemical properties: Via a facile chemical bath deposition method for supercapacitor applications. *New Journal of*

Chemistry, *44*(2), 522–529. https://doi.org/10.1039/c9nj05529k

B. A. Ezekoye, B. A. E., P.O. Offor, P. O. O., V. A. Ezekoye, V. A. E., & F. I. Ezema, F. I. E. (2012). Chemical Bath Deposition Technique of Thin Films: A Review. *International Journal of Scientific Research*, *2*(8), 452–456. https://doi.org/10.15373/22778179/aug2013/149

Bai, H., & Shi, G. (2007). Gas Sensors Based on Conducting Polymers. *Sensors (Basel, Switzerland)*, *7*(3), 267. Retrieved from /pmc/articles/PMC3756721/

Bai, S., Chen, C., Tian, Y., Chen, S., Luo, R., Li, D., … Liu, C. C. (2015). Facile synthesis of α-MoO3 nanorods with high sensitivity to CO and intrinsic sensing performance. *Materials Research Bulletin*, Vol. 64, pp. 252–256. https://doi.org/10.1016/j.materresbull.2014.12.049

Bharathi, P., Krishna Mohan, M., Shalini, V., Harish, S., Navaneethan, M., Archana, J., … Hayakawa, Y. (2020). Growth and influence of Gd doping on ZnO nanostructures for enhanced optical, structural properties and gas sensing applications. *Applied Surface Science*, *499*, 143857. https://doi.org/10.1016/j.apsusc.2019.143857

Bigiani, L., Zappa, D., Comini, E., Maccato, C., Gasparotto, A., & Barreca, D. (2019). Manganese Oxide Nanoarchitectures as Chemoresistive Gas Sensors to Monitor Fruit Ripening. *Journal of Nanoscience and Nanotechnology*, *20*(5), 3025–3030. https://doi.org/10.1166/jnn.2020.17479

Bolokang, A. S., & Motaung, D. E. (2019). Reduction-oxidation of V 2 O 5 -WO 3 nanostructured by ball milling and annealing: Their improved H 2 S gas sensing performance. *Applied Surface Science*, *473*, 164–173. https://doi.org/10.1016/j.apsusc.2018.12.105

Borgschulte, A., Sambalova, O., Delmelle, R., Jenatsch, S., Hany, R., & Nüesch, F. (2017). Hydrogen reduction of molybdenum oxide at room temperature. *Scientific Reports*, *7*(September 2016), 1–9. https://doi.org/10.1038/srep40761

Cantalini, C., Valentini, L., Armentano, I., Kenny, J. M., Lozzi, L., & Santucci, S. (2004). Carbon nanotubes as new materials for gas sensing applications. *Journal of the European Ceramic Society*, *24*(6), 1405–1408. https://doi.org/10.1016/S0955-2219(03)00441-2

Chandra, L., Sahu, P. K., Dwivedi, R., & Mishra, V. N. (2017). Synthesis of Na doped ZnO nano-particles for detection of reducing gases. *2016 IEEE Uttar Pradesh Section International Conference on Electrical, Computer and Electronics Engineering, UPCON 2016*, 102–105. https://doi.org/10.1109/UPCON.2016.7894633

Chavali, M. S., & Nikolova, M. P. (2019, June 1). Metal oxide nanoparticles and their applications in nanotechnology. *SN Applied Sciences*, Vol. 1, p. 607. https://doi.org/10.1007/s42452-019-0592-3

Chithambararaj, A., & Chandra Bose, A. (2014). Role of synthesis variables on controlled nucleation and growth of hexagonal molybdenum oxide nanocrystals: Investigation on thermal and optical properties. *CrystEngComm*, *16*(27), 6175–6186. https://doi.org/10.1039/c4ce00418c

Chithambararaj, A., Rajeswari Yogamalar, N., & Bose, A. C. (2016). Hydrothermally Synthesized h-MoO3 and α-MoO3 Nanocrystals: New Findings on Crystal-Structure-Dependent Charge Transport. *Crystal Growth and Design*, *16*(4), 1984–1995. https://doi.org/10.1021/acs.cgd.5b01571

Dai, Z., Liang, T., & Lee, J. H. (2019). Gas sensors using ordered macroporous oxide nanostructures. *Nanoscale Advances*, *1*(5), 1626–1639. https://doi.org/10.1039/c8na00303c

Das, M., & Sarkar, D. (2017). One-pot synthesis of zinc oxide - polyaniline nanocomposite for fabrication of efficient room temperature ammonia gas sensor. *Ceramics International*, *43*(14), 11123–11131. https://doi.org/10.1016/j.ceramint.2017.05.159

de Castro, I. A., Datta, R. S., Ou, J. Z., Castellanos-Gomez, A., Sriram, S., Daeneke, T., & Kalantar-zadeh, K. (2017). Molybdenum Oxides – From Fundamentals to Functionality. *Advanced Materials*, *29*(40), 1–31. https://doi.org/10.1002/adma.201701619

Devendiran, S., & Sastikumar, D. (2017). Gas sensing based on detection of light radiation from a region of modified cladding (nanocrystalline ZnO) of an optical fiber. *Optics and Laser Technology*, *89*, 186–191. https://doi.org/10.1016/j.optlastec.2016.10.013

Dey, Ananya. (2018, March 1). Semiconductor metal oxide gas sensors: A review. *Materials Science and Engineering B: Solid-State Materials for Advanced Technology*, Vol. 229, pp. 206–217. https://doi.org/10.1016/j.mseb.2017.12.036

Dey, Anup, Roy, S., & Sarkar, S. K. (2018). Synthesis, Fabrication and Characterization of ZnO-Based Thin Films Prepared by Sol–Gel Process and H2 Gas Sensing Performance. *Journal of Materials Engineering and Performance*, *27*(6), 2701–2707. https://doi.org/10.1007/S11665-018-3284-Z

Dhara, A., Hodes, G., & Sarkar, S. K. (2014). Two stage chemical bath deposition of MoO3 nanorod films. *RSC Advances*, *4*(96), 53694–53700. https://doi.org/10.1039/c4ra08606f

Dongwook Kwak, Mengjing Wang, Kristie J. Koski, Liang Zhang, Henry Sokol, Radenka Maric, and Y. L. (2019). Molybdenum Trioxide (αMoO3) Nanoribbons for Ultrasensitive Ammonia (NH3) Gas Detection. Integrated Experimental and Density Functional Theory Simulation Studies.pdf. *ACS Appl. Mater. Interfaces*.

Drmosh, Q. A., Yamani, Z. H., & Hossain, M. K. (2017). Hydrogen gas sensing performance of low partial oxygen-mediated nanostructured zinc oxide thin film. *Sensors and Actuators, B: Chemical*, *248*, 868–877. https://doi.org/10.1016/j.snb.2017.01.082

Epp, J. (2016). X-Ray Diffraction (XRD) Techniques for Materials Characterization. In *Materials Characterization Using Nondestructive Evaluation (NDE) Methods* (pp. 81–124). https://doi.org/10.1016/B978-0-08-100040-3.00004-3

Espinosa, E. H., Ionescu, R., Chambon, B., Bedis, G., Sotter, E., Bittencourt, C., … Llobet, E. (2007). Hybrid metal oxide and multiwall carbon nanotube films for low temperature gas sensing. *Sensors and Actuators, B: Chemical*, *127*(1), 137–142. https://doi.org/10.1016/j.snb.2007.07.108

Espitia, P. J. P., Soares, N. de F. F., Coimbra, J. S. dos R., de Andrade, N. J., Cruz, R. S., & Medeiros, E. A. A. (2012, July). Zinc Oxide Nanoparticles: Synthesis, Antimicrobial Activity and Food Packaging Applications. *Food and Bioprocess Technology*, Vol. 5, pp. 1447–1464. https://doi.org/10.1007/s11947-012-0797-6

Fu, H., Jiang, Y., Ding, J., Zhang, J., Zhang, M., Zhu, Y., & Li, H. (2018). Zinc oxide nanoparticle incorporated graphene oxide as sensing coating for interferometric optical microfiber for ammonia gas detection. *Sensors and Actuators, B: Chemical*, *254*, 239–247. https://doi.org/10.1016/j.snb.2017.06.067

Fu, H., Wang, Q., Ding, J., Zhu, Y., Zhang, M., Yang, C., & Wang, S. (2020). Fe2O3 nanotube coating micro-fiber interferometer for ammonia detection. *Sensors and Actuators, B: Chemical*, *303*(April 2019), 127186. https://doi.org/10.1016/j.snb.2019.127186

Gaikwad, G., Patil, P., Patil, D., & Naik, J. (2017). Synthesis and evaluation of gas sensing properties of PANI based graphene oxide nanocomposites. *Materials Science and Engineering B: Solid-State Materials for Advanced Technology*, *218*, 14–22. https://doi.org/10.1016/j.mseb.2017.01.008

Girei, S. H., Majeed Alkhabet, M., Kamil, Y. M., Lim, H. N., Mahdi, M. A., & Yaacob, M. H. (2021). *Wavelength Dependent Graphene Oxide-Based Optical Microfiber Sensor for Ammonia Gas*. https://doi.org/10.3390/s21020556

Haghighi, F., Talebpour, Z., & Sanati-Nezhad, A. (2015). Through the years with on-a-chip gas chromatography: A review. *Lab on a Chip*, *15*(12), 2559–2575. https://doi.org/10.1039/c5lc00283d

Han, T., Nag, A., Chandra Mukhopadhyay, S., & Xu, Y. (2019, June 1). Carbon nanotubes and its gas-sensing applications: A review. *Sensors and Actuators, A: Physical*, Vol. 291, pp. 107–143. https://doi.org/10.1016/j.sna.2019.03.053

Hodes, G. (2007). Semiconductor and ceramic nanoparticle films deposited by chemical bath deposition. *Physical Chemistry Chemical Physics*, *9*(18), 2181–2196. https://doi.org/10.1039/b616684a

Hodgkinson, J., & Tatam, R. P. (2013). Optical gas sensing: A review. *Measurement Science and Technology*, *24*(1). https://doi.org/10.1088/0957-0233/24/1/012004

Hu, H., Deng, C., Xu, J., Zhang, K., & Sun, M. (2015). Metastable *h* -MoO_3 and stable α -MoO_3 microstructures: controllable synthesis, growth mechanism and their enhanced photocatalytic activity. *Journal of Experimental Nanoscience*, *10*(17), 1336–1346. https://doi.org/10.1080/17458080.2015.1012654

Huang, X., Lai, M., Zhao, Z., Yang, Y., Li, J., Song, H., … Liu, B. (2021). Fiber optic evanescent wave humidity sensor based on SiO 2 /TiO 2 bilayer films . *Applied Optics*, *60*(8), 2158. https://doi.org/10.1364/ao.416286

Husham, M., Hamidon, M. N., Paiman, S., Abuelsamen, A. A., Farhat, O. F., & Al-Dulaimi, A. A. (2017). Synthesis of ZnO nanorods by microwave-assisted chemical-bath deposition for highly sensitive self-powered UV detection application. *Sensors and Actuators, A: Physical*, *263*, 166–173. https://doi.org/10.1016/j.sna.2017.05.041

Ighodalo, K. O., Obi, D., Agbogu, A., Ezealigo, B. N., Nwanya, A. C., Mammah, S. L., … Ezema, F. I. (2017). The structural and optical properties of metallic doped copper (I) iodide thin films synthesized by SILAR method. *Materials Research Bulletin*, *94*, 528–536. https://doi.org/10.1016/j.materresbull.2017.06.032

Inpan, U., Leangtanom, P., Pookmanee, P., Phanichphant, S., & Kruefu, V. (2018). Synthesis of Molybdenum Trioxide: Structure Properties and Sensing Film Preparation. *Applied Mechanics and Materials*, *879*, 62–67. https://doi.org/10.4028/www.scientific.net/amm.879.62

J. Gouveia, C. A., M., J., & A.S., P. (2013). Refractometric Optical Fiber Platforms for Label Free Sensing. In *Current Developments in Optical Fiber Technology*. https://doi.org/10.5772/55376

Jakubik, W. P. (2011). Surface acoustic wave-based gas sensors. *Thin Solid Films*, *520*(3), 986–993. https://doi.org/10.1016/j.tsf.2011.04.174

Ji, H., Zeng, W., & Li, Y. (2019). Gas sensing mechanisms of metal oxide semiconductors: A focus review. *Nanoscale*, *11*(47), 22664–22684.

https://doi.org/10.1039/c9nr07699a

Jin, W., Ho, H. L., Cao, Y. C., Ju, J., & Qi, L. F. (2013a). Gas detection with micro- and nano-engineered optical fibers. *Optical Fiber Technology*, *19*(6 PART B), 741–759. https://doi.org/10.1016/j.yofte.2013.08.004

Jin, W., Ho, H. L., Cao, Y. C., Ju, J., & Qi, L. F. (2013b). Gas detection with micro- and nano-engineered optical fibers. *Optical Fiber Technology*, *19*(6 PART B), 741–759. https://doi.org/10.1016/j.yofte.2013.08.004

Kanmani, R., Zainuddin, N. A. M., Rusdi, M. F. M., Harun, S. W., Ahmed, K., Amiri, I. S., & Zakaria, R. (2019). Effects of TiO2 on the performance of silver coated on side-polished optical fiber for alcohol sensing applications. *Optical Fiber Technology*, *50*, 183–187. https://doi.org/10.1016/j.yofte.2019.03.010

Ke, Z. J., Tang, D. L., Lai, X., Dai, Z. Y., & Zhang, Q. (2018). Optical fiber evanescent-wave sensing technology of hydrogen sulfide gas concentration in oil and gas fields. *Optik*, *157*, 1094–1100. https://doi.org/10.1016/j.ijleo.2017.11.130

Khalaf, A. L., Hasan, T. S., Abdulbari, H. A., Kadhim, W. A., & Yaacob, M. H. (2021). CNT-Based Tapered Optical Fiber for Ethanol Remote Sensing Over 3-kilometer Optical fiber. *Journal of Materials Research and Technology*. https://doi.org/10.1016/j.jmrt.2021.03.103

Khan, M. I., Bhatti, K. A., Qindeel, R., Althobaiti, H. S., & Alonizan, N. (2017). Structural, electrical and optical properties of multilayer TiO2 thin films deposited by sol–gel spin coating. *Results in Physics*, *7*, 1437–1439. https://doi.org/10.1016/j.rinp.2017.03.023

Kharissova, O. V., Kharisov, B. I., González, C. M. O., Méndez, Y. P., & López, I. (2019). Greener synthesis of chemical compounds and materials. *Royal Society Open Science*, *6*(11). https://doi.org/10.1098/RSOS.191378

Khatibani, A. B. (2021). Investigation of gas sensing property of zinc oxide thin films deposited by Sol-Gel method: effects of molarity and annealing temperature. *Indian Journal of Physics*, *95*(2), 243–252. https://doi.org/10.1007/s12648-020-01689-4

Khelchand Singh, N., & Rajkumari, R. (2019). Effect of Annealing on Metal-Oxide Nanocluster. In *Concepts of Semiconductor Photocatalysis*. https://doi.org/10.5772/intechopen.82267

Korposh, S., James, S., Lee, S.-W., & Tatam, R. (2019). Tapered Optical Fibre Sensors: Current Trends and Future Perspectives. *Sensors*, *19*(10), 2294. https://doi.org/10.3390/s19102294

Kozhevnikova, N. S., Vorokh, A. S., & Uritskaya, A. A. (2015). Cadmium sulfide nanoparticles prepared by chemical bath deposition. *Russian Chemical Reviews*, *84*(3), 225–250. https://doi.org/10.1070/rcr4452

Kumar, R., Kumar, R., Kushwaha, N., & Mittal, J. (2016). Ammonia Gas Sensing Using Thin Film of MnO2 Nanofibers. *IEEE Sensors Journal*, *16*(12), 4691–4695. https://doi.org/10.1109/JSEN.2016.2550079

Kumar, S., Singh, A., Singh, R., Singh, S., Kumar, P., & Kumar, R. (2020). Facile h-MoO3 synthesis for NH3 gas sensing application at moderate operating temperature. *Sensors and Actuators, B: Chemical*, *325*(September), 128974. https://doi.org/10.1016/j.snb.2020.128974

Kwak, D., Lei, Y., & Maric, R. (2019). Ammonia gas sensors: A comprehensive review. *Talanta*, *204*, 713–730. https://doi.org/10.1016/j.talanta.2019.06.034

Lee, E., Yoon, Y. S., & Kim, D. J. (2018). Two-Dimensional Transition Metal Dichalcogenides and Metal Oxide Hybrids for Gas Sensing. *ACS Sensors*, *3*(10), 2045–2060. https://doi.org/10.1021/acssensors.8b01077

Lee, K., Lee, J. W., Dong, K. Y., & Ju, B. K. (2008). Gas sensing properties of single-wall carbon nanotubes dispersed with dimethylformamide. *Sensors and Actuators, B: Chemical*, *135*(1), 214–218. https://doi.org/10.1016/j.snb.2008.08.031

Lehmann, K. (2016). Atomic and Molecular Spectroscopy: Basic Concepts and ApplicationsAtomic and Molecular Spectroscopy: Basic Concepts and Applications , Rita Kakkar, Cambridge U. Press, 2015. $75.00 (415 pp.). ISBN 978-1-107-06388-4 Buy at Amazon . *Physics Today*, *69*(10), 57–58. https://doi.org/10.1063/pt.3.3333

Li, C., Liu, Y., Wan, W., Li, Y., Ma, Y., Zhang, J., … Zhao, H. (2020). Hydrothermal synthesis of novel porous butterfly-like hierarchical SnO2 architecture with excellent gas-sensing performance to acetaldehyde. *Sensors and Actuators, B: Chemical*, *318*. https://doi.org/10.1016/J.SNB.2020.128209

Li, X.-T., Zhu, D.-Z., Pan, L.-G., Ma, Z.-H., Lu, A.-X., Wang, D., & Wang, J.-H. (2011). [FTIR microspectroscopy and its progress in application]. *Guang Pu Xue Yu Guang Pu Fen Xi = Guang Pu*, *31*(9), 2313–2318. Retrieved from http://www.ncbi.nlm.nih.gov/pubmed/22097817

Li, Z., Ma, J., Zhang, B., Song, C., & Wang, D. (2017). Crystal phase- and morphology-controlled synthesis of MoO3 materials. *CrystEngComm*, *19*(11), 1479–1485. https://doi.org/10.1039/c6ce02437h

Liu, C., Navale, S. T., Yang, Z. B., Galluzzi, M., Patil, V. B., Cao, P. J., … Stadler, F. J. (2017). Ethanol gas sensing properties of hydrothermally grown α-MnO2 nanorods.

Journal of Alloys and Compounds, *727*, 362–369. https://doi.org/10.1016/J.JALLCOM.2017.08.150

Liu, Xiao, Cheng, S., Liu, H., Hu, S., Zhang, D., Ning, H., & Engineering, I. (2012). *A Survey on Gas Sensing Technology*. 9635–9665. https://doi.org/10.3390/s120709635

Liu, Xiaodi, Chen, C., Zhao, Y., & Jia, B. (2013). A review on the synthesis of manganese oxide nanomaterials and their applications on lithium-ion batteries. *Journal of Nanomaterials*, *2013*. https://doi.org/10.1155/2013/736375

Liu, Y., Wei, J., Tian, Y., & Yan, S. (2015). The structure-property relationship of manganese oxides: Highly efficient removal of methyl orange from aqueous solution. *Journal of Materials Chemistry A*, *3*(37), 19000–19010. https://doi.org/10.1039/c5ta05507e

Majhi, S. M., Mirzaei, A., Kim, H. W., Kim, S. S., & Kim, T. W. (2021, January 1). Recent advances in energy-saving chemiresistive gas sensors: A review. *Nano Energy*, Vol. 79, p. 105369. https://doi.org/10.1016/j.nanoen.2020.105369

Makuła, P., Pacia, M., & Macyk, W. (2018, December 6). How To Correctly Determine the Band Gap Energy of Modified Semiconductor Photocatalysts Based on UV-Vis Spectra. *Journal of Physical Chemistry Letters*, Vol. 9, pp. 6814–6817. https://doi.org/10.1021/acs.jpclett.8b02892

Malallah Rzaij, J., & Mohsen Abass, A. (2020). Review on: TiO2 Thin Film as a Metal Oxide Gas Sensor. *Journal of Chemical Reviews*, *2*(2), 114–121. https://doi.org/10.33945/sami/jcr.2020.2.4

Mane, A. T., Navale, S. T., & Patil, V. B. (2015). Room temperature NO2 gas sensing properties of DBSA doped PPy-WO3 hybrid nanocomposite sensor. *Organic Electronics*, *19*, 15–25. https://doi.org/10.1016/j.orgel.2015.01.018

Marlinda, A. R., Huang, N. M., Muhamad, M. R., An'Amt, M. N., Chang, B. Y. S., Yusoff, N., … Kumar, S. V. (2012). Highly efficient preparation of ZnO nanorods decorated reduced graphene oxide nanocomposites. *Materials Letters*, *80*, 9–12. https://doi.org/10.1016/j.matlet.2012.04.061

Matsuguchi, M., Harada, N., & Omori, S. (2014). Poly(N-isopropylacrylamide) nanoparticles for QCM-based gas sensing of HCl. *Sensors and Actuators, B: Chemical*, *190*, 446–450. https://doi.org/10.1016/j.snb.2013.08.095

Mishra, R. K., Zachariah, A. K., & Thomas, S. (2017). Energy-Dispersive X-ray Spectroscopy Techniques for Nanomaterial. In *Microscopy Methods in Nanomaterials Characterization* (pp. 383–405). https://doi.org/10.1016/b978-0-

323-46141-2.00012-2

Mittal, M., & Kumar, A. (2014). Carbon nanotube (CNT) gas sensors for emissions from fossil fuel burning. *Sensors and Actuators, B: Chemical*, Vol. 203, pp. 349–362. https://doi.org/10.1016/j.snb.2014.05.080

Miyaoka, H., Miyaoka, H., Ichikawa, T., Ichikawa, T., & Kojima, Y. (2018). Highly purified hydrogen production from ammonia for PEM fuel cell. *International Journal of Hydrogen Energy*, *43*(31), 14486–14492. https://doi.org/10.1016/j.ijhydene.2018.06.065

More, P., Dhanayat, S., Gattu, K., Mahajan, S., Upadhye, D., & Sharma, R. (2016). Annealing effect on Cu2S thin films prepared by chemical bath deposition. *AIP Conference Proceedings*, *1728*. https://doi.org/10.1063/1.4946540

Mugle, D., & Jadhav, G. (2016). Short review on chemical bath deposition of thin film and characterization. *AIP Conference Proceedings*, *1728*. https://doi.org/10.1063/1.4946648

Nadeem Riaz, K., Yousaf, N., Bilal Tahir, M., Israr, Z., & Iqbal, T. (2019). Facile hydrothermal synthesis of 3D flower-like La-MoS2 nanostructure for photocatalytic hydrogen energy production. *International Journal of Energy Research*, *43*(1), 491–499. https://doi.org/10.1002/ER.4286

Nguyen, T. T. D., Choi, H. N., Ahemad, M. J., Van Dao, D., Lee, I. H., & Yu, Y. T. (2020). Hydrothermal synthesis of In2O3 nanocubes for highly responsive and selective ethanol gas sensing. *Journal of Alloys and Compounds*, *820*. https://doi.org/10.1016/J.JALLCOM.2019.153133

Niederberger, M. (2007). Nonaqueous sol-gel routes to metal oxide nanoparticles. *Accounts of Chemical Research*, *40*(9), 793–800. https://doi.org/10.1021/AR600035E

Nikam, A. V., Prasad, B. L. V., & Kulkarni, A. A. (2018). Wet chemical synthesis of metal oxide nanoparticles: A review. *CrystEngComm*, *20*(35), 5091–5107. https://doi.org/10.1039/C8CE00487K

Nimbalkar, A. R., & Patil, M. G. (2017). Synthesis of ZnO thin film by sol-gel spin coating technique for H2S gas sensing application. *Physica B: Condensed Matter*, *527*, 7–15. https://doi.org/10.1016/J.PHYSB.2017.09.112

Nunes, D., Pimentel, A., Goncalves, A., Pereira, S., Branquinho, R., Barquinha, P., … Martins, R. (2019). Metal oxide nanostructures for sensor applications. *Semiconductor Science and Technology*, *34*(4), 1–178. https://doi.org/10.1088/1361-6641/ab011e

Oskam, G. (2006). Metal oxide nanoparticles: Synthesis, characterization and application. *Journal of Sol-Gel Science and Technology*, *37*(3), 161–164. https://doi.org/10.1007/S10971-005-6621-2

Owji, E., Mokhtari, H., Ostovari, F., Darazereshki, B., & Shakiba, N. (2021). 2D materials coated on etched optical fibers as humidity sensor. *Scientific Reports*, *11*(1). https://doi.org/10.1038/s41598-020-79563-w

Parashar, M., Shukla, V. K., & Singh, R. (2020). Metal oxides nanoparticles via sol–gel method: a review on synthesis, characterization and applications. *Journal of Materials Science: Materials in Electronics*, *31*(5), 3729–3749. https://doi.org/10.1007/S10854-020-02994-8

Park, N. H., Akamatsu, T., Itoh, T., Izu, N., & Shin, W. (2014). Calorimetric thermoelectric gas sensor for the detection of hydrogen, methane and mixed gases. *Sensors (Switzerland)*, *14*(5), 8350–8362. https://doi.org/10.3390/s140508350

Pathan, H. M., & Lokhande, C. D. (2004). Deposition of metal chalcogenide thin films by successive ionic layer adsorption and reaction (SILAR) method. *Bulletin of Materials Science*, *27*(2), 85–111. https://doi.org/10.1007/BF02708491

Ren, H., Sun, S., Cui, J., & Li, X. (2018). Synthesis, functional modifications, and diversified applications of molybdenum oxides micro-/nanocrystals: A review. *Crystal Growth and Design*, *18*(10), 6326–6369. https://doi.org/10.1021/acs.cgd.8b00894

Ren, Y., Yuan, Z., Fan, J., Huang, W., & Shuai, C. (2018). Annealing temperature-dependent morphology, structure, and optical properties of well-aligned ZnO nanowire arrays. *Applied Physics A: Materials Science and Processing*, *124*(9), 0. https://doi.org/10.1007/s00339-018-2081-8

Rickelt, L. F., Ottosen, L. D. M., & Kühl, M. (2015). Etching of multimode optical glass fibers: A new method for shaping the measuring tip and immobilization of indicator dyes in recessed fiber-optic microprobes. *Sensors and Actuators, B: Chemical*, *211*, 462–468. https://doi.org/10.1016/j.snb.2015.01.091

Sabri, N., Aljunid, S. A., Salim, M. S., Ahmad, R. B., & Kamaruddin, R. (2013). Toward optical sensors: Review and applications. *Journal of Physics: Conference Series*, *423*(1). https://doi.org/10.1088/1742-6596/423/1/012064

Sabri, N., Aljunid, S. A., Salim, M. S., & Fouad, S. (2015). Fiber optic sensors: Short review and applications. *Springer Series in Materials Science*, *204*, 299–311. https://doi.org/10.1007/978-981-287-128-2_19

Samavati, Z., Samavati, A., Ismail, A. F., Othman, M. H. D., & Rahman, M. A. (2019).

Comprehensive investigation of evanescent wave optical fiber refractive index sensor coated with ZnO nanoparticles. *Optical Fiber Technology*, *52*, 101976. https://doi.org/10.1016/j.yofte.2019.101976

Sangeetha, M., & Madhan, D. (2020). Ultra sensitive molybdenum disulfide (MoS2)/graphene based hybrid sensor for the detection of NO2 and formaldehyde gases by fiber optic clad modified method. *Optics and Laser Technology*, *127*, 106193. https://doi.org/10.1016/j.optlastec.2020.106193

Sharma, A. K., Gupta, J., & Sharma, I. (2019). Fiber optic evanescent wave absorption-based sensors: A detailed review of advancements in the last decade (2007–18). *Optik*, *183*(February), 1008–1025. https://doi.org/10.1016/j.ijleo.2019.02.104

Singer, M. A. (2007). Ammonia Toxicity. In *Comparative Physiology, Natural Animal Models and Clinical Medicine* (pp. 149–189). https://doi.org/10.1142/9781860949494_0005

Singh, K. K., Ramakrishnan, V., Ramya Prabhu, B., & John, N. S. (2017). Rapid augmentation of vertically aligned MoO3 nanorods: Via microwave irradiation. *CrystEngComm*, *19*(44), 6568–6572. https://doi.org/10.1039/c7ce01531c

Singh, N. K., Shrivastava, S., Rath, S., & Annapoorni, S. (2010). Optical and room temperature sensing properties of highly oxygen deficient flower-like ZnO nanostructures. *Applied Surface Science*, *257*(5), 1544–1549. https://doi.org/10.1016/j.apsusc.2010.08.093

Spencer, M. J. S. (2012). Gas sensing applications of 1D-nanostructured zinc oxide: Insights from density functional theory calculations. *Progress in Materials Science*, Vol. 57, pp. 437–486. https://doi.org/10.1016/j.pmatsci.2011.06.001

Srinivasan, P., Ezhilan, M., Kulandaisamy, A. J., Babu, K. J., & Rayappan, J. B. B. (2019, September 1). Room temperature chemiresistive gas sensors: challenges and strategies—a mini review. *Journal of Materials Science: Materials in Electronics*, Vol. 30, pp. 15825–15847. https://doi.org/10.1007/s10854-019-02025-1

Subramanian, M., Dhayabaran, V. V., Sastikumar, D., & Shanmugavadivel, M. (2018). Development of room temperature fiber optic gas sensor using clad modified Zn3 (VO4)2. *Journal of Alloys and Compounds*, *750*, 153–163. https://doi.org/10.1016/j.jallcom.2018.02.186

Subramanian, M., Violet Dhayabaran, V., & Shanmugavadivel, M. (2020). Fiber optic gas sensing properties of Ni2V2O7 nanorods operable at room temperature. *Materials Science and Engineering B: Solid-State Materials for Advanced Technology*, *259*, 114604. https://doi.org/10.1016/j.mseb.2020.114604

Sun, Y. F., Liu, S. B., Meng, F. L., Liu, J. Y., Jin, Z., Kong, L. T., & Liu, J. H. (2012, February 27). Metal oxide nanostructures and their gas sensing properties: A review. *Sensors*, Vol. 12, pp. 2610–2631. https://doi.org/10.3390/s120302610

Tabassum, R., & Kant, R. (2020). Recent trends in surface plasmon resonance based fiber–optic gas sensors utilizing metal oxides and carbon nanomaterials as functional entities. *Sensors and Actuators, B: Chemical*, *310*(February), 127813. https://doi.org/10.1016/j.snb.2020.127813

Tang, J., Fang, J., Liang, Y., Zhang, B., Luo, Y., Liu, X., … Chen, Z. (2018). All-fiber-optic VOC gas sensor based on side-polished fiber wavelength selectively coupled with cholesteric liquid crystal film. *Sensors and Actuators, B: Chemical*, *273*, 1816–1826. https://doi.org/10.1016/j.snb.2018.06.105

Tanguy, N. R., Thompson, M., & Yan, N. (2018). A review on advances in application of polyaniline for ammonia detection. *Sensors and Actuators, B: Chemical*, *257*, 1044–1064. https://doi.org/10.1016/j.snb.2017.11.008

Terasako, T., Obara, S., Sakaya, S., Tanaka, M., Fukuoka, R., Yagi, M., … Yamamoto, T. (2019). Morphology-controlled growth of ZnO nanorods by chemical bath deposition and seed layer dependence on their structural and optical properties. *Thin Solid Films*, *669*(September 2018), 141–150. https://doi.org/10.1016/j.tsf.2018.10.039

Thangaraj, S., Paramasivan, C., Balusamy, R., Arumainathan, S., & Thanigainathan, P. (2020). Evanescent wave optical fibre ammonia sensor with methylamine hydroiodide. *IET Optoelectronics*, *14*(5), 292–295. https://doi.org/10.1049/iet-opt.2019.0144

Tian, W., Liu, X., & Yu, W. (2018). Research Progress of Gas Sensor Based on Graphene and Its Derivatives: A Review. *Applied Sciences*, *8*(7), 1118. https://doi.org/10.3390/app8071118

Tseng, S.-M., & Chen, C.-L. (1992). Side-polished fibers. *Applied Optics*, *31*(18), 3438. https://doi.org/10.1364/ao.31.003438

Tu, Y., Kyle, C., Luo, H., Zhang, D. W., Das, A., Briscoe, J., … Krause, S. (2020). Ammonia Gas Sensor Response of a Vertical Zinc Oxide Nanorod-Gold Junction Diode at Room Temperature. *ACS Sensors*, *5*(11), 3568–3575. https://doi.org/10.1021/acssensors.0c01769

Wang, C., Yin, L., Zhang, L., Xiang, D., & Gao, R. (2010a). Metal oxide gas sensors: Sensitivity and influencing factors. *Sensors*, *10*(3), 2088–2106. https://doi.org/10.3390/s100302088

Wang, C., Yin, L., Zhang, L., Xiang, D., & Gao, R. (2010b, March). Metal oxide gas sensors: Sensitivity and influencing factors. *Sensors*, Vol. 10, pp. 2088–2106. https://doi.org/10.3390/s100302088

Wang, H., & Na, C. (2015). Chemical Bath Deposition of Aluminum Oxide Buffer on Curved Surfaces for Growing Aligned Carbon Nanotube Arrays. *Langmuir*, *31*(26), 7401–7409. https://doi.org/10.1021/acs.langmuir.5b01002

Wang, L. C., Tang, K. T., Teng, I. J., Kuo, C. T., Ho, C. L., Kuo, H. W., … Chang, C. P. (2011). A single-walled carbon nanotube network gas sensing device. *Sensors*, *11*(8), 7763–7772. https://doi.org/10.3390/s110807763

Wang, Q., Fu, H., Ding, J., Yang, C., & Wang, S. (2020). Sensitivity enhanced microfiber interferometer ammonia gas sensor by using WO3 nanorods coatings. *Optics and Laser Technology*, *125*(October 2019), 106036. https://doi.org/10.1016/j.optlastec.2019.106036

Wong, Y. C., Ang, B. C., Haseeb, A. S. M. A., Baharuddin, A. A., & Wong, Y. H. (2020). Review—Conducting Polymers as Chemiresistive Gas Sensing Materials: A Review. *Journal of The Electrochemical Society*, *167*(3), 037503. https://doi.org/10.1149/2.0032003jes

Xiang, D., Han, C., Zhang, J., & Chen, W. (2015). Gap States Assisted MoO3 Nanobelt Photodetector with Wide Spectrum Response. *Scientific Reports*, *4*. https://doi.org/10.1038/srep04891

Xue, Z. Y., Xu, P., Gu, L. Y., & Ren, Y. (2017). Characterization of MoO3 solution prepared using bath deposition. *Key Engineering Materials*, *727*, 588–591. https://doi.org/10.4028/www.scientific.net/KEM.727.588

Yadav, B. C., Chauhan, · K S, Singh, · S, Sonker, · R K, Sikarwar, · S, & Kumar, · R. (2016). Growth and characterization of sol-gel processed rectangular shaped nanostructured ferric oxide thin film followed by humidity and gas sensing. *Journal of Materials Science: Materials in Electronics*, *28*, 5270–5280. https://doi.org/10.1007/s10854-016-6184-8

Yahya, N. A. M., Hamid, M. R. Y., Ong, B. H., Rahman, N. A., Mahdi, M. A., & Yaacob, M. H. (2020). H2 Gas Sensor Based on Pd/ZnO Nanostructures Deposited on Tapered Optical Fiber. *IEEE Sensors Journal*, *20*(6), 2982–2990. https://doi.org/10.1109/JSEN.2019.2957838

Yang, L. L., Zhao, Q. X., Willander, M., Yang, J. H., & Ivanov, I. (2009). Annealing effects on optical properties of low temperature grown ZnO nanorod arrays. *Journal of Applied Physics*, *105*(5). https://doi.org/10.1063/1.3073993

Yang, S., Lei, G., Lan, Z., Xie, W., Yang, B., Xu, H., … Gu, H. (2019a). Enhancement of the room-temperature hydrogen sensing performance of MoO 3 nanoribbons annealed in a reducing gas. *International Journal of Hydrogen Energy*, *44*(14), 7725–7733. https://doi.org/10.1016/j.ijhydene.2019.01.205

Yang, S., Lei, G., Lan, Z., Xie, W., Yang, B., Xu, H., … Gu, H. (2019b). Enhancement of the room-temperature hydrogen sensing performance of MoO3 nanoribbons annealed in a reducing gas. *International Journal of Hydrogen Energy*, *44*(14), 7725–7733. https://doi.org/10.1016/j.ijhydene.2019.01.205

Yang, S., Wang, Z., Hu, Y., Luo, X., Lei, J., Zhou, D., … Gu, H. (2015). Highly responsive room-temperature hydrogen sensing of α-MoO3 nanoribbon membranes. *ACS Applied Materials and Interfaces*, Vol. 7, pp. 9247–9253. https://doi.org/10.1021/acsami.5b01858

Yantchev, V. M., Strashilov, V. L., Rapp, M., Stahl, U., & Avramov, I. D. (2002). Theoretical and experimental mass-sensitivity analysis of polymer-coated SAW and STW resonators for gas sensing applications. *IEEE Sensors Journal*, *2*(4), 307–312. https://doi.org/10.1109/JSEN.2002.804039

Yao, Q., Ren, G., Xu, K., Zhu, L., Khan, H., Mohiuddin, M., … Ou, J. Z. (2019). 2D Plasmonic Tungsten Oxide Enabled Ultrasensitive Fiber Optics Gas Sensor. *Advanced Optical Materials*, *7*(24), 1–7. https://doi.org/10.1002/adom.201901383

Zhang, C., Liu, G., Geng, X., Wu, K., & Debliquy, M. (2020, July 1). Metal oxide semiconductors with highly concentrated oxygen vacancies for gas sensing materials: A review. *Sensors and Actuators, A: Physical*, Vol. 309, p. 112026. https://doi.org/10.1016/j.sna.2020.112026

Zhang, X., Wu, X., Amrehn, S., & Wagner, T. (2019). Refractive index modulation in metal oxides arising from chemically induced free carriers and its application in gas sensing. *Journal of Materials Chemistry C*, *7*(22), 6752–6758. https://doi.org/10.1039/c9tc01612k

Zhang, Y. nan, Peng, H., Qian, X., Zhang, Y., An, G., & Zhao, Y. (2017). Recent advancements in optical fiber hydrogen sensors. *Sensors and Actuators, B: Chemical*, *244*, 393–416. https://doi.org/10.1016/j.snb.2017.01.004

Zhu, C., & Panzer, M. J. (2014). Seed layer-assisted chemical bath deposition of CuO films on ITO-coated glass substrates with tunable crystallinity and morphology. *Chemistry of Materials*, *26*(9), 2960–2966. https://doi.org/10.1021/cm500762w

Zhu, L., & Zeng, W. (2017, November 1). Room-temperature gas sensing of ZnO-based gas sensor: A review. *Sensors and Actuators, A: Physical*, Vol. 267, pp. 242–261. https://doi.org/10.1016/j.sna.2017.10.021